

EFFECTS OF MARANGONI FLOWS ON PARTICLE TRANSPORT AND
DEPOSITION DURING DROP EVAPORATION

A Dissertation

Submitted to the Faculty

of

Purdue University

by

Lihui Wang

In Partial Fulfillment of the

Requirements for the Degree

of

Doctor of Philosophy

August 2019

Purdue University

West Lafayette, Indiana

THE PURDUE UNIVERSITY GRADUATE SCHOOL
STATEMENT OF DISSERTATION APPROVAL

Dr. Michael T. Harris, Chair

Davidson School of Chemical Engineering

Dr. Osman A. Basaran

Davidson School of Chemical Engineering

Dr. David S. Corti

Davidson School of Chemical Engineering

Dr. Carl Wassgren

School of Mechanical Engineering

Approved by:

Dr. David S. Corti

Thesis From Head

ACKNOWLEDGMENTS

I would like to first thank my advisor, Prof. Michael Harris, for his guidance along my entire PhD journey. He put my development as a high priority, provided many valuable opportunities and encouraged me to pursue research excellence. He is very open-minded about research and give me the freedom to explore interesting topics. He is also understanding and patiently supports me when I have difficulties, which allowed me to think deeply about my problems.

I would also like to thank Prof. Osman Basaran, Prof. David Corti and Prof. Carl Wassgren for being my committee members and providing valuable critique and direction from their perspectives. Prof. Basaran has also mentored me much in terms of learning fluid mechanics, and the rigorous, critical thinking he has inspired in me. I appreciate very much that he allowed me to attend his group meetings, because I not only learned from each group member but also received feedbacks on my projects in his perspectives.

My parents, Zhiming Wang and Guang Zhang are the ones who made my four-year of exploration and growth possible from the start. I would like to thank their constant unconditional love and support, and the role model they have set up regarding life attitudes. I am grateful that I have a father who encourages me to explore the unknown and a mother who helps me stay positive all the time.

My boyfriend, Zhao Wang, is the one who has been supporting me in every aspect of my life. He discusses with me and gives suggestions on problems ranging from academic problems, life decisions to everyday trivial details. I appreciate his company through my PhD journey as well as the years before, which let me feel someone is always there for me to confront any obstacles together.

My office mates and group mates are the people who fight together with me in the field. I would like to thank them for their help. Dr. Chris Anthony spent much time and

effort teaching me from scratch to use the tool for my research. He has also developed the multifrontal solver code and tailored it for my project, which allowed me to get results from simulations much faster. Dr. Prithish Kamat was the one who first inspired me to work on fluid mechanics with his poster presentation, and later his creative and critical thinking also inspired me to consider problems comprehensively. Dr. Sumeet Thete helped me understanding fundamental aspects of my research when I first started the project. He was also very helpful when I started job hunting, although we only overlapped less than a year. I thank Dr. Vishrut Garg because he helped me solve detailed problems and provided feedbacks on my ideas. I am grateful to have such an intelligent and diligent person sitting next to me for three years. Brayden Wagoner is the student who has accompanied me almost through my entire research time and many courses. His enthusiasm about research inspires me all the time and it has been a pleasure to discuss problems with him from time to time. His expertise in experiments also broadened my knowledge in the field. I also had a pleasant time working with Hansol Wee for he is rigorous and brings up useful opinions even though working in the area for less time. Prof. Shohreh Hemmati worked in the group for a year and helped me on lab management. It was nice to have a group mate like her. Dr. Nicole Vadivel discussed questions with me when I first started the project, which I am also thankful for.

My friends during the four years are very important to me. Dr. Jianfeng Liu is not only a friend of mine, but also a mentor. I appreciate his help on teaching me driving cars, setting a model on actively looking for opportunities, and many other aspects. I am grateful to have met Dr. Yang Xiao, Dr. Zhenwei Wu, Yi Ding and to have their company. I would like to thank my roommates, Dr. Tingting Wang and Huang Zhang, to have accompanied and helped me at home. I also thank Yiru Li, Claire Liu, Laryssa Ceasers, Jaeyub Cheung to accompany me through the start of my PhD journey. I am grateful to have met Dr. Donghan Ma, Dr. Heng Lv, Dr. Fan Xu and Yilun Li, who share the same interest with me in playing badminton.

Last but not least, I am grateful to have Bev Johnson to help with almost everything at school. She has always been efficient, patient and kind.

TABLE OF CONTENTS

	Page
LIST OF TABLES	vii
LIST OF FIGURES	viii
SYMBOLS	xv
ABBREVIATIONS	xviii
ABSTRACT	xix
1 INTRODUCTION	1
1.1 Drop Evaporation of Pure Fluid	1
1.1.1 Classification of Drop Evaporation	1
1.1.2 Evaporation Rate and Flux	3
1.1.3 Flow Types in an Evaporating Drop	5
1.1.4 Marangoni Flow	7
1.2 Particle Behaviors in an Evaporating Drop	10
1.2.1 Particle Adsorption, Coagulation, Convection and Diffusion	10
1.2.2 Adsorption to the Substrate	12
1.2.3 Particle Accumulation on the Drop-air Interface	13
1.3 Objective of the Dissertation	16
2 METHODS	18
2.1 Governing Equations	21
2.2 Boundary Conditions	23
2.3 Numerical Method	27
2.3.1 Mesh Adjustment	33
2.3.2 Two-Part FEM Formulations of Boundary Conditions	35
3 RESULTS	40
3.1 Drop Surface Temperature	40
3.1.1 Effect of Heat Convection	40
3.1.2 Extremum Points	46
3.1.3 The Effect of Substrate Dimensions On Temperature	48
3.2 Multi-Circulation Flow Profiles	54
3.2.1 Flow Profiles and Stagnation Points	54
3.2.2 Capillary-Induced Stagnation Point	60
3.2.3 Offset of Marangoni-Induced Stagnation Points	62

	Page
3.2.4 The Effect of Circulations on Particle Distribution	66
3.3 Particle Distribution Affected by Marangoni Flows	67
3.3.1 The Influence of Marangoni Flows with a Negative Ma	67
3.3.2 The Results with a Positive Ma	70
3.3.3 Results of Thermal Marangoni Flows	79
3.3.4 Regional Segregation in Thermal Marangoni Circulations	83
3.4 Particle Adsorption	95
3.4.1 The Influence of Viscosity Change Due to Particle Concentration Increase	95
3.4.2 Substrate Adsorption	97
4 SUMMARY AND FUTURE WORK	107
4.1 Summary	107
4.2 Future Studies	108
REFERENCES	110
A CONTACT ANGLE CHANGE	118
B NON-DIMENSIONALIZATION OF GOVERNING EQUATIONS AND BCS	119
B.1 Governing Equations	119
B.2 Boundary Conditions	120

LIST OF TABLES

Table	Page
2.1 Simulation Parameters	19
2.2 Characteristic Variables	20
2.3 Dimensionless Groups	21
2.4 Convergence Information	32

LIST OF FIGURES

Figure	Page
1.1 This figure shows the two pure modes of droplet evaporation. The right is the fixed-contact angle mode: a droplet with a constant contact angle. The left is the pinned-contact line mode: a drop with a constant contact area, or a pinned contact line. The solid line shows the drop before evaporation, and the dashed line shows the drop after part of liquid evaporates.	2
1.2 Flow profiles of (a) capillary flow only, and (b) circulation forming by capillary flow and Marangoni flow	6
1.3 Ellipsoid particles presented obvious interparticle capillary attraction and a particle in the bulk phase adsorb to surface packed structures on their way to the contact line [90].	14
2.1 Cylindrical coordinates (r, z) were used, and the azimuth coordinate was neglected. The base of the drop is located at the height of $z = 0$, and has a radius of R	18
2.2 Boundary conditions	26
2.3 A coarse example of the mesh distribution. The red dashed line shows the algebraic mesh restriction.	28
2.4 The actual mesh used for computation.	28
2.5 The comparison of the results with 2 mesh distribution: (1)the mesh actually used for results; (2)a even denser mesh to validate precision. The overlap proves the mesh in Figure 2.4 to be sufficient.	29
2.6 The time intervals of each time step dt changing in simulations according to the change rate of the solved variables. CA $theta$ decreases from the right to the left during simulations. Small dt implies a rapid change of flow, temperature or concentration profiles at that θ	31
2.7 The distribution of $f(\xi)$ and $g(\eta)$	34
2.8 The mesh near CL	36
2.9 Two-part surface integral formulation: Element I in the drop domain gives the terms contain T in the surface integral, while Element II in the substrate domain gives the terms of T_s	36

Figure	Page
3.1 Surface temperature under various θ changing as evaporation. The influence of heat convection was shown by the comparison of the dashed lines (no convection) and the solid lines (convection included). Heat convection is negligible when $\theta < 15^\circ$	41
3.2 Surface temperature when no Marangoni flow was included. The overlap of the results with or without heat convection illustrates that heat convection was negligible.	42
3.3 The magnitude of the dimensionless axial velocity $v = \tilde{v}/v_c$ from numerical results when Marangoni flow was included. v_c is the scale of the capillary flow. $ v $ can be as large as 10^3 , meaning the Marangoni flow was much stronger than the capillary flow. The magnitude decreased with evaporation as the contact angle decreased.	43
3.4 The balance of the Marangoni stress and the viscous stress.	44
3.5 Temperature profile in the drop when $\theta = 38^\circ$. Temperature changes faster in the axial direction than in the radial direction.	45
3.6 The dependence of the aspect ratio on θ	47
3.7 The direction of Marangoni stress	47
3.8 Locations of extremum points ($d\sigma/ds = 0$). As drop evaporates, θ decreases from the right to the left on the abscissa axis. Given a pair of (θ, r) , $d\sigma/ds > 0$ if it is on the right of the extremum line, and $d\sigma/ds < 0$ if on the left.	48
3.9 The surface temperature of the air-drop interface ($0 \leq r \leq 1$) and the air-substrate interface ($r \geq 1$)	49
3.10 The isotherms when $\theta = 14^\circ$ for the whole domain and near the contact line.	50
3.11 Locations of extremum points ($d\sigma/ds = 0$) when the substrate radius was set to be R.	50
3.12 The extremum point locations of the results with substrate length of $l_s = 1.3$ and $l_s = 2.0$. The complete overlap indicates that using $l_s = 1.3$ was enough and further extending the length of the substrate in simulations will be no use.	51
3.13 The locations r and changes with θ of extremum points for results with various substrate thickness d	52
3.14 The comparison of the results with different substrate temperature at the bottom. The results are the surface temperature gradient at various θ . The temperature was set to be room temperature ($\tilde{T} = 25^\circ C$) and $\tilde{T} = 40^\circ C$, which means a slight heating at the bottom. The gradient of the temperature was almost the same with the two cases.	53

Figure	Page
3.15 A perfect circulation flow was developed when $\theta = 40^\circ$	54
3.16 Flow profiles of multi-circulation when $\theta = 14^\circ$. Zooming in to CL showed a stagnation point near CL.	54
3.17 Flow profiles of multi-circulation when $\theta = 10^\circ$. Zooming in to CL showed two stagnation points near CL at different locations.	55
3.18 The radial locations r of the stagnation points, where the surface flow is 0, as θ decreases with evaporation. The surface flow is inward on the right of the line and outward on the left.	57
3.19 Comparison between locations of stagnation points and $\tau_{Ma} = 0$ points. The locations of stagnation points are not exactly where $\tau_{Ma} = 0$ due to capillary flow. The stagnation points close to $r = 1$ emerge much earlier than extremum points during evaporation.	58
3.20 Flow profiles and Marangoni stresses near the two kinds of stagnation points.	59
3.21 Flow profile near the contact line with $\theta = 10^\circ$ with a constant evaporation flux imposed. No capillary-induced stagnation point emerged.	60
3.22 The comparison of the locations between the stagnation points and the extremum points with the uniform flux condition. The locations overlapped for all of the points and no extra stagnation points emerged.	61
3.23 Lubrication theory: When τ_{Ma} is negative, v_s can be positive or negative based on the value of $\bar{u}_r(r, \theta)$	62
3.24 The parameters of liquid were changed to those of octane. The comparison between locations of stagnation points and extremum points showed an offset even at small r , which did not happen when the parameters were for water.	63
3.25 Offset of the Marangoni-induced stagnation point from the extremum point: τ_{Ma} and surface flow in opposite directions between the two points. A Marangoni-induced stagnation point located at where $\tau_{Ma} = -\tau_{offset}$, away from the extremum point where $\tau_{Ma} = 0$	64
3.26 A diagram of offset of a Marangoni-induced stagnation point. The Marangoni-induced stagnation point is located at where $\tau_{Ma} = -\tau_{offset}$, away from the extremum point where $\tau_{Ma} = 0$	65
3.27 The particle concentrations c_p at the drop surface with Marangoni flow or with pure capillary flow.	66
3.28 Particle concentration when $\theta = 20^\circ$ with only the capillary flow. There were mainly two regions where the particle concentration was higher than other regions: near the contact line (CL) and at the drop surface.	67

Figure	Page
3.29 A comparison of particle distribution at $\theta = 20^\circ$ between the case with clockwise Marangoni flow and the case with no Marangoni flow. The left is the case with no Marangoni flow. A Marangoni number of $Ma = 10^5$ was used for the case with Marangoni flow. Capillary flow transported most particles near the CL, while Marangoni circulation kept particles suspended in the drop with a higher concentration.	68
3.30 The mass fractions of particles left in the middle of the drop depend on the strength of Marangoni stresses. x_{inner} is the mass fraction of particles that located at a radial position less than 0.8 ($r < 0.8$) when CA decreased to $\theta = 20^\circ$. It is larger for larger Marangoni stresses, viz. larger Marangoni number Ma .	69
3.31 The profile on the right is with a reverse Marangoni stress of $Ma = 10^3$. The flow profile divided the drop into two regions. One is the clockwise circulation, and the other is the edgeward flow near the CL. The edgeward flow transported the accumulated particles at the drop surface to CL, while the circulation made the particle concentration within the circulation region uniform. Therefore, compared to the capillary flow case on the left, the drop surface presented lower concentration, and the high concentration only showed near CL.	70
3.32 On the left of the transition point, the flow is toward the center of the drop along the bottom; on the right, the flow is toward CL. The mathematical expression of the left side is $\partial u / \partial z < 0$ and vice versa, since the application of no-slip BC gives $u = 0$ at $z = 0$. The transition point has a radial location r_T where $\partial u / \partial z = 0$	71
3.33 The radial location r of the transition point changes as the CA, θ , decreased during drop evaporation (θ value changes from the right to the left of the abscissa). A fixed $Ma = 10^3$ led to a distinct movement of the transition point (r_T changed by 0.2). Setting $\theta \cdot Ma = 2 \times 10^4$ restricted r_T between $r = 0.85$ and $r = 0.9$. The moving distance of the transition point was much smaller than the case with a constant Ma	72
3.34 The transition point stayed at different ranges of radial positions r when $\theta \cdot Ma$ has different values.	74
3.35 The locations of the transition point r_T under various Ma at a contact angle of 20° .	75
3.36 The change of r_T with CA θ when different Ma was imposed. The transition point moved inward as evaporation proceeds for the case of a fixed Ma	76
3.37 Profiles at $\theta = 20^\circ$ with $Ma = 10^5$ (Figure (a)), where clockwise circulation was formed, and $Ma = -10^5$ (Figure (b)), where counterclockwise circulation was formed. The scale bars for c_p are the same. The clockwise circulation and counterclockwise circulation lead to similar particle distribution.	77

Figure	Page
3.38 The mass fractions of particles left in the middle of the drop versus Ma when Marangoni stresses are in the direction from the top to CL. x_{inner} is the mass fraction of particles that located at a radial position less than 0.8 ($r < 0.8$) when CA decreased to $\theta = 20^\circ$	78
3.39 Temperature, flow and concentration profiles at the CA of $\theta = 20^\circ$. The temperature profile is the left side and shows both the drop domain and the substrate domain. A counter clockwise circulation was caused by Marangoni flow toward the top of the drop. The Marangoni flow results from the decrease of temperature from CL to the top of the drop.	80
3.40 The temperature T change on the surface of the drop became non-monotonous. A flow profile of two circulations presented at $\theta = 14^\circ$. The circulation close to CL was counterclockwise, and the other was clockwise. Between the two circulations at the drop surface, a Marangoni-induced stagnation point existed at the minimum of temperature. The particle concentrations c_p near the stagnation point were large.	81
3.41 At $\theta = 10^\circ$, the temperature minimum located close to CL. There were still two circulations. The counterclockwise circulation near CL took up a small corner of the drop. The particle concentrations c_p inside the CL circulation were the largest.	81
3.42 The values of the concentrations c_p at different radial locations r of the drop surface at various CAs θ	82
3.43 The surface temperature T and correspondent Marangoni number Ma changing with radial positions r . The Marangoni stress (Ma) magnitude was determined by the temperature gradient on the surface. Ma in the CL region is quite large due to the sharp temperature change. The results are at $\theta = 10^\circ$ with a condition of $d = 0.5$	84
3.44 The concentration at the surface at different radial locations at $\theta = 10^\circ$. The green line shows the CL accumulation brought by the capillary flow, featured with a smooth increase of the concentration approaching CL. The red and the blue lines are results with thermal Marangoni flow. They manifests the concentration difference due to the regional segregation. The larger substrate thickness d led to a wider CL concentration plateau.	86
3.45 The locations r of transition points changing with the contact angle θ during evaporation. The thickness of the substrate d determined how early a transition point emerged and how far the transition point was away from CL. If d is larger than 1.5, increasing the thickness does not make a difference anymore.	87

Figure	Page
3.46 The high concentration region was restricted between the turning point and CL, and was pushed shrinking by the transition point. The contours are for the normalized particle concentration $c_{pN} = c_p/c_{pA}$, where c_{pA} is the averaged concentration for the current CA.	89
3.47 The locations r of transition points changing with the contact angle θ during evaporation. The thermal conductivity of the substrate k_s determined how early a transition point emerged and how far the transition point was away from CL.	90
3.48 The temperature profiles for $k_s = 0.6$. The surface temperature was plotted separately. The results are with $d = 0.5$	91
3.49 The temperature profiles for $k_s = 1.2$. The surface temperature was plotted separately. The results are with $d = 0.5$	92
3.50 The temperature profiles for $d = 0.5, k_s = 0.8$	93
3.51 The temperature profiles for $d = 1.0, k_s = 0.8$	94
3.52 The locations of stagnation points are compared with simulations incorporating the influence of viscosity change and simulations without viscosity change. The results are with $d = 0.15$	95
3.53 The locations of transition points are compared with simulations incorporating the influence of viscosity change and simulations without viscosity change. The results are with $d = 0.15$	96
3.54 As a drop evaporates, the CA decreases from the right to the left on the abscissa. The red line shows the amount of particles in the bulk of the drop phase. The green line shows the amount of particles deposited on the substrate due to the adsorption. The blue line is the summation of the particle amount in the bulk phase and on the substrate. The results are for $Da = 100$. The Marangoni flow was caused by temperature change. The substrate thickness was $d = 0.5$	98
3.55 The meaning of the lines are the same as Figure 3.54. The results are for $Da = 100$ and pure capillary flows.	99
3.56 The surface concentration of the particles deposited on the substrate Γ_{sub} versus θ as CA decreased. The results are for $Da = 100$. The Marangoni flow was caused by temperature change. The substrate thickness was $d = 0.5$	100
3.57 The flow and concentration profile at $\theta = 17^\circ$ with $Da = 100$. The Marangoni flow was induced by temperature change with $d = 0.5$	101
3.58 The flow and concentration profile at $\theta = 17^\circ$ with $Da = 100$. The flow was pure capillary flow with no Marangoni stress effect.	101

Figure	Page
3.59 The surface concentration of the particles deposited on the substrate Γ_{sub} versus θ as CA decreased. The results are for $Da = 100$. No Marangoni flow was incorporated.	102
3.60 $\theta_{0.8}$ is the CA at the moment when 80% of the total particles were deposited on the substrate. The larger $\theta_{0.8}$ is, the earlier most particles deposit on the substrate, indicating the faster a deposition rate. The value of $\theta_{0.8}$ changed with Ma . The Marangoni stress is in the same direction as the tangential unit vector.	103
3.61 The same plot as Figure 3.60 but the direction of Marangoni stress, which was in the opposite direction as the tangential unit vector leading to counterclockwise circulation. Ma was negative, but the absolute value was used in the plot.	104
3.62 Three types of surface concentration Γ (blue for suspended particles, green for deposited particles and red for total particles) versus the radial locations r at $\theta = 12^\circ$. $Da = 100$. The plots are for different values of Ma imposed: the negative ones mean the Marangoni stress is in the opposite direction from the tangential unit vector \mathbf{t}	106
A.1 The CA, θ , changing with the dimensionless time t . The characteristic time is 1.5×10^3 s.	118

SYMBOLS

r	radial coordinate
z	axial position
t	time
m	mass
R	radius of the base of the drop
l_s	substrate length (radius)
d	substrate thickness
θ	contact angle
ρ	fluid density
μ	fluid viscosity
σ	drop-air surface tension
β	coefficient of surface tension changes with temperature
g	gravitational acceleration
\mathbf{v}	velocity
u	radial velocity
v	axial velocity
v_s	velocity at the surface
p	pressure
T	temperature
c_p	particle concentration
c_{p0}	initial particle concentration
c_{pm}	the particle concentration when maximum packing is reached
c_{pN}	normalized particle concentration
\mathbf{T}	stress tensor

\mathbf{I}	identity matrix
T	drop temperature
T_s	substrate temperature
k_s	thermal conductivity of the substrate
k_l	thermal conductivity of the drop
μ	viscosity
α	thermal diffusivity
r_p	particle radius
D_p	particle diffusion coefficient
D	vapor diffusion coefficient
c	vapor concentration
J	evaporation mass flux
c	vapor concentration
h	drop surface height
H	the height of the drop at the center
$2\mathcal{H}$	twice the mean curvature
Jac	determinant of the Jacobian in each element for the finite element method
\mathbf{n}	normal unit vector
\mathbf{t}	tangential unit vector
s	arc length in the direction of the tangential unit vector
Γ	particle surface concentration
α_V	volumetric thermal expansion coefficient
τ_{Ma}	Marangoni stress
τ_c	characteristic stress
k	reaction coefficient of the particle adsorption to the substrate surface
∇_s	surface gradient
Δ	variable difference
k_B	Boltzman constant

Hum	relative humidity in air
H_v	latent heat of vaporization
k_a	air thermal conductivity
Re	Reynolds number
Ca	capillary number
Pe	Peclet number for thermal transport
Pe_{Ma}	Peclet number for thermal transport based on Marangoni flow
Pe_p	Peclet number for particle transport
REH	Relative latent heat of evaporation
k_R	relative heat conductivity
F_0	Fourier number
Ma	Marangoni number
Da	Damkoler number for particle adsorption to the substrate
B	gravitational Bond number

ABBREVIATIONS

CL	contact line
CA	contact angle
CCA	constant contact angle evaporation mode
CCR	constant contact radius evaporation mode
CAH	contact angle hysteresis
FEM	finite element method
PDE	partial differential equation
ODE	ordinary differential equation
BC	boundary condition

ABSTRACT

Wang, Lihui PhD, Purdue University, August 2019. Effects of Marangoni Flows on Particle Transport and Deposition during Drop Evaporation. Major Professor: Michael T. Harris.

The evaporation of a liquid drop containing particles resting on a substrate have diverse industrial applications including inkjet printing, spray coating, fabrication of functional nanomaterials, disease diagnosis, among others. In addition to these wide ranging practical applications, the sessile drop evaporation can be observed in everyday life with dew drops, coffee spills, and the dry patterns of other beverages.

The self-assembly of particles during drop evaporation is a process that is affected by various factors, such as contact line (CL) behaviors, microfluidic flows, short-range interactions of particle-interface and particle-particle. Each of these factors are complicated enough to study, let alone the total effects on the process. The primary goal of this work is to investigate the influence of microfluidic flows and the particle-interface interaction, viz. the evaporation process was subject to a pinned CL and the particle-particle interaction was neglected under dilute particle concentration. To accomplish this goal, the Galerkin/Finite Element Method (G/FEM) is used to solve for the flow, the temperature and the particle concentration profiles.

The complexity of the problems comes from various surface phenomena, one of which is the surface tension. The surface tension brings capillary force in the normal direction and capillary flow toward the CL, which results in the well-known coffee-ring effect. Moreover, the surface tension changes with temperature, surfactant concentration, etc. resulting in Marangoni stresses in the tangential direction. The Marangoni stress on the surface leads to circulations of flow inside the drop and the circulation can be either clockwise or counterclockwise depending on the direction of the stress.

When the Marangoni stress is merely caused by temperature change, the circulation direction changes not only in time but also in space. At late stage of evaporation, i.e. with a small contact angle (CA), multi-circulation flow profiles emerge. This flow profiles are featured with stagnation points and transition points. The stagnation points can be further categorized into capillary-induced stagnation points and Marangoni-induced stagnation points. By introducing the concept of capillary-induced stagnation points, the simulations reached agreement with experiments in terms of the radial location of the observed stagnation points.

The multi-circulation flow profiles implied regional segregation inside the drop. When a large circulation is observed in most part of the drop and a small circulation exists near the CL, particle concentrations are relatively uniform in each individual region but differs significantly across the two regions. Transition points are used to characterize the location of the regional segregation, which can be adjusted by Marangoni stress.

Marangoni circulations in different directions revealed distinct influences on particle distribution and deposition. First, while both directions facilitate even distribution of particles, a clockwise circulation strengthens CL accumulation for a small Marangoni stress. Second, a counterclockwise circulation with a small Marangoni stress impedes the deposition rate of particles, while a clockwise circulation facilitates the deposition no matter how small the Marangoni stress is. This results is under a condition of a strong adsorption between particles and substrates.

The analysis and understanding of the above results are crucial to elucidating and controlling the final deposition patterns of particles. Thus, the focus of this research is to understand the combined effect of Marangoni stress and capillary flow on particle deposition during sessile drop evaporation.

1. INTRODUCTION

Drop drying is a common phenomenon in nature. It is mostly well known for the “coffee ring” pattern that is left by a coffee drop after the drop dries on a table. The process of the pattern formation was first explained and scaled by Deegan [1]. The system of evaporating drops containing non-volatile solutes receives great attention and has been widely applied in fields like photonic device production [2–5], disease diagnosis [6–8], deposition of DNA sequencing microarrays [9, 10], nanochromatography [11, 12] and other evaporative self-assembly techniques [13, 14]. Various modifications to this system have been used, such as drop drying on hydrophobic surfaces [15], surfactant addition [16], vibration or electric field applications [17, 18], to control the deposition patterns. But a theoretical understanding of the process of particle deposition in drop evaporation requires further study.

1.1 Drop Evaporation of Pure Fluid

1.1.1 Classification of Drop Evaporation

First, evaporating drops can be classified, based on their positions, into sessile drops, pendant drops, and inclined drops. This classification is important because gravity shows its effect for different positions. One effect of gravity is the shape of drops. This effect is only important when a drop is large enough. When the drop base radius R is much smaller than the capillary length $l_{cap} = \sqrt{\sigma/\rho g}$ (where σ is surface tension, ρ is fluid density, g is gravitational constant), the drop shape is determined by capillary force as a spherical cap. In the adverse case, the drop sags under gravity. Another effect of gravity is the buoyancy-driven flow, which is important when the gravitational Bond number is large. The last effect of gravity is its influence on the particles inside colloidal drops, especially when particles inside the drops are over 1 nm [19].

Another classification of drop evaporation is according to the contact line and contact angle θ behaviors as evaporation processes. The contact line location represents the drop base radius R . Two most typical modes are a pinned-contact-line mode and a fixed-contact-angle mode [20] (Figure 1.1). In the former case, the contact line of the drop is fixed at a certain location, and the contact angle of the drop decreases as the drop evaporates. In the latter case of a fixed-contact-angle mode, the contact line moves inward and the contact angle remains the same. The whole evaporating process does not happen solely in one of the two modes. These modes are used to describe a certain period of the evaporation. A mixed type was also reported to describe that the drop would suddenly change its shape, sometimes with an increase in θ accompanying a decrease in R , and sometimes with a decrease of both θ and R [20]. Generally, surface roughness is the origin of contact line pinning [21]. Particle existence in a droplet enhances the pinning effect [22–24].

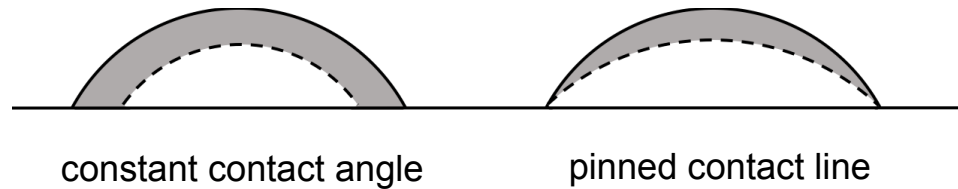


Figure 1.1. This figure shows the two pure modes of droplet evaporation. The right is the fixed-contact angle mode: a droplet with a constant contact angle. The left is the pinned-contact line mode: a drop with a constant contact area, or a pinned contact line. The solid line shows the drop before evaporation, and the dashed line shows the drop after part of liquid evaporates.

In the contact-line-pinning mode, the behavior of the contact angle change is called the "contact angle hysteresis" [25]. For a certain drop, there is an equilibrium contact angle θ_E calculated according to the Young-Dupre equation as

$$\cos\theta_E = \frac{\sigma_{SV} - \sigma_{SL}}{\sigma_{LV}}, \quad (1.1)$$

where σ_{SV} , σ_{SL} , σ_{LV} are the surface tensions between the solid-vapor, solid-liquid, and liquid-vapor phases, respectively. However, an evaporating drop is usually not at an equi-

librium state in terms of the contact angle, especially when evaporation is under a pinned contact line mode. The range of the contact angle change is between a maximum and a minimum contact angle. The maximum angle is called the advancing contact angle θ_A , and the minimum is called the receding contact angle θ_R . A drop can keep the contact line pinned with a metastable contact angle between θ_A and θ_R . A drop with a larger θ_E often has a smaller hysteresis range [26], thus more likely to evaporate in the constant contact angle mode.

This work focuses on a sessile drop evaporating in the pinned contact line mode till late stage. This is the kind of evaporation where the coffee-ring effect occurs.

1.1.2 Evaporation Rate and Flux

The evaporation speed of a drop has been long studied. Maxwell in 1877 first worked on drop evaporation in still air by assuming that the vapor outside an evaporating drop is at quasi-steady state [27]. The quasi-steady evaporation is widely applied later in solving problems of droplet evaporation. Harry W. Morse first studied sessile drop evaporation on a substrate in 1910. He concluded from experiments of iodine drops that the evaporation rate is proportional to the droplet radius rather than its surface area, as $\frac{dm}{dt} = -kr$, where m is the liquid mass, r is the radius, and k is a constant [28]. Langmuir further explained the proportionality in 1918 by using the analogy between vapor diffusion and heat conduction based on the quasi-steady mode [29]. The conclusion that the drop bottom radius determines the evaporation rate also applies to water drops on glass according to Birdi's experiments [30]. Birdi also showed that when a drop evaporates in a pinned-contact-line mode, the evaporation rate remained unchanged [31].

The evaporation flux along the surface of a spherical-cap shaped sessile drop has also been widely studied. In theoretical studies of drop evaporation, two kinds of evaporation flux are common: a hydrodynamic model and a kinetic model. They care about different limiting steps of evaporation. The kinetic model believes that the mass transfer across the liquid-air interface is the limiting step, and the hydrodynamic model treats the diffusion of

vapor molecules as the limiting step. Clearly, the quasi-steady evaporation rate adopts the hydrodynamic model.

The kinetic model is necessary for the following kinds of problems. First is when evaporation happens at a temperature close to the boiling point. Heat pipes belong to this kind of condition [32] [33]. Second, evaporation happens in some extreme conditions, such as evaporation under vacuum [34], low temperature evaporation [35], high pressure background [36]. Last, microscopic studies of evaporation near the CL, including drop impact [37,38] and evaporation with CL depinning [35], use the kinetic evaporation model. Because the CL in microscopic view is a thin layer, the disjoining pressure, which describes microscopic behaviors between the drop and the substrate, affects the mass transfer and is included in the model [39–41].

From macroscopic level, it is sufficient to model evaporation with quasi-steady assumption. This assumption has reached agreement with experiments in terms of both evaporation speed and coffee ring growth [42], while kinetic model yielded a compromised coffee ring effect [38]. The quasi-steady assumption requires the air around the drop to be still, then the evaporation flux is controlled by vapor diffusion. Under this condition, although the net evaporation rate remains constant, the evaporation flux distribution changes with θ . The flux is integrably singular at the contact line of the droplet [20,43]. Deegan used the analogy between the diffusive flux outside a drop and the electrostatic potential surrounding a conducting wedge, and concluded that the evaporation flux is a function of the radial position along the drop surface [1]:

$$\tilde{J} \propto (R - \tilde{r})^{-\lambda} \quad (1.2)$$

where $\lambda = (\pi - 2\theta)/(2\pi - 2\theta)$, \tilde{r} is the horizontal distance between the point and the center of the drop base, and θ is the contact angle, which changes with the evaporation time. The singularity can be eliminated if disjoining pressure is incorporated in the model, but this is not going to be done in our work since it needs extra computational efforts.

Hu and Larson solved the drop evaporation rate and flux by an FEM model [43]. By fitting the FEM simulation results, they gave an expression for the evaporation rate for a drop with a contact angle no larger than 90° . Their expression agreed well with previous

analytical models, such as Picknett and Bexon's result [20]. Besides, their results confirmed the flux singularity with an asymptotic equation of the evaporation flux (in a dimensionless form):

$$J = J_{0(\theta)}(1 - r^2)^{-\lambda(\theta)}, \quad (1.3)$$

where r is the dimensionless distance from the axis of symmetry ($0 \leq r \leq 1$) and θ is the contact angle. The equations for $J_{0(\theta)}$ and $\lambda(\theta)$ are $J_{0(\theta)} = (1 - Hum)(0.27\theta^2 + 1.30)[0.6381 - 0.2239(\theta - \pi/4)^2]$ and $\lambda(\theta) = 0.5 - \theta/\pi$. This results have been widely used in other numerical research for a spherical-cap-shaped evaporating drop [44,45].

1.1.3 Flow Types in an Evaporating Drop

Microfluidic flow in sessile drop evaporation is worth studying because it affects the colloidal deposition. Understanding the development of the flow patterns is crucial for elucidating and controlling the deposition patterns of colloidal particles in an evaporating drop.

The flow causing the coffee-ring effect is an edgeward capillary flow. The capillary flow is caused to replenish the mass loss due to evaporation in the periphery of the pinned contact line [1, 42, 46]. Particles, if there are any, are convected the contact line with the capillary flow, and deposit near the contact line. This contact line deposition forms the ring-shape which is the "coffee ring". Studies on drop evaporation can never dismiss this flow. Many research, especially theoretical research on colloidal drop evaporation, cared only about the capillary flow due to the complexity of the problems [47–49].

Another important flow in an evaporating drop is Marangoni flow. Marangoni flow is caused by variations of the surface tension, and is in the opposite direction from the surface gradient of the surface tension $\nabla_s \sigma$ (σ is the surface tension). The surface tension gradient can be caused by variations in temperature, solvent composition [50–52] and surfactant distribution [53, 54]. Unlike the capillary flow which is always from the center to the periphery, Marangoni flow direction changes with time and location. A common Marangoni flow direction in drop evaporation is along the drop surface from the contact line to the

top, forming a circulation flow together with capillary flow as figure 1.2b. Depending on the material properties and evaporation time, Marangoni flow is not always in the same direction, though. The circulation can be clockwise, counter-clockwise or multi-directional. These new flow patterns, compared to the pure capillary flow pattern (figure 1.2a), change the deposition time [55] and the deposition patterns [56, 57] for the dispersed particles if there are any. Further discussion on Marangoni flow in drop evaporation is in the next section.

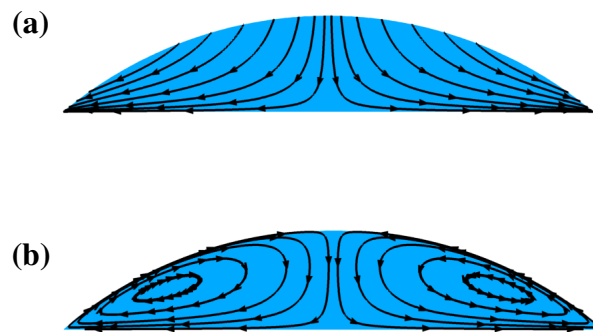


Figure 1.2. Flow profiles of (a) capillary flow only, and (b) circulation forming by capillary flow and Marangoni flow

Bouyancy-driven flow sometimes affects the flow pattern as well, especially when the drop is heated. An evaporating drop is cooler at the drop surface due to evaporation cooling. So a temperature difference exists between the drop surface and the drop base, resulting in a density difference. A gravitational Bond number $B = \frac{\rho g h \alpha}{\beta}$ (where ρ is density of the fluid, h is the drop height, α is the water thermal expansion coefficient, and β is the derivative of surface tension with respect to temperature) can be used to determine the importance of buoyancy-driven flow [58]. For a water drop, buoyancy-driven flow is not important because of a small B [59], which was also validated by numerical results [60]. add explanation of β to the Marangoni flow paragraph.

1.1.4 Marangoni Flow

Marangoni flow, observed as early as the 1800s [61], is caused by surface tension gradient along an interface which results in the fluid flow from the low-surface-tension region to high-surface-tension region. Such flow exists in an evaporating drop and form a circulation flow profile together with the edgeward capillary flow. In this section, temperature-induced Marangoni flow, which is called thermal Marangoni flow, will be discussed.

The relation between surface tension and temperature is linear for a small temperature change, and the coefficient β is negative for most liquid. This means the high temperature region is the low surface tension region. Thus Marangoni flow is from high temperature region to low temperature region.

1.1.4.1 Observation of Marangoni flow

The existence of Marangoni flow in an evaporating droplet has been experimentally observed by tracking particles in water drops as well as other organic drops.

Early Marangoni flow observation was on organic drops, because Marangoni flow in pure water drops is hard to observe since water is easily contaminated [62]. In 2002, Savino used tracers of $20\mu m$ to characterize the flow of a hanging n-octane drop with a base radius of $1.5mm$ [63]. In 2006, Hu and Larson observed the flow in a sessile octane drop [64]. These two papers both reported strong Marangoni flow.

Later Xu first reported Marangoni flow in water drops by observing tracking particles near the contact line [65]. He used a water drop with a base radius of $2mm$ and an initial contact angle of 10° on a glass substrate. With a microscopic under the transparent glass substrate, he observed particles moving toward the contact line and then moving away. This indicated a circulation flow pattern.

Recently, 3D particle tracking allows precise observation of flow in drops. Therefore, more people observed Marangoni flow in evaporating water drops. In 2013, Trantum et al. used optical coherence tomography to track the motion of $1\mu m$ carboxylated polystyrene particles in an $1\mu L$ water drop on a glass slide [66], and saw Marangoni eddies. In 2015,

Marin used astigmatism particle tracking velocimetry (APTV) to observe water drops on a glass slide [67]. $2\mu\text{m}$ polystyrene particles coated with sulfate groups were used as tracking indications. They observed Marangoni flow toward the center of the drop in both a surfactant-free water drop and a surfactant-laden drop.

It is easier to observe Marangoni flow when a drop is heated [68,69], because Marangoni flow is stronger with greater temperature difference.

1.1.4.2 Theories of Thermal Marangoni Flow

The relation between surface tension and temperature is linear for a small temperature change, and the coefficient β is constant and negative for most liquid. This means the high temperature region is the low surface tension region. So we say Marangoni flow is from high temperature region to low temperature region.

A counterclockwise of Marangoni flow pattern was obtained by the numerical results of Girard et al [59, 70]. They used finite element method to model Marangoni flow caused by inconsistent temperature along the drop interface. The surface temperature was always lower at the top and higher at the CL. However, their model was not rigorous since evaporative cooling was not included.

Thermal Marangoni flow can be clockwise or counterclockwise, according to Hu and Larson's research [46]. They studied droplet evaporation using both analytical solutions and numerical methods. The lubrication theory approximation was used for the analytical solution, and the finite element method was used for the numerical model. The two solutions agreed well with each other. Their lubrication theory can be used to predict flow velocities for a drop with a contact angle as high as 40° .

There are two causes of temperature gradient along the interface: the nonuniformity of heat diffusion and the nonuniformity of evaporative cooling. Heat diffusion tends to result in temperature higher near the CL due to a shorter diffusion path from the drop bottom, while evaporative cooling tends to result in temperature lower near the CL due to the divergent evaporation flux. The two factors compete with each other. Heat diffusion nonuniformity is dominant at early stage of evaporation, and evaporative cooling non uniformity dominates

the later stage. Therefore, Hu and Larson's numerical results showed that the circulation flow changes from counterclockwise to clockwise as the drop evaporates [46]. These conclusions were based on the assumption that the drop base is at constant temperature, viz. uniform temperature in the substrate.

Later Ristenpart gave an analytical result showing that the direction of the circulation depends on the relative thermal conductivity k_R , which is a ratio of the substrate and the liquid conductivity [71]. From solving heat diffusion near the contact line region, a criteria was given to decide the direction of the circulation based on k_R and the contact angle θ . The results were validated with experiments by observing the final deposition patterns with different fluids. Further, Xu incorporated the thickness of the substrate where the drop rests, and generalized the criteria [72]. These criteria judge the direction of Marangoni flow according to the temperature gradient direction near the CL, instead of the temperature all across the surface. This ruled out the possibility of multi-vortices.

1.1.4.3 Stagnation Points

Recent numerical results started to reveal multi-vortices of Marangoni flow [60,73,74], while the above results assumed monotonous temperature change along the drop surface. The multi-vortices implied the existence of stagnation points, where the surface flow is zero, on a drop surface between two vortices.

The existence of stagnation points was also observed by different groups with experiments of water drops [65,66,68], but not well explained. In 2007, when Xu et al. verified the existence of Marangoni flow in water drops, he also observed a stagnation point less than $17\mu m$ away from the contact line [65]. Li et al. also reported that the stagnation point they observed was less than $50\mu m$ away from the contact line [68].

According to results of Barash et al. [73,74] and Bouchenna et al. [60], the explanation to the stagnation points was the direction change of Marangoni stress on the surface. However, the numerical results and the experimental results don't coincide in terms of the radial positions of the stagnation points. Therefore, the mechanism of stagnation points near the CL as what were observed in the experiments needs further studying.

The existence of stagnation points implies the complication of the surface flow in an evaporating drop. The surface flow is significant in drop evaporation study because particles, if there are any in the drop, aggregate and even adsorb to the surface during evaporation. Hence, the surface flow affects particle behaviors significantly and is worth studying.

1.2 Particle Behaviors in an Evaporating Drop

Final particle deposition patterns are governed by particle behaviors during drop evaporation. The most famous particle behavior in an evaporating drop is the coffee ring effect where particle deposition occurs near the contact line. The following additional particle behaviors have been reported in the literature.

1.2.1 Particle Adsorption, Coagulation, Convection and Diffusion

Particle behaviors that were studied include particle diffusion, convection, adsorption to the substrate, adsorption to the drop surface, and particle coagulation.

Small particles diffuse because of their Brownian motion. The diffusion coefficient of particles D_p can be expressed by the Einstein-Stokes equation because we assume a dilute particle concentration of very small particles:

$$D_p = \frac{k_B T}{6\pi\mu r_p}, \quad (1.4)$$

where k_B is the Boltzman constant, T is temperature, μ is liquid viscosity, and r_p is particle radius. The diffusion effect is stronger for particles with a smaller radius, because D_p is reversely proportional to the particle radius.

The particles are also convected as there is flow of the liquid in the evaporating drop. Thus, the particle concentration is coupled with flow patterns inside the drop. If the system is treated as a continuum, the convection-diffusion equation of mass transfer can be used to model the particle concentration distribution. The Peclet number $Pe_p = v_c l_c / D_p$ represents the ratio of mass convection and mass diffusion of particles.

The coffee ring effect is a product of particle convection during drop evaporation. The growth of the ring during evaporation has drawn the attention of researchers. Berteloot

et al. analyzed the growth of the ring in the radial direction due to geometry constraint and concluded a length scale of $t^{\frac{2}{3}}$ [49]. They proposed a model that the location of the evaporation flux singularity gradually moves inward to the front of the ring deposition. Bhardwaj et al. numerically studied the ring growth by assuming the contact line moved inward onto the deposited ring structure [75]. A certain contact angle for the phase line of the fluid, the particle bed and air was used. They both proved that their theoretical work reached agreements with experiments.

Particle convection affected by Marangoni flow largely change the ring deposition. The ring deposition was observed to be thinner when the drop was heated, which was attributed to stronger Marangoni flow. [76]. Parsa et al. even observed secondary rings when the drop was heated [77]. The distance between the CL ring and the secondary ring was smaller for higher temperature, which implied the stagnation point was further away from the CL for higher temperature. However, Li et al. found that the stagnation point was closer to the CL by observing the turning point of particle traces [68]. The contradiction between work of Li et al. and Parsa et al. requires further elucidation of drop deposition patterns during pendant drop evaporation.

Early studies on Marangoni flows in drop evaporation mainly focused on uni-directional (clockwise or counterclockwise) circulations and believed that counterclockwise circulations suppressed the “coffee ring effect” [64] and the clockwise circulations do not [71,72]. Later, multi-circulations were observed with numerical simulations [60,73,74,78,79]. However, Understanding of the influences of multi-circulations on particle deposition is still limited.

Experiments of particle traces and deposition patterns have shown ring deposition in spite of Marangoni flows. Experiments with polystyrene particles in water drops on glass substrates were done by Li et al. [80]. While counterclockwise circulations were observed during evaporation, the final deposition with room temperature still presents “coffee rings”. This contradicts the previous conclusions of counterclockwise circulations suppressing the “coffee ring effect”.

Other than particle diffusion and convection in the bulk phase, particles also adsorb to interfaces, including the drop-substrate interface and the drop-air interface. We will call the drop-air interface as “drop surface” in the following context. The adsorption is affected by the materials of particles and substrates. The essence of the adsorption is microscopic electrostatic behaviors. Therefore, the surface charge of particles affect the adsorption greatly. Some models are used to simply this aspect of the problem by employing the Damkholer number, $Da = k_d l_c / D_p$, where k_d is particle adsorption rate. The Damkholer number is the ratio of the rate of adsorption to the rate of diffusion.

1.2.2 Adsorption to the Substrate

The effect of particle adsorption was studied by experiments. Yan et al. experimented with charged polystyrene(PS) particles in water drops on charged substrates and observed particle deposition patterns [81]. They found that the usage of opposite charged particles and substrates, which means strengthened attraction between particles and substrates, resulted in particle deposition at the inner region of the droplet and much looser “coffee rings”. Later, Dugyala et al. calculated from DLVO (Derjaguin-Landau-Verwey-Overbeek) theory the interaction energy between particles and substrates at different pH environment and observed the deposition patterns after evaporation. Their results indicated that as particle-substrate attraction increases, a uniform film is obtained [82].

The deposition of Brownian particles that interact with a solid surface behaves as a first-order reaction, where the coefficient of the reaction is derived from the interaction potential [83]. Widjaja used this theory to simulate particle adsorption on the substrate during drop evaporation in 2008 [84]. After simulations with the finite element method, final deposition patterns were derived from the surface concentration of the particles. Various deposition patterns, including a ring deposition and a uniform deposition, were achieved, and the patterns were influenced by different values of Pe_p and Da . The larger Da is, the more suppressed is the coffee-ring effect. A larger Da means the adsorption effect is stronger, which can be produced by a strong attraction between particles and the substrate.

Recently, a more comprehensive model was developed to describe the behaviors of particle aggregates. A 1-D model given by Zigelman et al. accounted for particle convection, coagulation and adsorption to the substrate at the same time [85]. For adsorption, the first-order reaction model was used. It is a breakthrough that they described the behaviors of particle aggregates comprising of i particles, and solve a series of equations for each i value. Due to computation capacity limit, the trade-off is that the model, for the convection part, used an assumed velocity field derived from mass balance. A questionable assumption is that the evaporation flux was assumed to be constant along the drop surface. At last, both their analytical and simulation results indicated that a "central bump" deposition formed with $Da > 1$.

Apart from being treated as a continuum, particles can also be modelled microscopically using molecular dynamics simulations. Katiyar and Singh performed such simulations for the self assembly of particles during drop evaporation, where the temperature was assumed constant [86]. In the simulations, particle-substrate and liquid-substrate interactions were both included using LJ 12-6 potential energy function: $U_{LJ} = 4\epsilon[(\frac{\sigma}{r})^{12} - (\frac{\sigma}{r})^6]$, where ϵ and σ are interaction parameters. The pair energy of particles with the substrate $E_{NP-surface}$ is an indication of particle adsorption, and was varied by changing ϵ value for the particle-substrate and the liquid-substrate interactions. Their results showed that the ring shape deposition was obtained with lower $E_{NP-surface}$ values.

It is noticeable that most theoretical research on particle deposition exclude Marangoni flow, and even the capillary flow was not precisely modeled in some work [85]. Hence, the influence of Marangoni flow on particle deposition still needs careful studies.

1.2.3 Particle Accumulation on the Drop-air Interface

Particles accumulate on drop surfaces if the surface shrinks down fast enough to capture particles. Narayanan and Wang observed the accumulation by small-angle x-ray scattering and proposed a "kinetic crushing model" [87]. In this model, if drop surface shrink rate is larger than particle random walk diffusion rate, accumulation occurs.

Bigioni et al. further proposed an “interfacial growth model”, where surface diffusion and desorption was considered [88]. The model requires one more condition for surface accumulation, which is an attractive interaction between the particles and the drop surface. The interaction was characterized by interfacial diffusion length δ , which can be influenced by surface tension, particle size, etc. If the location where a particle first impacts on the surface is less than δ , the particle adsorbs on the drop surface; otherwise it desorbs back to the bulk phase. Later Li et al. used this model to explain the enhanced particle accumulation at higher temperature [89].

The drop surface adsorption effectively suppresses the formation of the “coffee ring” and leaves a monolayer of particles at the end of drop drying if the number of particles dispersed in the drop is well controlled [88]. Particles trapped at the surface of the drop are prevented from accumulating at the contact line.

Beside surface diffusion, interparticle capillary attraction also facilitates the surface accumulation. Yunker experimented with ellipsoid particles. They observed the adherence of particles to the packed structures that already existed at the drop surface, as what is represented in Figure 1.3 [90]. This is the mechanism by which ellipsoid particles are prevented from forming the “coffee rings” deposits.

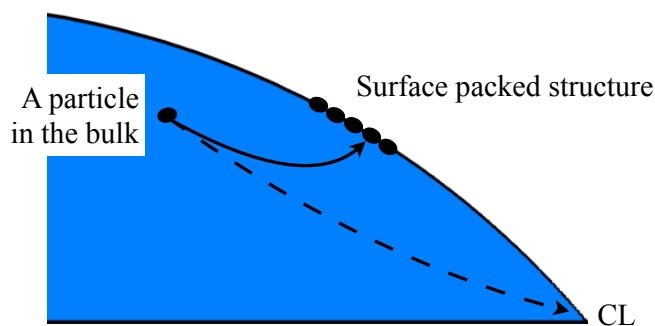


Figure 1.3. Ellipsoid particles presented obvious interparticle capillary attraction and a particle in the bulk phase adsorb to surface packed structures on their way to the contact line [90].

Al-Milaji and Zhao experimented with dual-droplet inkjet printing process, where two kinds of particles exist in a water-ethanol droplet and one kind of particles, the sulfate-PS particles, exists at the drop surface [91]. By observing the final deposition, they found that there were always a large portion of sulfate-PS particles deposited in the middle of the drop and formed a disk pattern. Their results were not well explained because the drop is complicated with two kinds of particles and two kinds of liquid, leading to possible complex Marangoni flow. However, it was at least valid to speculate from their experiments that Marangoni flow and surface accumulation can lead to deposition in the drop center.

Particle surface charge affects the surface accumulation according to the experiments by Anyfantakis et al [92]. By changing surfactant species and amount, they were able to manipulate particle surface charges from negative to neutral to positive. When particle surfaces are almost neutral, particles tend to accumulate on the drop surface due to their hydrophobicity and at last deposit into homogeneous patterns. Otherwise, ring deposition was formed.

To theoretically study the accumulation process, particle concentration gradient along the vertical direction needs to be considered, making theoretical studies complex. Thus the studies are far from enough.

While experiments proved the effectiveness of surface adsorption in suppressing the coffee ring effect, simulations have shown that the surface accumulation has to be coupled with Marangoni flow to achieve the suppression. If accumulation is included in the model but Marangoni flow is not, particles still reach the contact line at last, forming ring deposition. This conclusion was draw from both continuum modeling [93] and molecule dynamics (MD) simulations [94]. Yet, Zhao and Yong's MD simulations studied the influence of surface accumulation and concluded that the accumulation enhanced the particle density at the deposition center despite that it did not totally prevent the contact line deposition.

Since Marangoni flow seems essential in suppressing the coffee ring effect, a model including Marangoni flow to study "particle skin" at the drop surface was done by Maki and Kumar. They gave a mathematical model treating colloid with particles as continuum and numerically solved it by finite difference method [95]. Their results focused on the

particle concentration at the drop surface to study the “particle skin” at the drop surface. The simulations showed that Marangoni flows promote the formation of “particle skin”: the high concentration region first appeared near the contact line and later shifted to the top of the drop because Marangoni flow pull the ”skin” to the top. These results implied that surface flow has great influences on surface accumulation but previous studies on surface adsorption neglected these influences. On the other hand, their results showed that weak diffusion promotes the skin formation, which is consistent with Narayanan and Wang’s model [87]. Limits of Maki and Kumar’s work are that the evaporation flux was derived from the kinetic model and the CL was not pinned.

1.3 Objective of the Dissertation

The experimental observation of the flows or their influences is hard. One reason is that it is hard to observe the precise 3D movement of tracking particles or fluid. The other is that it is almost impossible to change factors at will in experiments. For example, the magnitude of Marangoni stress is determined by multiple factors including temperature change, particle concentration, properties of fluid. Therefore, it is impossible to change the Marangoni stress without other side effects. However, through simulations, it is possible to apply a certain Marangoni stress without changing other parameters. In this way, it is much easier to figure out the influence of a single factor.

Although flows inside an evaporating drops have been studied, Marangoni flows have not been as well understood as capillary flows. On the one hand, temperature-induced Marangoni flow may cause multi-circulations featured with several interesting phenomena like stagnation points and region segregation. These phenomena will be studied in this work. On the other hand, the clockwise circulation and the counterclockwise circulation behave differently and the magnitude of the Marangoni stress matters.

When particles are dispersed in the drop and adsorb to the substrate, the effects of Marangoni flows in different directions are even more complex. The particle distribution and the deposition speed of particles affected by Marangoni flows have rarely been investigated due to the difficulty of manipulating the direction or the magnitude of Marangoni

stresses/flows. In this work, the effects of fixed Marangoni stress was investigated as well as the temperature-induced Marangoni stress.

2. METHODS

A sessile evaporating colloidal drop on a substrate in ambient air at room temperature was modeled as continuum. The model was assumed axisymmetric. Cylindrical coordinates (r, z) were used, and the azimuth coordinate was neglected. The base of the drop is located at the height of $z = 0$, and has a radius of R (Figure 2.1). The drop rests on a substrate with a radius of l_s and a thickness of d . The contact line was assumed pinned till the contact angle reached below 3° or the simulations stopped converging. The material properties are shown in Table 2.1, which are for a water droplet on a glass substrate.

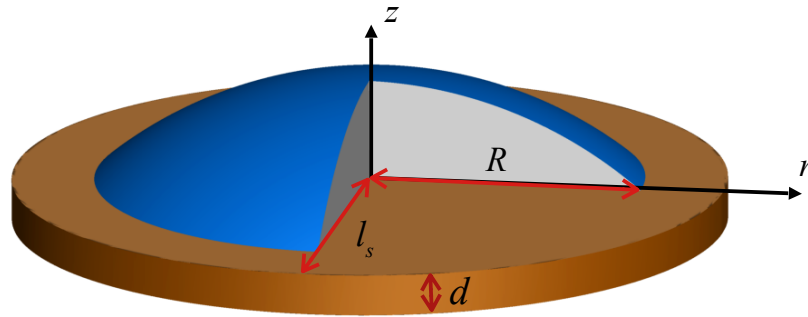


Figure 2.1. Cylindrical coordinates (r, z) were used, and the azimuth coordinate was neglected. The base of the drop is located at the height of $z = 0$, and has a radius of R .

The equations are going to be solved in dimensionless forms. Apart from the properties in Table 2.1, all variables use the following notations: tilde symbols refer to dimensional variables, while bare letters indicate corresponding dimensionless variables based on the characteristic values denoted by footprint " c " shown in Table 2.2.

Several assumptions were made in this dissertation: 1) Particle bulk concentration was so low that it does not affect the fluid properties. 2) Gravitational effects were neglected because the droplet is so small that gravitational Bond number $Bo_g = \rho g l_c^2 / \sigma$, which means

Table 2.1.
Simulation Parameters

Variable	Definition	Value	Units
R	drop base radius	1×10^{-3}	m
ρ	fluid density	9.97×10^2	kg/m ³
μ_0	viscosity	8.90×10^{-4}	Pa·s
k_l	liquid thermal conductivity	0.58	W/m/K
α	thermal diffusivity	1.39×10^{-7}	m ² /s
T_0	initial temperature	25	°C
Hum	relative humidity in air	0.5	-
σ_0	initial surface tension	71.91	dyn/cm
β	$\partial\tilde{\sigma}/\partial\tilde{T}$	-0.1657	dyn/cm/K
c_v	vapor saturation concentration	2.32×10^{-2}	kg/m ³
D	diffusivity of vapor in air	26.1×10^{-5}	m ² /s
H_v	latent heat of vaporization	2264.76	kJ/kg
k_s	substrate thermal conductivity	0.80	W/m/K
l_s	half length of the substrate	1.3×10^{-3}	m
d	substrate thickness	0.15×10^{-3} *	m
k_a	air thermal conductivity	0.024	W/m/K
r_p	particle radius	10	nm

* 0.15×10^{-3} is the value used for Section 3.2. In Section 3.3, $d = 0.5 \times 10^{-3}$ m is used.

Table 2.2.
Characteristic Variables

Variable	Definition	Value	Units	Dimensionless variable
length	$l_c = R$	1×10^{-3}	m	$l = \tilde{l}/l_c$
velocity	$v_c = \frac{Dc_c}{\rho l_c}$	6.5×10^{-7}	m/s	$u = \tilde{u}/v_c, v = \tilde{v}/v_c$
time	$t_c = l_c/v_c$	1.5×10^3	s	$t = \tilde{t}/t_c$
surface tension	$\sigma_c = \sigma_0$	71.91	dyn/cm	$\sigma = (\tilde{\sigma} - \sigma_0)/\sigma_c$
temperature	$T_c \approx H_v Dc_c/k_l^*$	1.0	K	$T = (\tilde{T} - T_0)/T_c$
stress	$\tau_c = \mu_0 v_c/l_c$	5.8×10^{-7}	Pa	$\tau = \tilde{\tau}/\tau_c$
pressure	$p_c = \sigma_c/l_c$	71.97	Pa	$p = \tilde{p}/p_c$
particle concentration	$c_{pc} = c_{p0}$	2.5	kg/m ³	$c_p = \tilde{c}_p/c_{pc}$
particle surface concentration	$\Gamma_c = c_{p0} \cdot l_c$	2.5×10^{-3}	kg/m ²	$\Gamma = \tilde{\Gamma}/\Gamma_c$

* $H_v Dc_c/k_l = 2.5$ K. We used $T_c = 1.0$ K because it facilitates the transformation from the dimensionless temperature to dimensional temperature.

Table 2.3.
Dimensionless Groups

Variable	Definition	Value
Re	$Re = \rho v_c l_c / \mu_0$	7.4×10^{-4}
Ca	$Ca = \mu_0 v_c / \sigma_c$	8.1×10^{-9}
Pe	$Pe = v_c l_c / \alpha$	4.7×10^{-3}
Pe_p	$Pe_p = v_c l_c / D_p$	26.7
REH	$REH = \frac{H_v D_{c_c}}{k_l T_c}$	2.5
k_R	$k_R = k_s / k_l$	1.4
F_0	$F_0 = \alpha_s \frac{l_c}{l_c^2}$	1.4
Da	$Da = \frac{k l_c}{D_p}$	change with k

the buoyancy is negligible compared to the capillary stress. 3) Furthermore, gravitational effects on the particles are also negligible since the particles are 10 nm in size where Brownian forces dominate over gravitational forces. 4) If Marangoni flows are caused by temperature change, a comparison between the Marangoni stress and the buoyancy force due to temperature change indicated that the buoyancy force was negligible as follows. A Bond number $B = \frac{\Delta \rho g l_c^2}{\Delta \tilde{\sigma}}$ is the ratio between buoyancy force and the Marangoni stress. Density change $\Delta \rho$ and surface tension change $\Delta \tilde{\sigma}$ are both caused by a temperature change $\Delta \tilde{T}$ by $\Delta \rho = \rho \alpha_V \Delta \tilde{T}$ and $\Delta \tilde{\sigma} = \beta \Delta \tilde{T}$ respectively, where $\alpha_V = 2.07 \times 10^{-4}$ is the volumetric thermal expansion coefficient of water. Then $B = \rho g l_c \alpha_V / \beta \approx 10^{-5}$ is small, indicating the validity of neglecting the buoyancy force.

2.1 Governing Equations

The domains in our model include the drop domain and the substrate domain. The dimensionless groups coming from non-dimensionalization are listed in Table 2.3.

Inside the drop, five variables were solved, which are velocity \mathbf{v} (including radial velocity u and axial velocity v), pressure p , temperature T and particle concentration c_p .

The fluid phase was assumed Newtonian and incompressible. The continuity equation 2.1 and the Cauchy momentum equation 2.2 determine the flow of the fluid:

$$\nabla \cdot \mathbf{v} = 0, \quad (2.1)$$

$$Re \cdot \left(\frac{\partial \mathbf{v}}{\partial t} + \mathbf{v} \cdot \nabla \mathbf{v} \right) = \nabla \cdot \mathbf{T}, \quad (2.2)$$

where the stress tensor $\mathbf{T} = -(1/Ca) \cdot p\mathbf{I} + \mu \left[\nabla \mathbf{v} + (\nabla \mathbf{v})^T \right]$ and $Ca = \tau_c/p_c$. $\mu = \tilde{\mu}/\mu_0$ is the dimensionless viscosity that changes with the particle concentration c_p according to the Krieger-Dougherty relationship [96]:

$$\mu = \left(1 - \frac{c_p}{c_{pm}} \right)^{-2}, \quad (2.3)$$

where μ_0 is the viscosity of pure liquid. Here the force balance includes the inertia and the viscous stress, and the ratio of the former to the latter is given by Reynolds number Re .

The heat transport in the drop was modeled by the heat convection-diffusion equation:

$$Pe \left(\frac{\partial T}{\partial t} + \mathbf{v} \cdot \nabla T \right) = \nabla^2 T. \quad (2.4)$$

The particle dynamics in the drop were described as continuum by the convection-diffusion equation:

$$Pe_p \left(\frac{\partial c_p}{\partial t} + \mathbf{v} \cdot \nabla c_p \right) = \nabla^2 c_p, \quad (2.5)$$

where c_p is the dimensionless particle concentration, $Pe_p = v_c l_c / D_p$ is the Peclet number for mass transfer which is the ratio of particle convection to diffusion. D_p is the diffusion coefficient of particles, which was given by Einstein-Stokes relation:

$$D_p = \frac{k_T}{6\pi\mu_0 r_p}, \quad (2.6)$$

where r_p is the particle radius.

In the substrate domain, only one governing equation of heat conduction was solved by

$$\frac{\partial T_s}{\partial t} = F_0 \nabla^2 T_s, \quad (2.7)$$

where T_s is temperature of substrate, F_0 is Fourier number that describes the ratio of heat conduction and heat storage.

2.2 Boundary Conditions

There are five boundaries that need boundary conditions: the drop surface $z = h(r, t)$, $0 \leq r \leq 1$ (h is the height of the drop which changes with locations and time), the drop-substrate interface $z = 0$, $0 \leq r \leq 1$ (also called the drop base), the substrate lower surface $z = -d$, $0 \leq r \leq l_s$, the axis of symmetry $r = 0$ and the substrate-air interface $z = 0$, $1 < r \leq l_s$.

On the drop surface, there are mass balance for the fluid, momentum balance for the fluid, heat balance for the fluid and mass balance for the particles. The mass balance is between surface movement, fluid velocity and evaporation, that is given by kinetic boundary condition:

$$\mathbf{n} \cdot (\mathbf{v} - \mathbf{v}_s) = J, \quad (2.8)$$

where \mathbf{n} is the surface normal vector shown in Figure 2.2, $\mathbf{v}_s = (dr/dt, dz/dt)$ is the velocity of the surface, J is the dimensionless evaporation flux. The evaporation flux is solved from quasi-steady state vapor diffusion in the air domain $\nabla^2 c = 0$ (c is the vapor concentration). However, in order to save computational efforts, we did not incorporate the air domain and employed the forms of the flux J derived by Hu and Larson [43]:

$$J = J_{0(\theta)} (1 - r^2)^{-\lambda(\theta)}, \quad (2.9)$$

where r is the radio position ($0 \leq r \leq 1$) and θ is the contact angle. The term $(1 - r^2)^{-\lambda(\theta)}$ means the integrable singularity at the contact line $r = 1$. The equations for $J_{0(\theta)}$ and $\lambda(\theta)$ were $J_{0(\theta)} = (1 - Hum) (0.27\theta^2 + 1.30) [0.6381 - 0.2239(\theta - \pi/4)^2]$ and $\lambda(\theta) = 0.5 - \theta/\pi$. The employment is valid because both the capillary number and the gravitational Bond number is so small that the drop remains a spherical-cap shape, which was an assumption in Hu and Larson's work.

The momentum balance on the surface consists of internal stress and surface stress including capillary stress and Marangoni stress:

$$C\mathbf{a}\mathbf{n} \cdot \mathbf{T} = -2\mathcal{H}\sigma\mathbf{n} + \nabla_s\sigma, \quad (2.10)$$

where $2\mathcal{H}$ is twice the mean curvature. The Marangoni stress term $\nabla_s\sigma$ is the change of surface tension along the surface.

Two kinds of imposition of Marangoni stresses were used. First, the Marangoni stresses are caused by the temperature change due to evaporative cooling and heat transport. Then $\frac{d\sigma}{dT} = \beta \frac{T_c}{\sigma_c}$, where $\beta = \partial\tilde{\sigma}/\partial\tilde{T}$ is constant for a small range of temperature change, meaning the surface tension is linearly related to temperature. As a result, Equation 2.10 is substituted by

$$Ca\mathbf{n} \cdot \mathbf{T} = -2\mathcal{H}\sigma\mathbf{n} + \left(\beta \frac{T_c}{\sigma_c}\right) \nabla_s T. \quad (2.11)$$

Second, to acquire general understanding on the effects of the directions and the magnitudes of the Marangoni stress, fixed Marangoni stresses were applied. A Marangoni number $Ma = \frac{\Delta\tilde{\sigma}}{\mu_0\nu_c}$ stands for the ratio of Marangoni stresses and viscous stresses (also the dimensionless Marangoni stress τ_{Ma}). To use certain magnitude of Marangoni stresses, Equation 2.10 is changed to

$$Ca\mathbf{n} \cdot \mathbf{T} = -2\mathcal{H}\sigma\mathbf{n} + Ca \cdot Ma\mathbf{t}, \quad (2.12)$$

where \mathbf{t} is the unit tangential vector, shown in Figure 2.2, whose direction is in the direction where r increases. If the Marangoni stress is in the same direction as \mathbf{t} , then Ma is a positive value, vice versa. The results with a fixed Marangoni stress are valid for broader cases, since the Marangoni stress can be caused not only by the temperature change, but also solvent composition, surfactant distribution, etc.

The temperature distribution at the drop surface is influenced by the heat balance between diffusion and the evaporative cooling. The evaporative cooling flux is proportional to the evaporation mass flux \tilde{J} as $H_v\tilde{J}$ where H_v is the latent heat of vaporization. So the balance is given as

$$REH \cdot J = -\mathbf{n} \cdot \nabla T, \quad (2.13)$$

where relative vaporization heat $REH = \frac{H_v D_c c_c}{k_l T_c}$ is the ratio of evaporative cooling to diffusion.

The last boundary condition on the free surface is for particle concentration. Because no particles cross the surface, evaporated liquid leaves particles near the surface. Therefore, the condition is

$$Pe_p c_p \cdot J + \mathbf{n} \cdot \nabla c_p = 0. \quad (2.14)$$

At the drop-substrate interface, there is no slip, no penetration for the fluid:

$$\mathbf{v} = \mathbf{0}. \quad (2.15)$$

The heat flux from the substrate side and toward the drop is continuous, so

$$\mathbf{n} \cdot \left(\nabla T_s - \frac{1}{k_R} \nabla T \right) = 0, \quad (2.16)$$

where relative heat conductivity $k_R = k_s/k_l$ is the ratio of substrate heat conductivity to the liquid heat conductivity.

Particles do not cross the interface, meaning $\mathbf{n} \cdot \nabla c_p = 0$ if no deposition is considered. However, particles deposit on the substrate, i.e. the drop-substrate interface, which requires a surface concentration $\tilde{\Gamma}$ to represent the amount of the deposited particles. The deposition of particles before complete dryness of the drop is in essence an adsorption of particles onto the substrate, which can be described as a first-order reaction [83]:

$$\frac{\partial \tilde{\Gamma}}{\partial t} = k \cdot \tilde{c}_p, \quad (2.17)$$

where k represents the reaction constant of the first-order reaction of adsorption. As a result, the BC of particle concentration at the substrate surface is:

$$\mathbf{n} \cdot \nabla c_p + Da c_p = 0, \quad (2.18)$$

where $Da = \frac{k l_c}{D_p}$ represents the ratio of adsorption flux to diffusion flux.

The substrate lower surface was assumed to be at constant temperature, same as the ambient temperature T_0 , so $T = 0$. There is assumed to be no heat flux ($\mathbf{n} \cdot \nabla T = 0$) at the substrate-vapor interface and at the far end of the substrate ($r = l_s$ where l_s is the half length of the substrate).

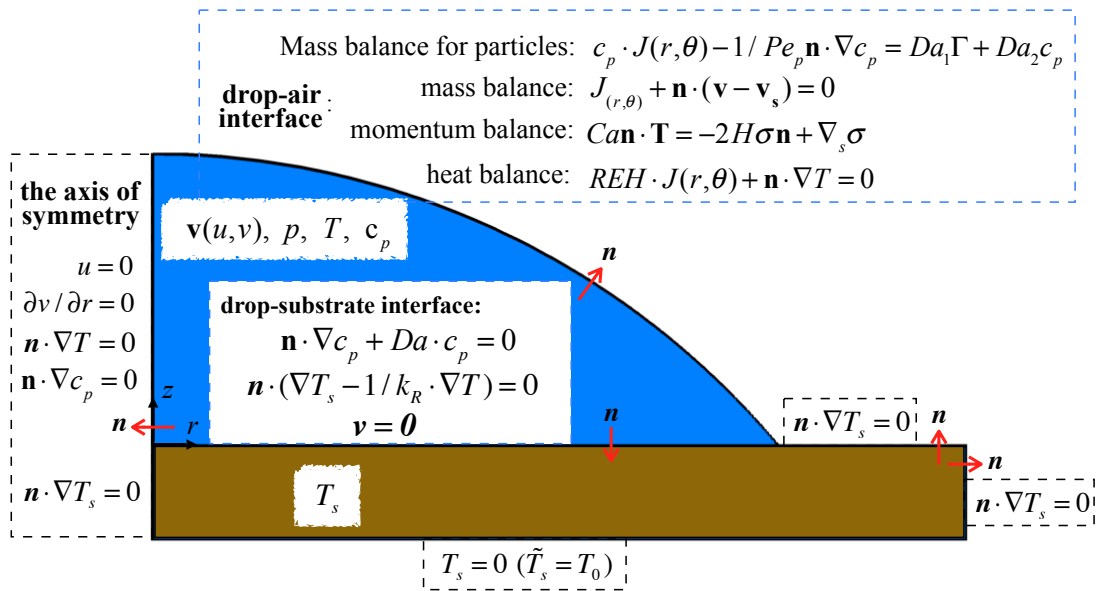


Figure 2.2. Boundary conditions

At the axis of symmetry, the boundary conditions of axisymmetry were imposed as Figure 2.2. Figure 2.2 also shows a summary of all the above boundary condition.

There is one more condition, pinning, at the contact line. The pinning was defined by a boundary condition of $r = 1$.

The initial conditions were $\mathbf{v} = \mathbf{0}$, $T = 0$ (which is $\tilde{T} = T_0$), $c_p = 1$ (which is $\tilde{c}_p = c_{p0}$). The initial contact angle was $\theta = 50^\circ$.

2.3 Numerical Method

This coupled system of second-order partial differential equations (PDEs) is solved numerically by employing the Galerkin finite element method (G/FEM).

We first discretized the drop domain and the substrate domain into small elements. A relatively coarse example of the mesh for spatial discretization is shown in Figure 2.3. In real computation, the numbers of elements we used are as follows: $NEL = 8$, $NEM = 200$, $NEV = 50$, $NES = 5$. A total of 4554 elements with 21 radial elements were used. The real mesh is shown by Figure 2.4. We also computed with an even denser mesh. The results are exactly the same with the mesh in Figure 2.4 and with the denser mesh used for checking precision as shown by Figure 2.5. The interpretation of this figure in the Results part, but it at least shows that the results with the two mesh sets are the same. This is to validate that our results are valid and not subject to mesh distribution.

Over the discretized domains, variables are interpolated via a mixed interpolation scheme. All the variables but the pressure p , including the velocities u , v , the temperature T and the particle concentration c_p , were interpolated upon biquadratic basis functions as 2.19, while

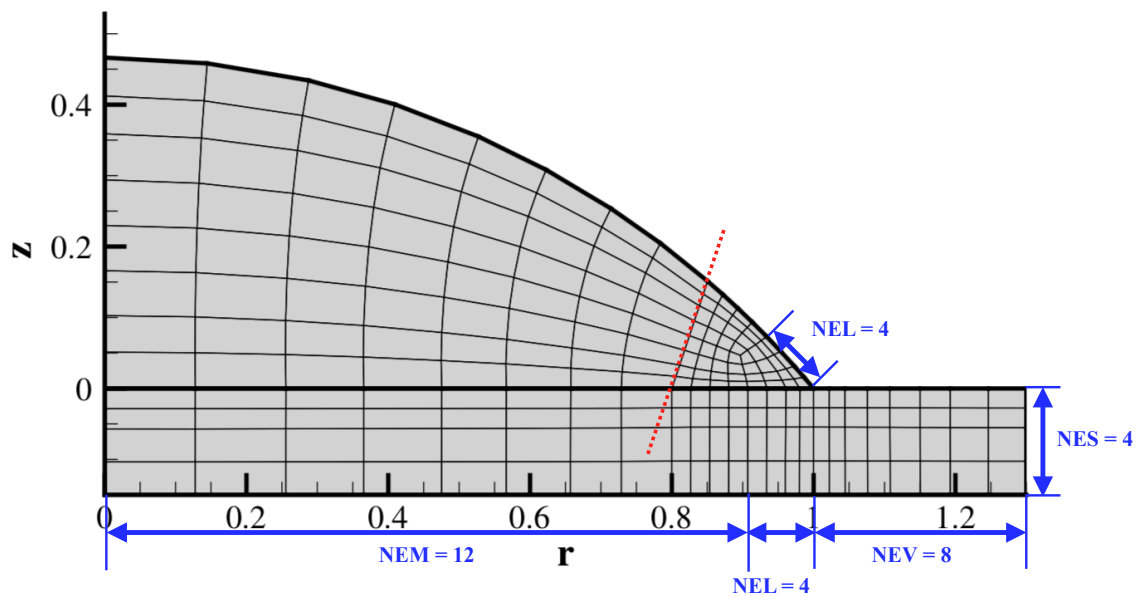


Figure 2.3. A coarse example of the mesh distribution. The red dashed line shows the algebraic mesh restriction.

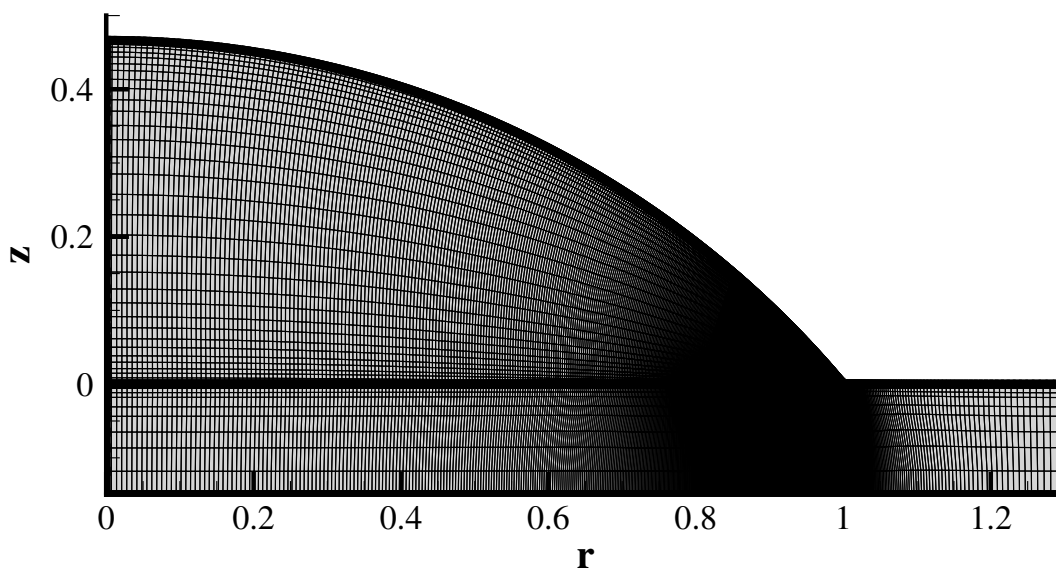


Figure 2.4. The actual mesh used for computation.

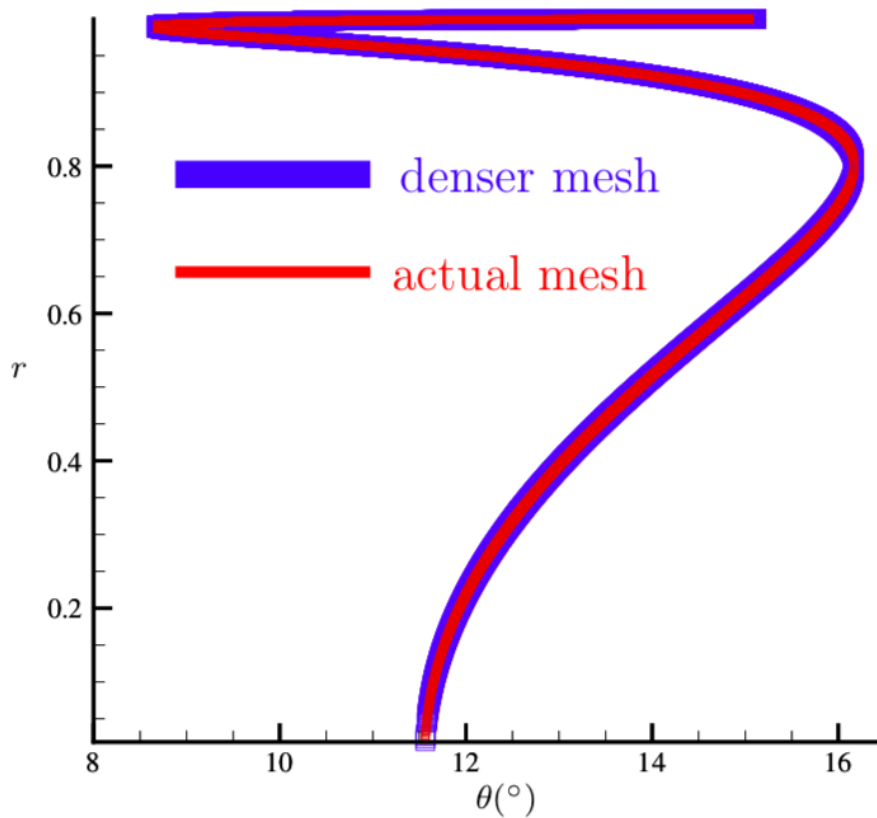


Figure 2.5. The comparison of the results with 2 mesh distribution: (1) the mesh actually used for results; (2) a even denser mesh to validate precision. The overlap proves the mesh in Figure 2.4 to be sufficient.

the pressure p is interpolated upon bilinear basis functions as 2.20. The basis functions are given below:

$$\begin{aligned}
\phi^1 &= (1 - 3\xi + 2\xi^2)(1 - 3\eta + 2\eta^2) \\
\phi^2 &= 4(\xi - \xi^2)(1 - 3\eta + 2\eta^2) \\
\phi^3 &= (-\xi + 2\xi^2)(1 - 3\eta + 2\eta^2) \\
\phi^4 &= (1 - 3\xi + 2\xi^2)4(\eta - \eta^2) \\
\phi^5 &= 4(\xi - \xi^2)4(\eta - \eta^2) \\
\phi^6 &= (-\xi + 2\xi^2)4(\eta - \eta^2) \\
\phi^7 &= (1 - 3\xi + 2\xi^2)(-\eta + 2\eta^2) \\
\phi^8 &= 4(\xi - \xi^2)(-\eta + 2\eta^2) \\
\phi^9 &= (-\xi + 2\xi^2)(-\eta + 2\eta^2)
\end{aligned} \tag{2.19}$$

$$\begin{aligned}
\psi^1 &= (1 - \xi)(1 - \eta) \\
\psi^2 &= \xi(1 - \eta) \\
\psi^3 &= (1 - \xi)\eta \\
\psi^4 &= \xi\eta
\end{aligned} \tag{2.20}$$

The details of interpolation and the finite element method formulation were presented in [97].

Temporal discretization was implemented with a second-order Adam-Bashforth adaptive time stepping method, which adapts time intervals with the changing rate of the variables. However, the first five steps used a fixed time step of 10^{-5} and simply backward differences for the time derivatives to prepare for the later adaptive time stepping. An example of the time difference changing with each time step is plotted in Figure 2.6. The increase and decrease of dt implied that the speed of the change of the temperature/flow/particle profiles was not steady. And the change happened fast at the late stage of evaporation when θ was small.

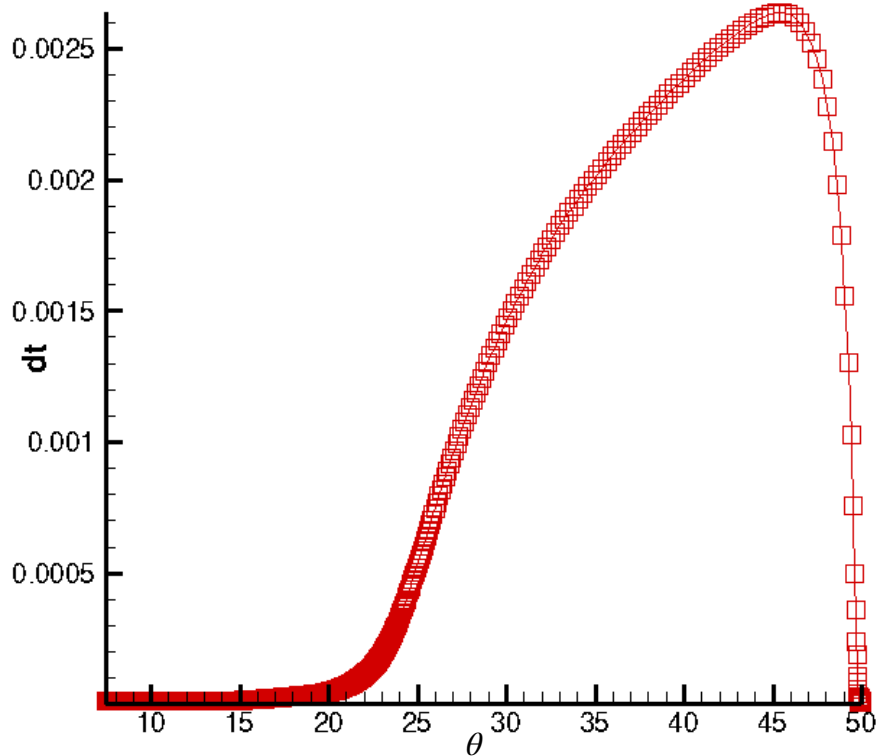


Figure 2.6. The time intervals of each time step dt changing in simulations according to the change rate of the solved variables. CA θ decreases from the right to the left during simulations. Small dt implies a rapid change of flow, temperature or concentration profiles at that θ .

Table 2.4.
Convergence Information

Contact angle (°)	Step	Residual error	Solution error
49.98	1	3.3×10^{-2}	3.9×10^{-1}
	2	9.9×10^{-8}	1.7×10^{-4}
	3	3.6×10^{-10}	3.9×10^{-9}
29.97	1	1.4×10^{-1}	1.1×10^{-1}
	2	4.7×10^{-7}	7.1×10^{-5}
	3	1.2×10^{-9}	5.1×10^{-8}
10.03	1	1.1×10^{-3}	5.5×10^{-2}
	2	1.0×10^{-8}	1.1×10^{-6}
3.37	1	2.0×10^{-3}	5.4×10^{-2}
	2	2.9×10^{-7}	9.8×10^{-6}

After the discretization, the resulting non-linear algebraic equations were transformed into linear algebraic equations using the Newton-Raphson method. A quadratic convergence was reached (because of the Newton-Raphson method) from the start of the simulation to the end as shown in Table 2.4. The iterations stopped when both the residual error and the solution error were below 10^{-5} . This usually took 3-4 iterations. It was hard for the errors to go below 10^{-9} because of the numerical precision, but it was not worth it to increase the precision since the convergence was good enough.

For each integration, the linear equations were solved with a frontal algorithm developed by Hood [98]. The solver was parallelized by Anthony to achieve close to 60% speed gains over a serial algorithm [99].

All of the above procedures were implemented with Fortran code.

2.3.1 Mesh Adjustment

The elliptic mesh algorithm developed by Christodoulou and Scriven [100] is employed to adapt to the moving free surface and to manipulate the mesh density. This algorithm has been proved helpful in many free surface problems [101] [102] [103]. Two more variables r and z were added into the model so that the position change of each node is solved together with other PDEs.

The two equations added to solve r and z according to the elliptic mesh algorithm were:

$$\begin{aligned}
 R_{\xi}^i &= \int_0^1 \int_0^1 \left(\sqrt{\frac{\left(\frac{\partial r}{\partial \xi}\right)^2 + \left(\frac{\partial z}{\partial \xi}\right)^2}{\left(\frac{\partial r}{\partial \eta}\right)^2 + \left(\frac{\partial z}{\partial \eta}\right)^2} + \varepsilon_s} \right) \nabla \xi \cdot \nabla \phi^i |Jac| d\xi d\eta - \\
 &\varepsilon_1 \int_0^1 \int_0^1 f(\xi) \ln \left[\left(\frac{\partial r}{\partial \xi}\right)^2 + \left(\frac{\partial z}{\partial \xi}\right)^2 \right] \frac{d\phi^i}{d\xi} d\xi d\eta - \\
 &M_1 \int_0^1 f(\xi) \ln \left[\left(\frac{\partial r}{\partial \xi}\right)^2 + \left(\frac{\partial z}{\partial \xi}\right)^2 \right] \frac{d\phi^i}{d\xi} d\xi = 0,
 \end{aligned} \tag{2.21}$$

$$\begin{aligned}
 R_{\eta}^i &= \int_0^1 \int_0^1 \left(\sqrt{\frac{\left(\frac{\partial r}{\partial \eta}\right)^2 + \left(\frac{\partial z}{\partial \eta}\right)^2}{\left(\frac{\partial r}{\partial \xi}\right)^2 + \left(\frac{\partial z}{\partial \xi}\right)^2} + \varepsilon_s} \right) \nabla \eta \cdot \nabla \phi^i |Jac| d\xi d\eta - \\
 &\varepsilon_2 \int_0^1 \int_0^1 g(\eta) \ln \left[\left(\frac{\partial r}{\partial \eta}\right)^2 + \left(\frac{\partial z}{\partial \eta}\right)^2 \right] \frac{d\phi^i}{d\eta} d\xi d\eta - \\
 &M_2 \int_0^1 g(\eta) \ln \left[\left(\frac{\partial r}{\partial \eta}\right)^2 + \left(\frac{\partial z}{\partial \eta}\right)^2 \right] \frac{d\phi^i}{d\eta} d\eta = 0,
 \end{aligned} \tag{2.22}$$

where

$$Jac = |\mathbf{J}| = \frac{\partial r}{\partial \xi} \frac{\partial z}{\partial \eta} - \frac{\partial r}{\partial \eta} \frac{\partial z}{\partial \xi} \tag{2.23}$$

is the determinant of the Jacobian of the element; η , ξ are isoparametric coordinates and can be referred to [97] in the finite element method formulations; The adjustable parameters that control the element shapes were set as $M_1 = 0$, $M_2 = 0$, $\varepsilon_1 = 1.0$, $\varepsilon_2 = 1.0$ and $\varepsilon_s = 0.1$; $f(\xi)$ and $g(\eta)$ were set to change according to the element locations because they control the element size thus the mesh density. The distribution of $f(\xi)$ and $g(\eta)$ are shown in Figure 2.7.

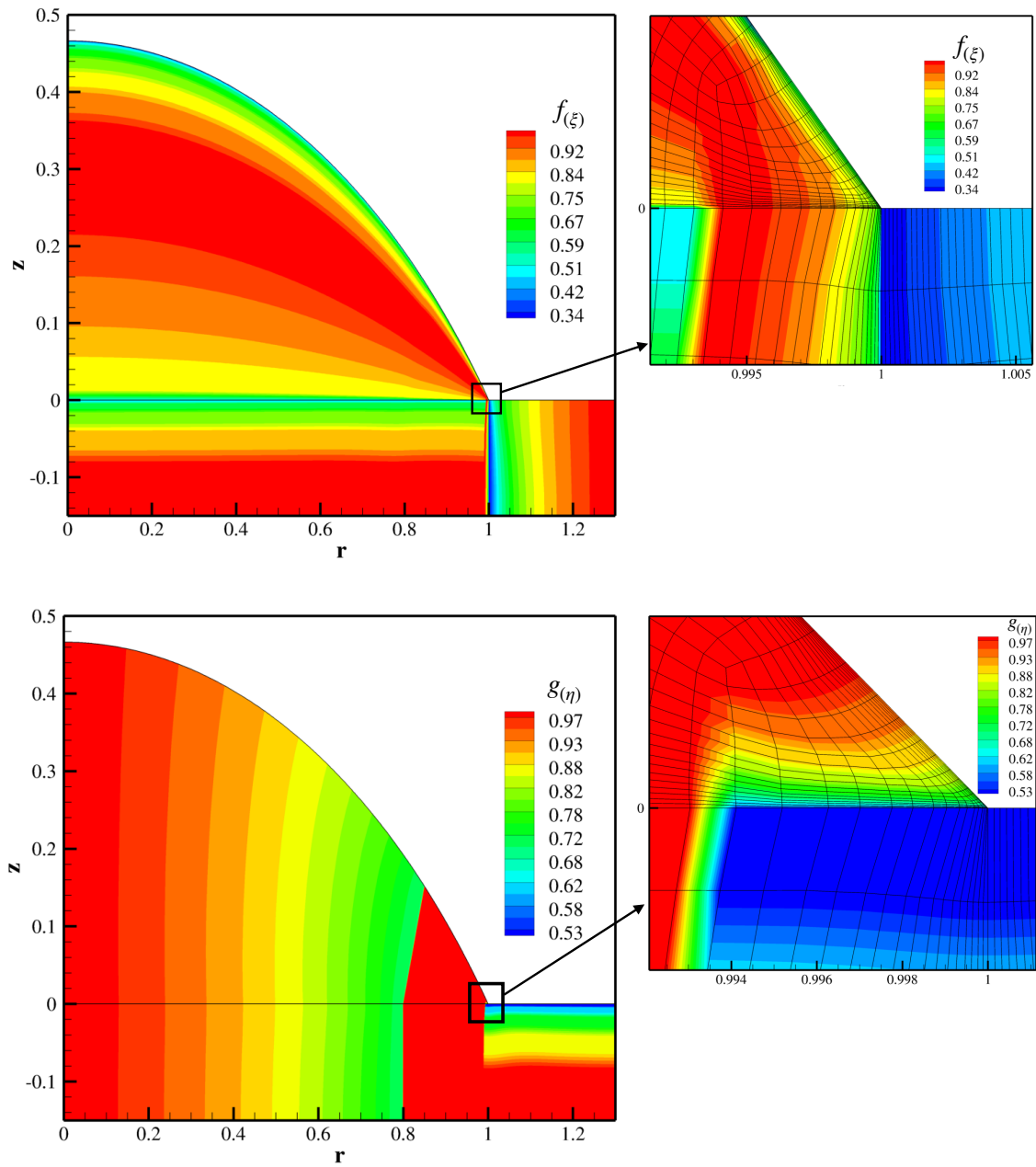


Figure 2.7. The distribution of $f(\xi)$ and $g(\eta)$.

The mesh density near the contact line was set higher than other regions, because the contact line region went through spatially rapid change in terms of velocity, temperature and concentration due to the divergent evaporation flux.

To achieve dense mesh near the contact line, two strategies were implemented. First "algebraic mesh" was set, which was to specify a restriction for a series of nodes. The dashed red line in Figure 2.3 shows the restriction we used, which was defined by

$$z = k_{alge}(r - x_{alge}) \quad (2.24)$$

where $k_{alge} = 3.0$ and $x_{alge} = 0.8$ and transformed into FEM formulation

$$R_{\eta}^i = k_{alge}(r_i - x_{alge}) - z_i \quad (2.25)$$

With this equation, the restricted nodes could only move along the dashed red line. Therefore, the mesh density near the contact line was guaranteed by preventing the elements on the right side of the line from moving to the left. In the rest context of paragraph, the region on the right side of the red dashed line will be called the "restricted region". Then, $f(\xi)$ and $g(\eta)$ of the elements in the restricted region was set as what is shown in Figure 2.7, so that elements tend to gather near the contact line. The mesh near CL is shown by Figure 2.8.

2.3.2 Two-Part FEM Formulations of Boundary Conditions

The imposing of boundary conditions at the drop surface and the drop base is unique in this work, so the formulations are listed below. The notation " $_{SI}$ " means the surface integral.

The continuous heat flux at the drop base (equation 2.16) contains variables in different domains: T in the drop domain and T_s in the substrate domain. Therefore, it is inevitable to use a two-part surface integral formulation: surface integrals were calculated from the adjacent two elements. As shown in Figure 2.9, Element I in the drop domain gives the terms contain T in the surface integral, while Element II in the substrate domain gives the

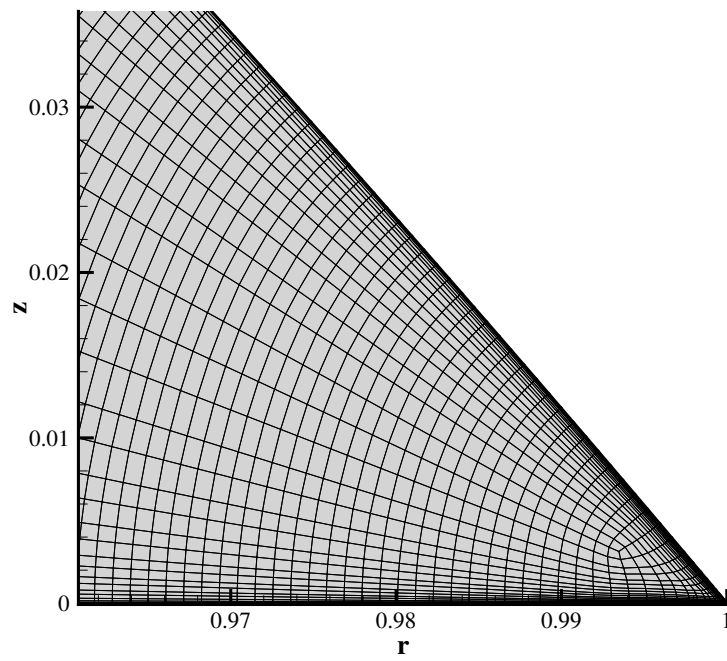


Figure 2.8. The mesh near CL

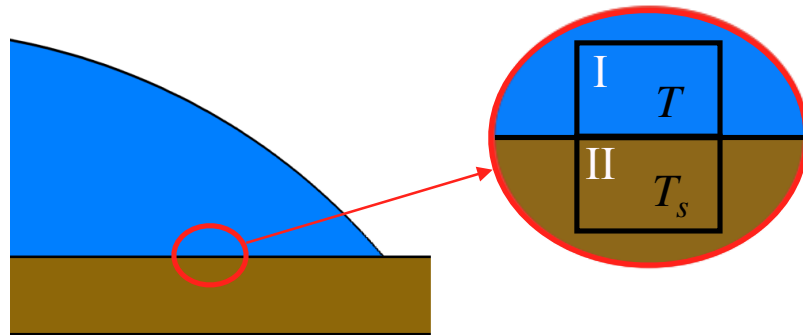


Figure 2.9. Two-part surface integral formulation: Element I in the drop domain gives the terms contain T in the surface integral, while Element II in the substrate domain gives the terms of T_s .

terms of T_s . Then volume integrals were not included at the nodes located at the drop base. The FEM formulation of this boundary condition was divided into two parts, shown below:

$$\begin{aligned}
R_{t,SI}^i &= \int_{\partial\Omega} \phi^i \mathbf{n} \cdot \left(\nabla T - \frac{1}{k_R} \nabla T \right) r ds \\
&= \int_{\partial\Omega} \phi^i \mathbf{n} \cdot \nabla T r ds - \frac{1}{k_R} \int_{\partial\Omega} \phi^i \mathbf{n} \cdot \nabla T r ds \\
&= R_{t,drop}^i - R_{t,substrate}^i = 0.
\end{aligned} \tag{2.26}$$

For each element,

$$\mathbf{n} \cdot \nabla T = \frac{1}{Jac} (r_\eta^2 + z_\eta^2)^{-1/2} [-T_\xi (r_\eta^2 + z_\eta^2) + T_\eta (r_\xi r_\eta + z_\xi z_\eta)], \tag{2.27}$$

$$\mathbf{n} \cdot \nabla T_s = \frac{1}{Jac} (r_\eta^2 + z_\eta^2)^{-1/2} \left[-\frac{\partial T_s}{\partial \xi} (r_\eta^2 + z_\eta^2) + \frac{\partial T_s}{\partial \eta} (r_\xi r_\eta + z_\xi z_\eta) \right]. \tag{2.28}$$

Then,

$$R_{t,drop}^i = \int_0^1 \phi^i [-T_\xi (r_\eta^2 + z_\eta^2) + T_\eta (r_\xi r_\eta + z_\xi z_\eta)] \frac{r}{Jac} d\eta, \tag{2.29}$$

$$R_{t,substrate}^i = \frac{1}{k_R} \int_0^1 \phi^i \left[-\frac{\partial T_s}{\partial \xi} (r_\eta^2 + z_\eta^2) + \frac{\partial T_s}{\partial \eta} (r_\xi r_\eta + z_\xi z_\eta) \right] \frac{r}{Jac} d\eta. \tag{2.30}$$

At the drop surface, the boundary conditions of mass balance, heat balance and mass balance of particles were also imposed by the two-part formulation. There could have been a simpler way of adding surface integrals to volume integrals of the governing equations. However, in the future, it may be necessary to add an additional air domain and compute the evaporation flux from vapor concentrations. Then the boundary conditions will include the variables from both the drop domain and the air domain. The two-part formulations make our code flexible to adapt to the additional air domain.

For the kinematic boundary conditions in (2.8), the finite element method formulation is derived as follows:

$$\begin{aligned}
R_{\xi,SI}^i &= \int_{\partial\Omega} \phi^i [\mathbf{n} \cdot (\mathbf{v} - \mathbf{v}_s) + J] r ds \\
&= \int_{\partial\Omega} \phi^i \mathbf{n} \cdot (\mathbf{v} - \mathbf{v}_s) r d\eta + \int_{\partial\Omega} \phi^i J r ds \\
&= R_{\xi 1} + R_{\xi 2} = 0.
\end{aligned} \tag{2.31}$$

For each element, $ds = \sqrt{r_\eta^2 + z_\eta^2} d\eta$, and the normal unit vector for the drop surface as the one shown in Figure 2.2 is

$$\mathbf{n} = \frac{(-z_\eta, r_\eta)}{\sqrt{r_\eta^2 + z_\eta^2}}. \quad (2.32)$$

Therefore, further,

$$R_{\xi 1}^i = \int_0^1 \phi^i [-z_\eta (u - \dot{r}) + r_\eta (v - \dot{z})] r d\eta, \quad (2.33)$$

$$R_{\xi 2}^i = \int_0^1 \phi^i J r (r_\eta^2 + z_\eta^2)^{1/2} d\eta. \quad (2.34)$$

(Notice: J is a function of r . When taking r -derivative of the formulation, the following equation is needed: $\frac{dJ}{dr} = 2J_0\lambda (1 - r^2)^{\lambda-1} r$.)

The heat balance (2.13) is formulated below:

$$\begin{aligned} R_{t-SI}^i &= \int_{\partial\Omega} \phi^i (REH \cdot \mathbf{J} - \mathbf{n} \cdot \nabla T) r ds \\ &= \int_{\partial\Omega} \phi^i REH \cdot \mathbf{J} r ds - \int_{\partial\Omega} \phi^i \mathbf{n} \cdot \nabla T r ds \\ &= R_{t2}^i - R_{t1}^i = 0. \end{aligned} \quad (2.35)$$

For each element, $\mathbf{n} \cdot \nabla T = \frac{1}{Jac} (r_\eta^2 + z_\eta^2)^{-1/2} [-T_\xi (r_\eta^2 + z_\eta^2) + T_\eta (r_\xi r_\eta + z_\xi z_\eta)]$. Therefore,

$$R_{t1}^i = \int_0^1 \phi^i [-T_\xi (r_\eta^2 + z_\eta^2) + T_\eta (r_\xi r_\eta + z_\xi z_\eta)] \frac{r}{Jac} d\eta, \quad (2.36)$$

$$R_{t2}^i = REH \cdot \int_0^1 \phi^i J r (r_\eta^2 + z_\eta^2)^{1/2} d\eta = REH \cdot R_{\xi 2}^i. \quad (2.37)$$

The mass balance of particles (2.14) are formulated as such:

$$\begin{aligned} R_{m-SI}^i &= \int_{\partial\Omega} \phi^i (Pe_p \cdot \mathbf{J} c_p + \mathbf{n} \cdot \nabla c_p) r ds \\ &= \int_{\partial\Omega} \phi^i Pe_p \cdot \mathbf{J} c_p r ds + \int_{\partial\Omega} \phi^i \mathbf{n} \cdot \nabla c_p r ds \\ &= R_{m2}^i + R_{m1}^i = 0. \end{aligned} \quad (2.38)$$

For each element, $\mathbf{n} \cdot \nabla c_p = \frac{1}{Jac} (r\eta^2 + z\eta^2)^{-1/2} \left[-\frac{\partial c_p}{\partial \xi} (r\eta^2 + z\eta^2) + \frac{\partial c_p}{\partial \eta} (r_\xi r_\eta + z_\xi z_\eta) \right]$.

Therefore,

$$R_{m1}^i = \int_0^1 \phi^i \left[-\frac{\partial c_p}{\partial \xi} (r\eta^2 + z\eta^2) + \frac{\partial c_p}{\partial \eta} (r_\xi r_\eta + z_\xi z_\eta) \right] \frac{r}{Jac} d\eta, \quad (2.39)$$

$$R_{m2}^i = Pe_p \cdot \int_0^1 \phi^i Jc_p r (r\eta^2 + z\eta^2)^{1/2} d\eta. \quad (2.40)$$

3. RESULTS

3.1 Drop Surface Temperature

3.1.1 Effect of Heat Convection

Both heat convection and diffusion influence the surface temperature, although many studies neglected heat convection [46, 71, 73]. In our research, two simulations were done: one using heat convection-diffusion equation, the other including only heat diffusion. As shown in figure 3.1, the numerical solution of the two simulations showed the effect of heat convection on the drop surface temperature profile as contact angle θ changes. When $\theta > 15^\circ$, the surface temperature is significantly different with or without heat convection. However, the Peclet number which is the ratio of heat convection to diffusion is small: $Pe = \frac{v_c l_c}{\alpha} \sim 10^{-2}$. The contradiction implied that Pe did not represent the relation between heat convection and diffusion well enough.

The importance of heat convection was enhanced by the Marangoni flow. Two more simulations were done with Marangoni flow being ruled out, i.e. the Marangoni stress term was set to 0 in BC of (2.10). Similarly, one simulation included heat convection and the other did not. The surface temperature comparison was shown in Figure 3.2. Since the results with convection and without convection are almost same, heat convection is negligible. Hence, the small Pe describes the cases with no Marangoni flow accurately.

The reason why Pe did not represent the results with Marangoni flow was the use of inappropriate scales. The velocity scale used for Pe was $v_c (= \frac{Dc_c}{\rho l_c})$, which is essentially the characteristic velocity of the capillary flow. Marangoni flow significantly increases fluid velocity, compared to the situation with pure capillary flow. Figure 3.3 shows the magnitude of the dimensionless axial velocity $v = \tilde{v}/v_c$ (with \tilde{v} representing the dimensional axial velocity) from numerical results when Marangoni flow was included. when Marangoni flow exists, numerical solution of Navier-Stokes equation showed that the dimensionless

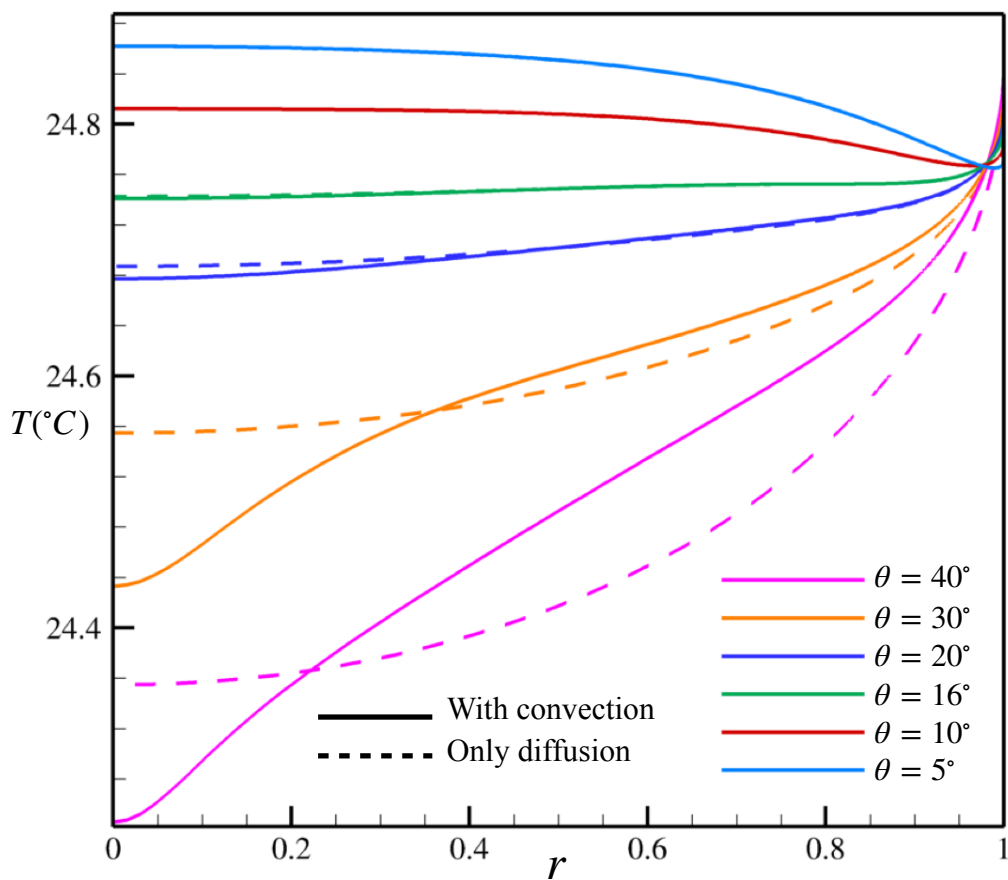


Figure 3.1. Surface temperature under various θ changing as evaporation. The influence of heat convection was shown by the comparison of the dashed lines (no convection) and the solid lines (convection included). Heat convection is negligible when $\theta < 15^\circ$.

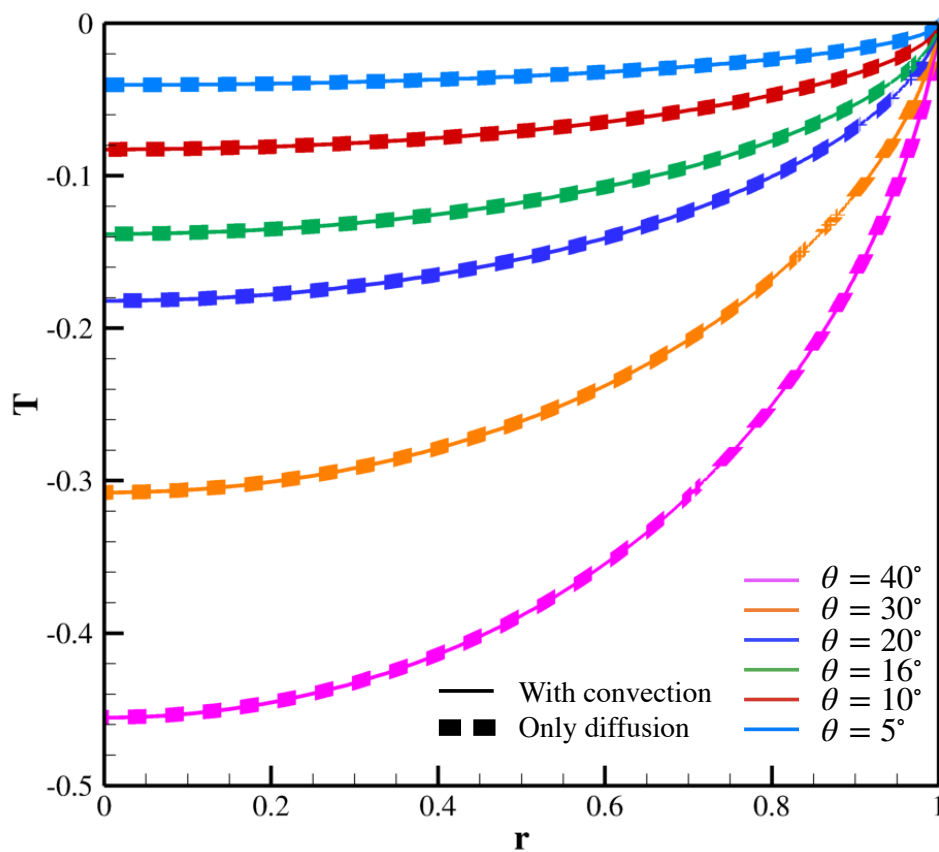


Figure 3.2. Surface temperature when no Marangoni flow was included. The overlap of the results with or without heat convection illustrates that heat convection was negligible.

axial velocity $v = \tilde{v}/v_c$ (with \tilde{v} representing the dimensional axial velocity) was as large as 10^3 . This means that the Marangoni velocity was 10^3 times the characteristic velocity v_c .

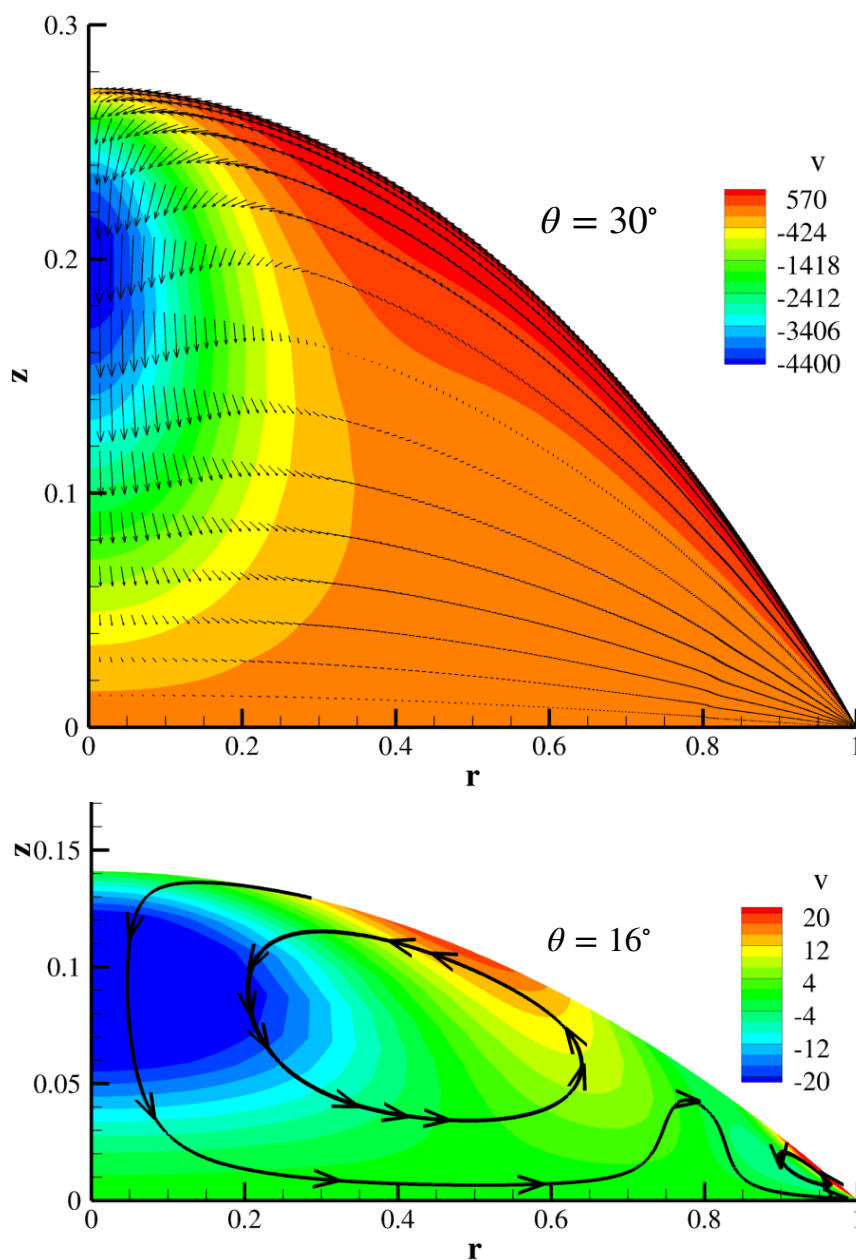


Figure 3.3. The magnitude of the dimensionless axial velocity $v = \tilde{v}/v_c$ from numerical results when Marangoni flow was included. v_c is the scale of the capillary flow. $|v|$ can be as large as 10^3 , meaning the Marangoni flow was much stronger than the capillary flow. The magnitude decreased with evaporation as the contact angle decreased.

Thus, a new dimensionless group, Pe_{Ma} which uses proper scales, needs to be defined to compare heat convection and diffusion when Marangoni flow exists. The scale of Marangoni flow can be calculated as follows. The radial Marangoni velocity u_{Ma} was derived from a balance of the Marangoni stress and the viscous stress (figure 3.4) as in (3.1); and the axial Marangoni velocity v_{Ma} was defined in (3.2) based on incompressibility.

$$\beta \frac{T_c}{R} \sim \mu \frac{u_{Ma}}{H} \quad (3.1)$$

$$\frac{v_{Ma}}{H} \sim \frac{u_{Ma}}{R} \quad (3.2)$$

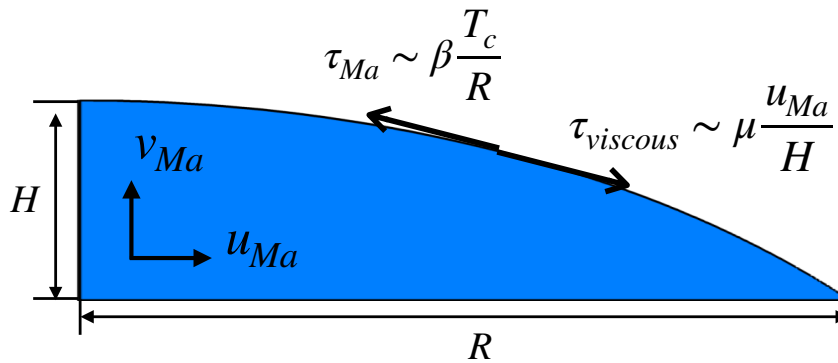


Figure 3.4. The balance of the Marangoni stress and the viscous stress.

Besides, the length scale in Pe_{Ma} was the drop thickness instead of $l_c = R$, the radius of the drop base, due to the following reason. Temperature changes faster between the drop surface and the drop base than that of the radial direction (figure 3.5), leading to more significant heat transport in the axial direction. Hence, the length scale should be H , the thickness of the drop. Because of the same reason, the velocity scale should be the axial Marangoni velocity v_{Ma} instead of the radial Marangoni velocity u_{Ma} .

So the new dimensionless number is $Pe_{Ma} = \frac{v_{Ma}H}{\alpha}$. With 3.1 and 3.2 substituted in for v_{Ma} , it scales as

$$Pe_{Ma} \sim \frac{\beta T_c R}{\mu \alpha} \cdot \left(\frac{H}{R}\right)^3 \sim 10^4 \left(\frac{H}{R}\right)^3, \quad (3.3)$$

whose value depends on the aspect ratio H/R , which decreases during evaporation. In this case, when $H/R > 0.1$, $Pe_{Ma} > 10$. So $H/R > 0.1$ is the condition when heat convection

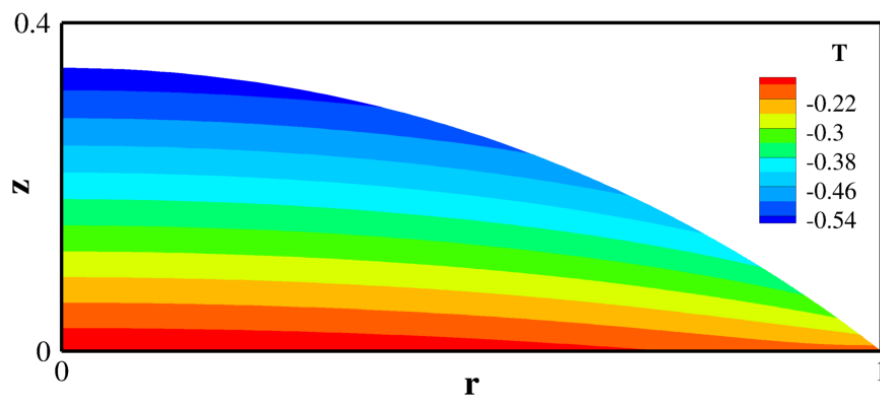


Figure 3.5. Temperature profile in the drop when $\theta = 38^\circ$. Temperature changes faster in the axial direction than in the radial direction.

is important. The dependence of the aspect ratio on θ was derived from geometry of a spherical cap as (3.4), and was shown by figure 3.6.

$$H/R = (1 - \cos\theta) / \sin\theta \quad (3.4)$$

When $\theta > 15^\circ$, $H/R > 0.1$. This is when heat convection should make a difference. Validated by figure 3.1, surface temperatures with and without heat convection are obviously different for $\theta > 15^\circ$. At late evaporation stage when $\theta < 10^\circ$, $H/R < 0.1$. This is when heat convection can be neglected. It again was supported by figure 3.1 that surface temperatures were almost the same with and without heat convection. Therefore, heat convection plays an important role in determining the surface temperature distribution when the contact angle is large ($\theta > 15^\circ$ for a water drop with $R = 1\text{mm}$), and can be neglected only at the late stage of evaporation.

3.1.2 Extremum Points

The change of surface temperature with radial position is not monotonous when the drop is flat (at a small contact angle) as shown in figure 3.1. Extrema of temperature exist when the temperature was observed from the drop top to the contact line along the drop surface. The extrema are expressed by $dT/ds = 0$, thus also giving $d\sigma/ds = 0$. The sign of $d\sigma/ds = 0$ is opposite on either side of an extremum (figure 3.7). Marangoni stress $\tau_{Ma} = \frac{\sigma_c}{l_c} \nabla_s \sigma$ is in the same direction as s (called outward in the following context) if $d\sigma/ds > 0$, and inward if $d\sigma/ds < 0$. Since $d\sigma/ds$ is negatively correlated to dT/ds , Marangoni stress is outward when $dT/ds > 0$, and inward when $dT/ds < 0$.

The location of the extrema under different θ are shown in figure 3.8. θ represents the evaporation process, and r indicates the location at a certain θ . As evaporation, θ decreases and the results in the Figure 3.8 change from the right (Region A) to the left (Region C). At the start of evaporation, surface temperature was monotonous with no extrema (Region A). As the contact angle θ decreased near Region B during evaporation, an extremum emerged. Then one extremum bifurcated into two extrema at different locations r for a certain θ in region B. $d\sigma/ds < 0$ between the two extrema. Later as θ decreases to region C, one

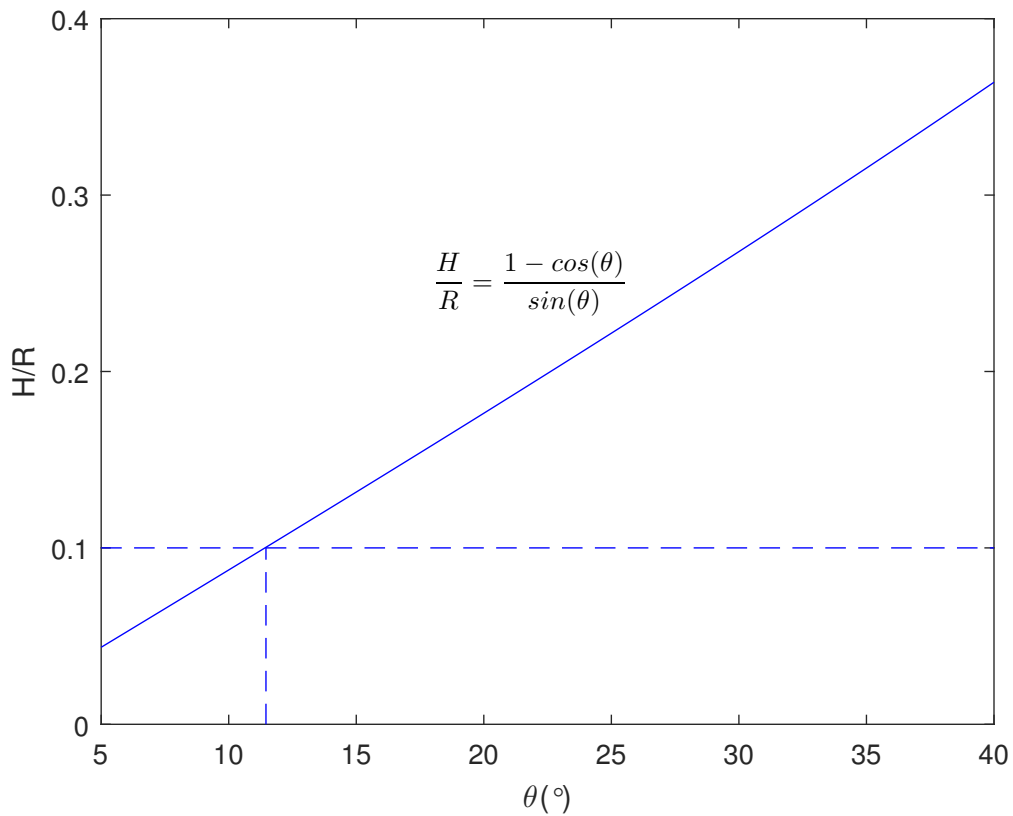


Figure 3.6. The dependence of the aspect ratio on θ

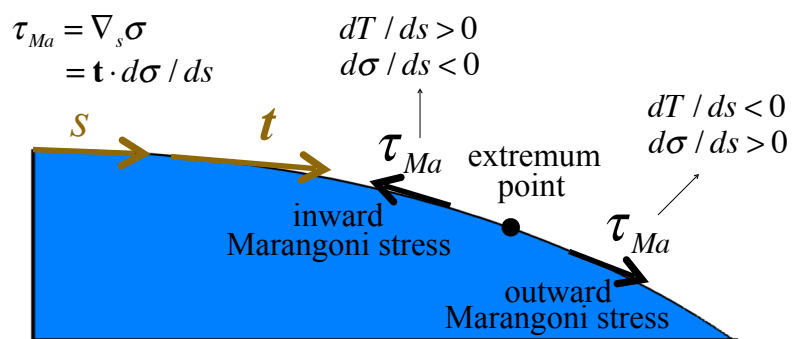


Figure 3.7. The direction of Marangoni stress

extremum moved to $r = 0$ and does not count, so only the other extremum still existed. Given a pair of (θ, r) , $d\sigma/ds > 0$ if it is on the right of the extremum line, and $d\sigma/ds < 0$ if on the left.

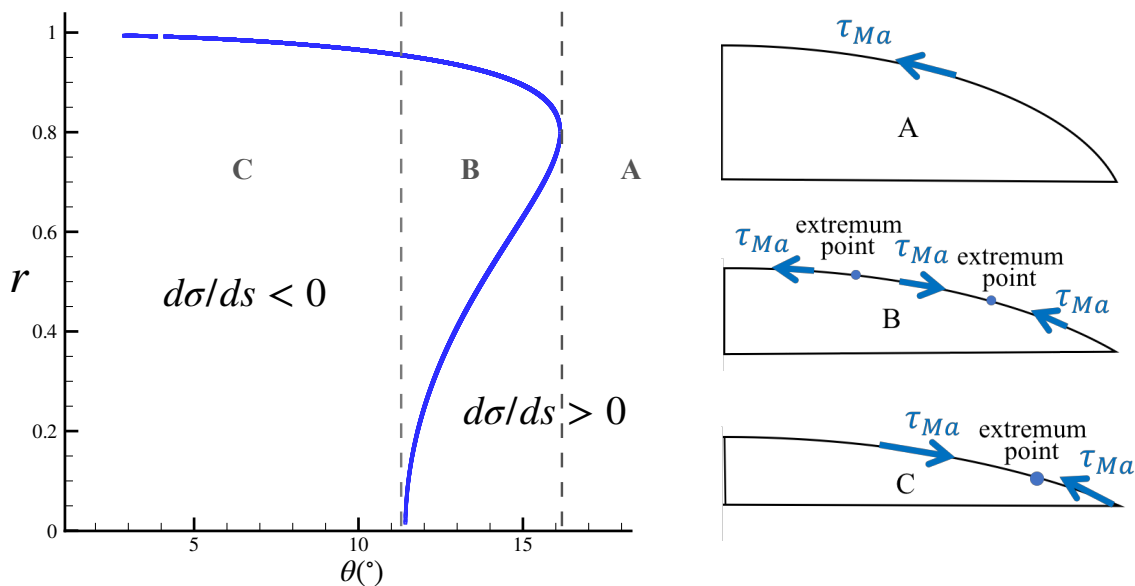


Figure 3.8. Locations of extremum points ($d\sigma/ds = 0$). As drop evaporates, θ decreases from the right to the left on the abscissa axis. Given a pair of (θ, r) , $d\sigma/ds > 0$ if it is on the right of the extremum line, and $d\sigma/ds < 0$ if on the left.

3.1.3 The Effect of Substrate Dimensions On Temperature

The substrate dimensions affect the temperature distribution in drop [73]. Figure 3.8 is the result using the same substrate dimensions (shown in table 2.1) as Hu and Larson's work [46]. The transition of temperature gradient from positive to negative happened around $\theta = 14^\circ$, which agreed with their work. But to be more accurate, the transition happens in a range of θ when the sign of the temperature gradient changes across the drop surface.

There is a sharp increase of surface temperature as r goes to 1 in Figure 3, but this sharp increase is not a blow-up as shown in Figure 3.9. The isotherms can be referred to in Figure

3.10. The sharp increase is caused by the abrupt disappearance of evaporative cooling at the substrate-air interface. The disappearance led to higher temperature at the substrate-air interface. Therefore, heat conduction from the right to the left near the CL warmed up the CL region of the drop. If the substrate radius was the same as drop base radius R , viz. $l_s = 1$, then the extremum points locations are shown by Figure 3.11. The disappearance of extremum points near CL implies the lack of the sharp increase near the CL.

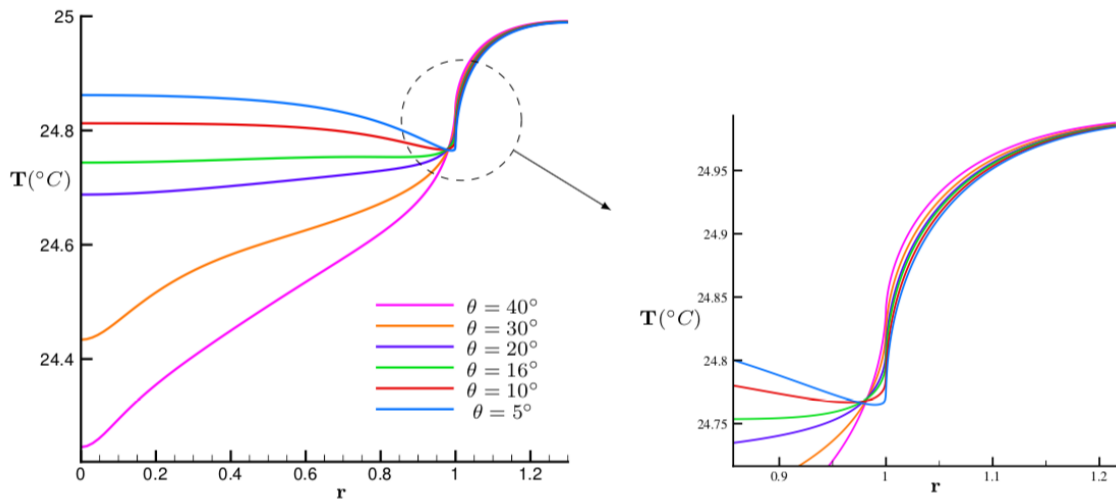


Figure 3.9. The surface temperature of the air-drop interface ($0 \leq r \leq 1$) and the air-substrate interface ($r \geq 1$)

The extension of the length of the substrate does not change the temperature profile in the drop much. Figure 3.12 compares the extremum point locations of the results with substrate length of $l_s = 1.3$ and $l_s = 2.0$. The complete overlap indicates that using $l_s = 1.3$ was enough and further extending the length of the substrate will be no use.

The increase of the thickness of the substrate matters. The emergence of extremum points is different as what Figure 3.13 shows. For a thin substrate ($d = 0.15$), an extremum point first emerged in the middle of the drop, then splitted into two and each moved in the opposite directions. For a thicker substrate ($d = 0.5$), an extremum point emerged from the top of the drop and moved toward CL. The flow profiles lead by these two ways will be

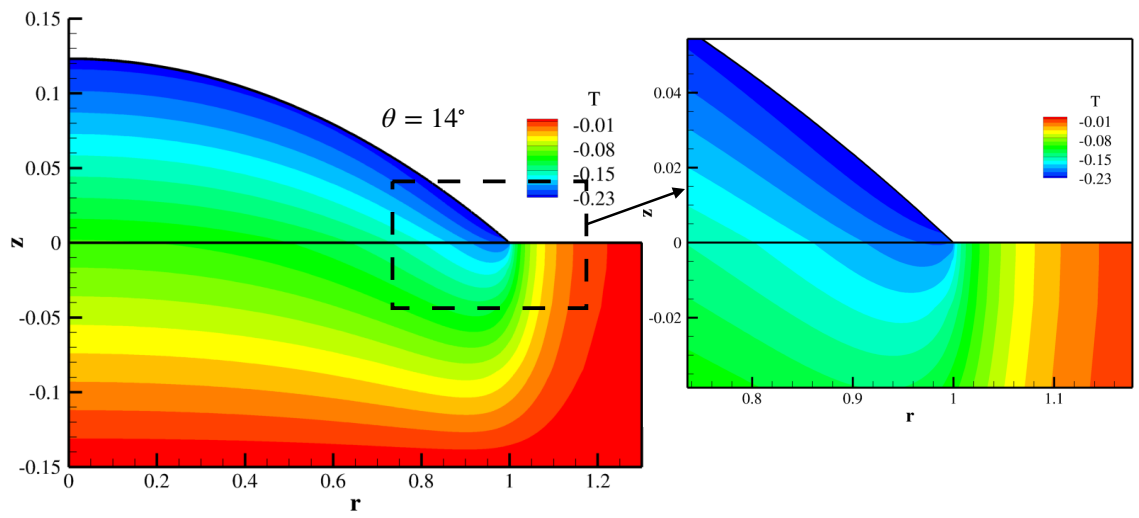


Figure 3.10. The isotherms when $\theta = 14^\circ$ for the whole domain and near the contact line.

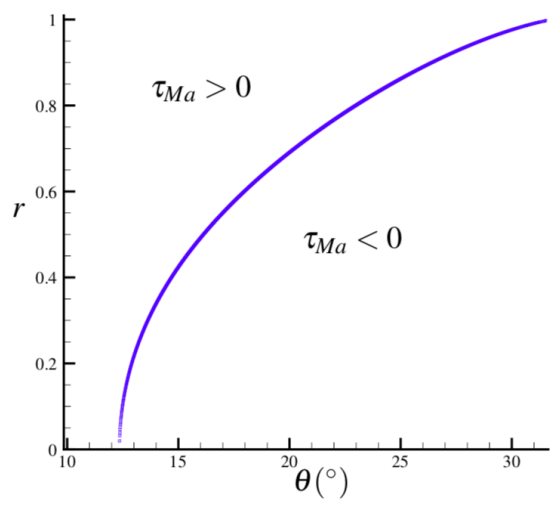


Figure 3.11. Locations of extremum points ($d\sigma/ds = 0$) when the substrate radius was set to be R .

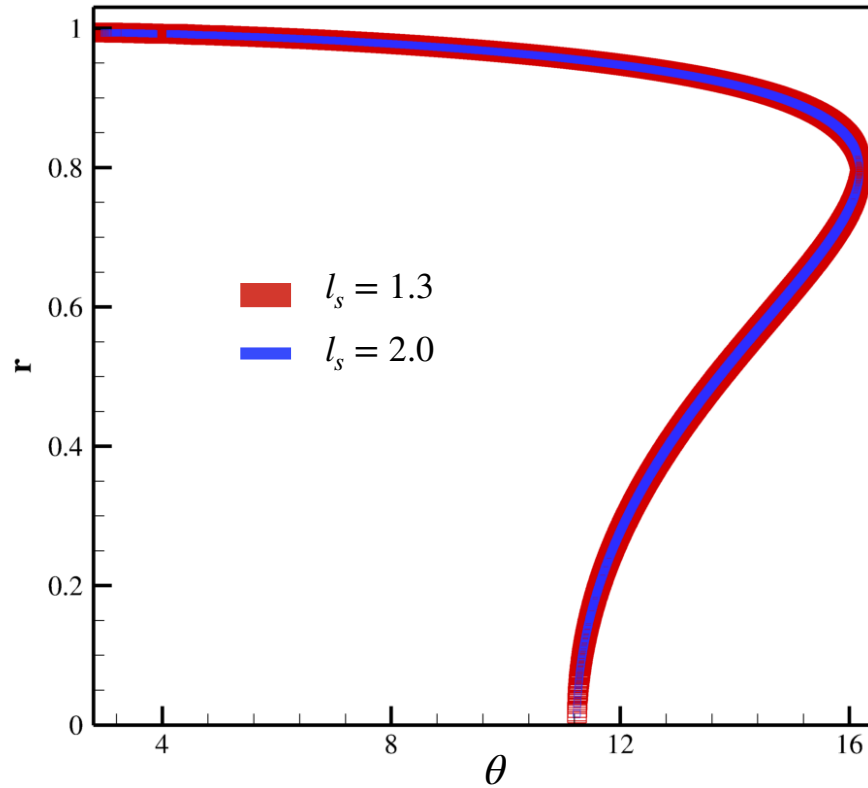


Figure 3.12. The extremum point locations of the results with substrate length of $l_s = 1.3$ and $l_s = 2.0$. The complete overlap indicates that using $l_s = 1.3$ was enough and further extending the length of the substrate in simulations will be no use.

shown in the next sections. The discussion of when the substrate thickness does not change the temperature or the flow profile is in the section on turning points.

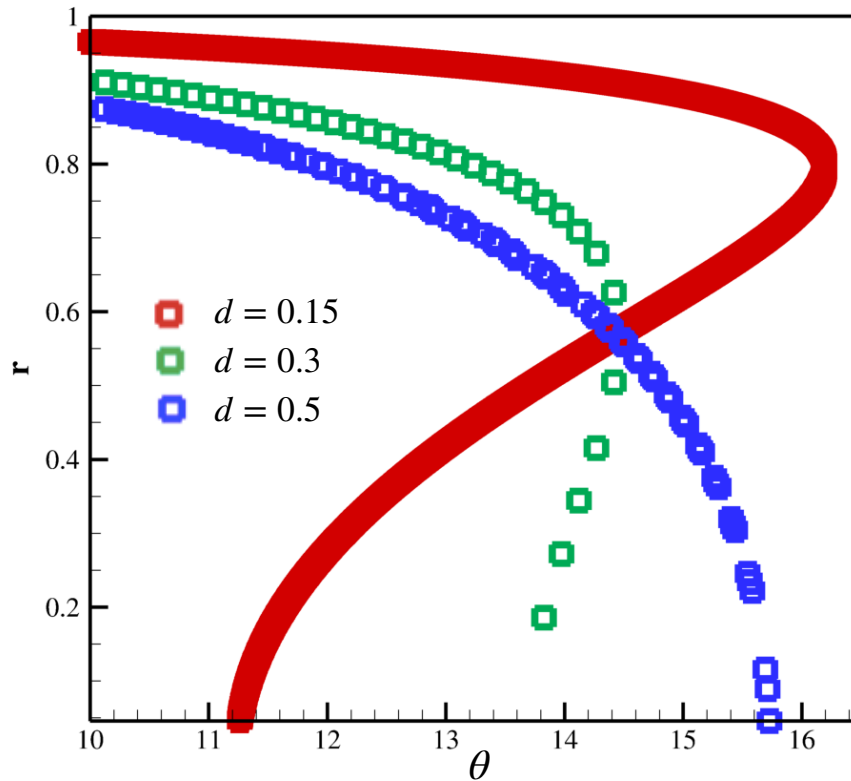


Figure 3.13. The locations r and changes with θ of extremum points for results with various substrate thickness d .

If the substrate was heated, the temperature of the drop, on the average, was higher. However, the flow profile is determined by the temperature gradient instead of the temperature itself. The comparison of the case of the room temperature and the case with a heating substrate, where the base of the substrate was wet to be $\tilde{T} = 40^\circ\text{C}$ ($T = 15$), is shown in Figure 3.14. The gradient of the temperature at the drop surface was almost the same with two cases. Therefore, we only study problems in the non-heating condition as representatives. If a heating problem is to be studied carefully, the heat exchange between the drop and the air and between the substrate and the air cannot be neglected because of the big temperature difference.

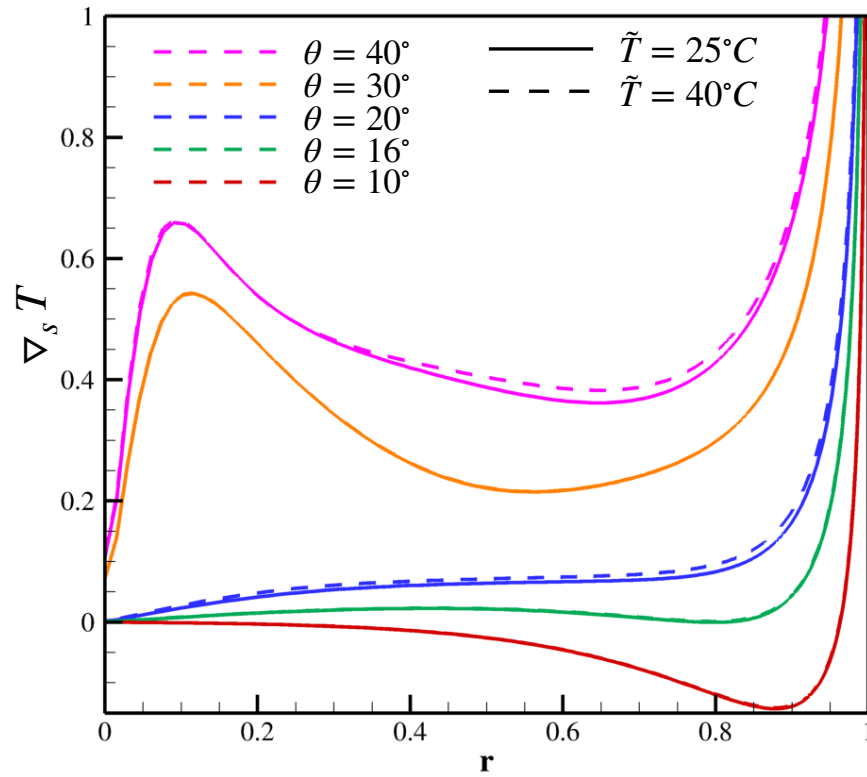


Figure 3.14. The comparison of the results with different substrate temperature at the bottom. The results are the surface temperature gradient at various θ . The temperature was set to be room temperature ($\tilde{T} = 25^\circ\text{C}$) and $\tilde{T} = 40^\circ\text{C}$, which means a slight heating at the bottom. The gradient of the temperature was almost the same with the two cases.

3.2 Multi-Circulation Flow Profiles

3.2.1 Flow Profiles and Stagnation Points

Flow profiles change during drop evaporation. At first with a large contact angle, a perfect single counter-clockwise circulation flow was formed as in figure 3.15. This circulation flow maintained till extremum points emerged on the surface. Then the profile changed to multi-circulation flows (shown with $\theta = 14^\circ$ in figure 3.16). Later, a clockwise circulation flow was developed as is shown in figure 3.17.

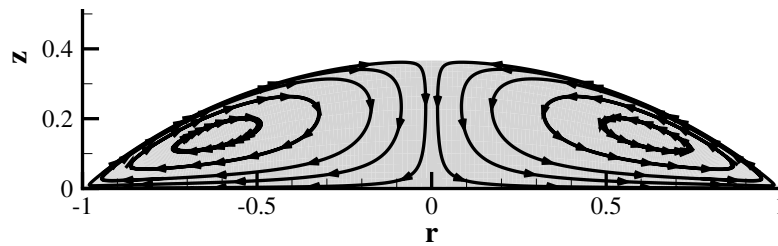


Figure 3.15. A perfect circulation flow was developed when $\theta = 40^\circ$.

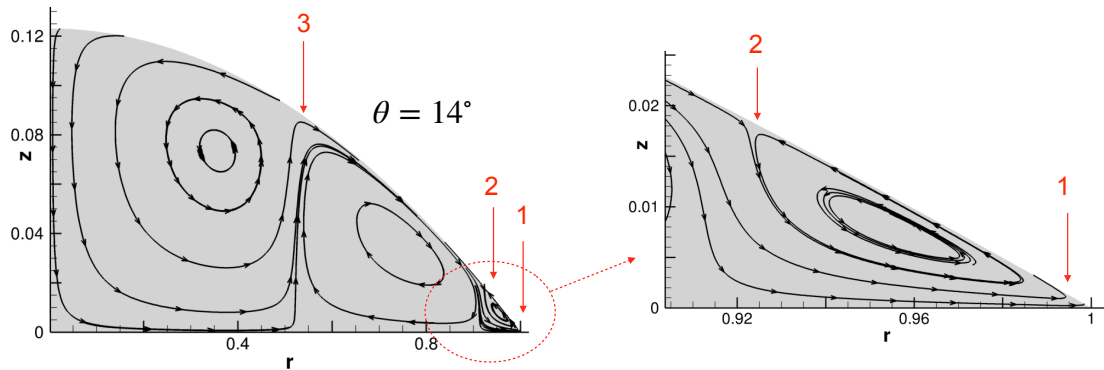


Figure 3.16. Flow profiles of multi-circulation when $\theta = 14^\circ$. Zooming in to CL showed a stagnation point near CL.

Stagnation points, describing the point where surface flow was 0 ($v_s = \mathbf{t} \cdot \mathbf{v} = 0$ with \mathbf{t} as the tangential unit vector shown in figure 3.7), emerged at the later stage of evaporation.

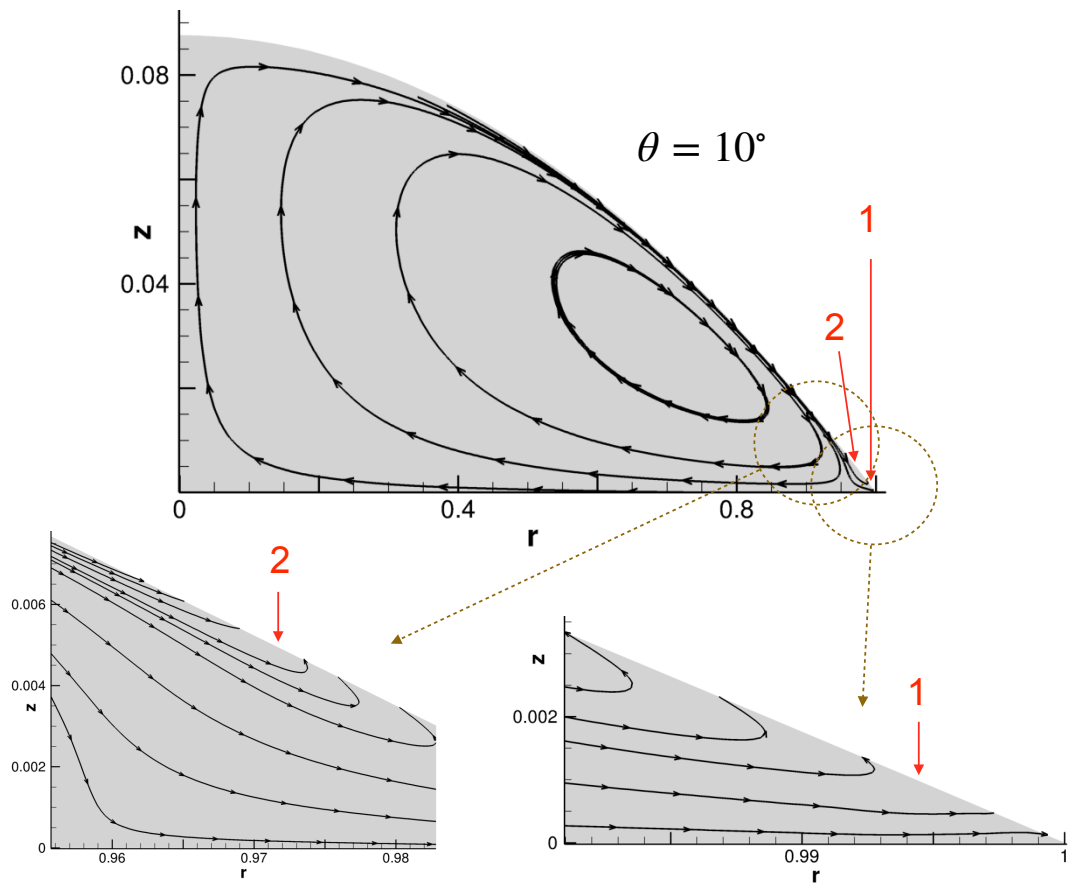


Figure 3.17. Flow profiles of multi-circulation when $\theta = 10^\circ$. Zooming in to CL showed two stagnation points near CL at different locations.

The surface flow is in the opposite directions on the two sides of a stagnation point. It was easy to notice the stagnation point when the flows were multi-circulations as 3.16. It is also worth noticing that zooming in to the CL revealed stagnation points in both Figure 3.16 and Figure 3.17. For example, at $\theta = 10^\circ$, there were two stagnation points near CL.

The locations of the stagnation points were tracked by finding the surface point where $v_s = 0$, and are shown in figure 3.18. When tracking the locations, if a stagnation point locates within 10^{-3} from CL, it is passed. With in such small distance from the CL, the drop surface is as close to the substrate as the scale of molecules, but our model lost precision at the scale of molecules by omitting the disjoining pressure. Similar to figure 3.8 of the extremum points, the surface flow is inward on the right of the line and outward on the left. When $\theta > 20^\circ$, any pair of (r, θ) is on the right of the line, which means the surface flow is inward over the whole drop, implying the counter-clockwise circulation. When $\theta = 14^\circ$, there were three stagnation points. The surface velocity changed direction at each stagnation point. As in figure 3.16, from the drop top to the contact line along the surface, the flow changed from inward to outward and to inward again and to outward again.

The stagnation points at $r < 0.95$ were caused by the change of Marangoni stress direction. The comparison of the extremum points and the stagnation points in figure 3.19 showed that the locations of the two points coincided for the $r < 0.95$ part. These stagnation points are named Marangoni-induced stagnation points, since the extremum points are the points where Marangoni stress changes directions. For example, when $\theta = 15^\circ$, there were two Marangoni-induced stagnation points according to figure 3.19 (the points where red line and blue line coincide). The flow profile near one of the Marangoni-induced stagnation points is shown in figure 3.20(a).

However, some of the stagnation points can not be explained by the direction change of the Marangoni stress. In Figure 3.19 for $r > 0.99$, the two lines do not coincide. These are the stagnation points close to the contact line. For example, when $\theta = 10^\circ$, there were two stagnation points, but only one extremum point. The stagnation point at around $r = 0.95$ coincided with the extremum point, thus was a Marangoni-induced one. And the one at around $r = 0.995$ was an extra stagnation point. The flow field around this stagnation point

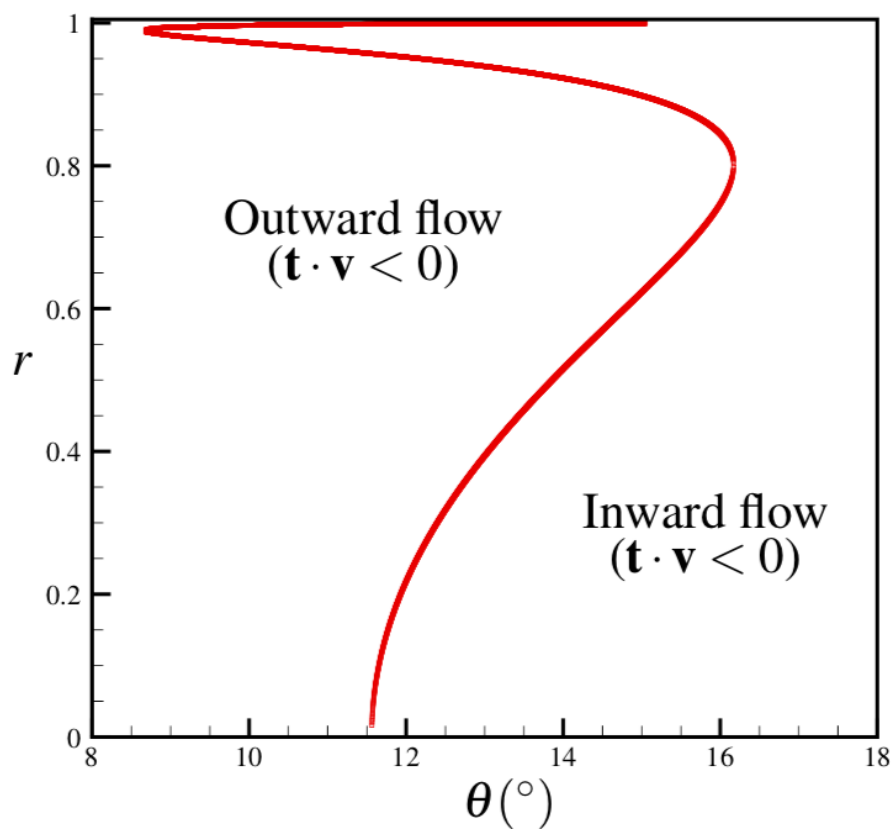


Figure 3.18. The radial locations r of the stagnation points, where the surface flow is 0, as θ decreases with evaporation. The surface flow is inward on the right of the line and outward on the left.

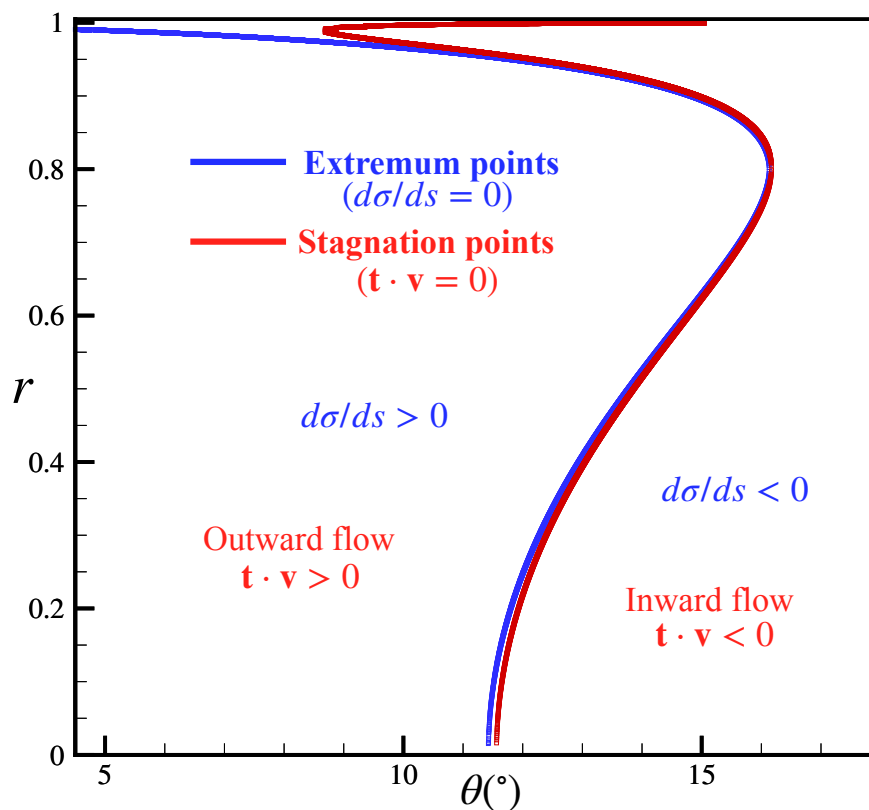
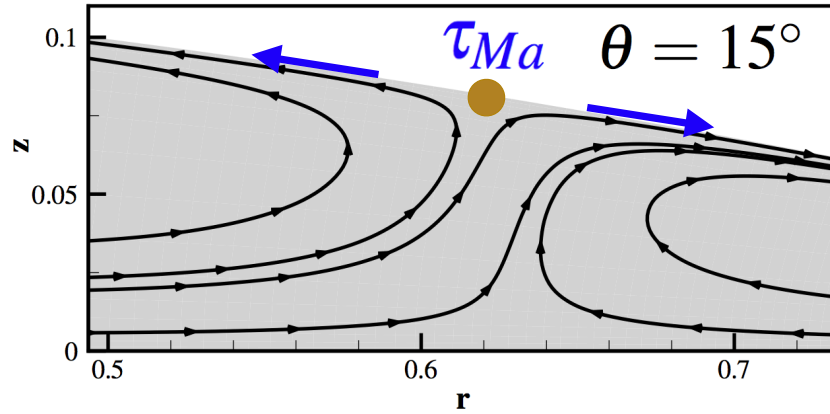
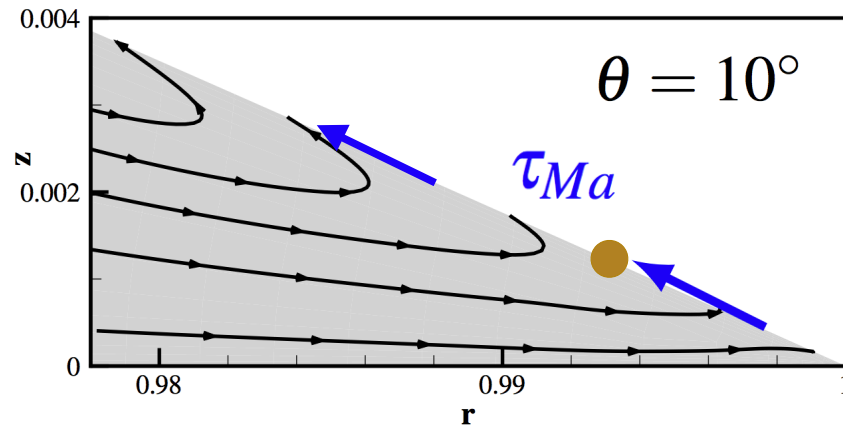


Figure 3.19. Comparison between locations of stagnation points and $\tau_{Ma} = 0$ points. The locations of stagnation points are not exactly where $\tau_{Ma} = 0$ due to capillary flow. The stagnation points close to $r = 1$ emerge much earlier than extremum points during evaporation.

are shown by figure 3.20(b). Such a stagnation point was also observed experimentally by Xu [65], which existed less than $17\mu\text{m}$ away from the contact line, giving $r > 0.992$ (in a dimensionless form) for an evaporating water drop with a 10° contact angle.



(a) A Marangoni stagnation point: Marangoni stresses are in the opposite directions on the two side of the stagnation point.



(b) A capillary stagnation point (r, z not to scale): Marangoni stresses are in the same direction on the two side of the stagnation point.

Figure 3.20. Flow profiles and Marangoni stresses near the two kinds of stagnation points.

3.2.2 Capillary-Induced Stagnation Point

No extremum point exists near the stagnation point, meaning the Marangoni stress is in the same direction around the stagnation point.

The stagnation points at $r > 0.99$ are caused by divergence of capillary flow near the contact line. To study the influence of the divergence on stagnation points, a different boundary condition was used to eliminate the divergence. Widjaja [104] found that radial velocities were much less with a constant evaporation flux imposed on the drop-gas interface when studying capillary flow with no Marangoni stress incorporated. Thus, we imposed a uniform evaporation flux similar to Widjaja's work but incorporated Marangoni stress, and found that the surface flow was inward with no stagnation point near the contact line at $\theta = 10^\circ$ (figure 3.21). The comparison of the locations between the stagnation points and the extremum points is as Figure 3.22 with the uniform flux condition. The locations overlapped for all of the points and no extra stagnation points emerged. Therefore, only if the capillary flow velocity increases rapidly (caused by the divergent evaporation flux) near the contact line does the extra stagnation point exist. So it is named a capillary-induced stagnation point.

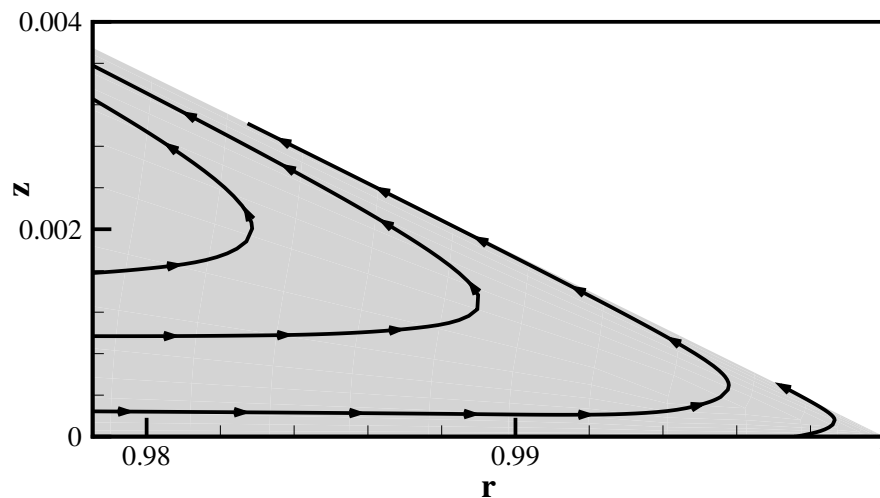


Figure 3.21. Flow profile near the contact line with $\theta = 10^\circ$ with a constant evaporation flux imposed. No capillary-induced stagnation point emerged.

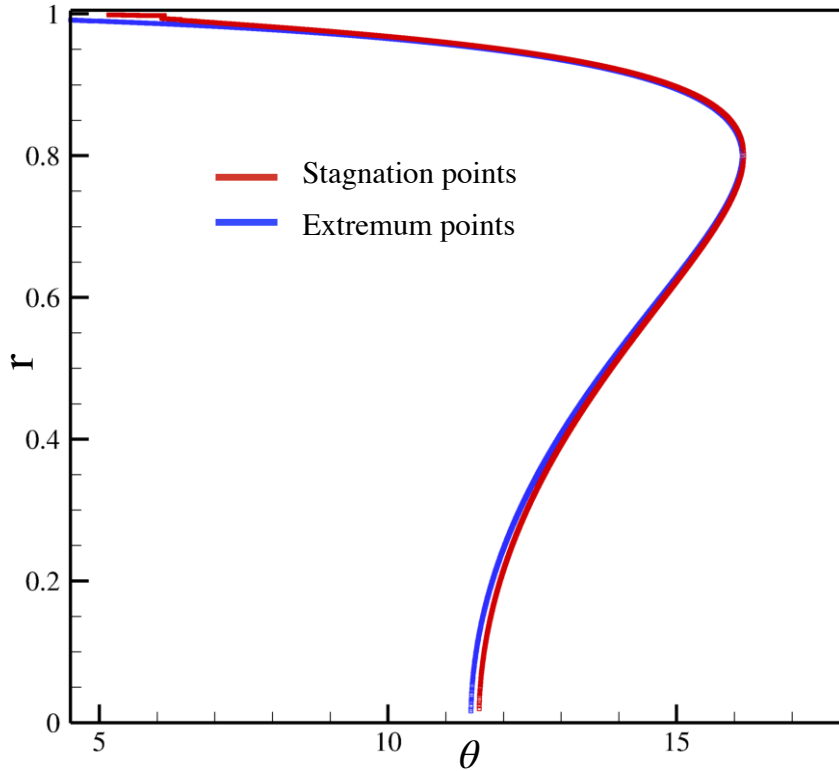


Figure 3.22. The comparison of the locations between the stagnation points and the extremum points with the uniform flux condition. The locations overlapped for all of the points and no extra stagnation points emerged.

The essence of the capillary-induced stagnation point is that the surface velocity is in opposite direction to Marangoni stress between the stagnation point and the contact line (figure 3.20(b)). This was explained by lubrication theory near the contact line (figure 3.23). Lubrication theory can be used because the contact angle was small ($\theta < 15^\circ$) when stagnation points emerged near the contact line. The height-averaged radial velocity for capillary flow was derived from mass balance as equation (3.5) [62], where $A(\theta)$ is a coefficient that changes as the drop evaporates. The mass balance keeps the same with or without Marangoni stress; therefore, the height-averaged radial velocity $\bar{u}_{r(r,\theta)}$ is essentially the same as (3.5) when Marangoni flow exists.

$$\bar{u}_{r(r,\theta)} = A(\theta) \frac{1}{r} \left[(1-r^2)^{-\lambda(\theta)} - (1-r^2) \right] \quad (3.5)$$

The radial velocity profile at each value of r is parabolic in z as $u_r(r,\theta) = Az^2 + Bz + C$ from lubrication theory. The following boundary conditions (dimensionless form) were applied: $v_r|_{z=0} = 0$ and $\frac{\partial v_r}{\partial z}|_{z=h(r,t)} = \tau_{Ma}$ with τ_{Ma} as the Marangoni stress in s direction. The surface velocity in s direction v_s derived from these conditions is

$$v_s = v_r|_{z=h(r,t)} = \frac{3}{2}\bar{u}_r(r,\theta) + \frac{1}{4}\tau_{Ma}h(r,t). \quad (3.6)$$

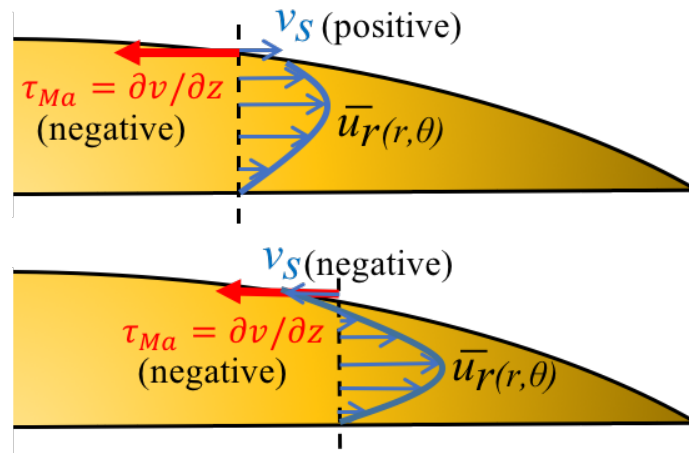


Figure 3.23. Lubrication theory: When τ_{Ma} is negative, v_s can be positive or negative based on the value of $\bar{u}_r(r,\theta)$

From (3.5), $\lim_{r \rightarrow 1} \bar{u}_r(r,\theta) = \infty$ with the physical divergent evaporation flux condition; and $\tau_{Ma}h(r,t)$ is bounded. Therefore $\lim_{r \rightarrow 1} v_s > 0$ for whichever value of τ_{Ma} . That is to say, the surface flow near the contact line is toward the contact line even when τ_{Ma} is negative (away from the contact line). It clearly didn't happen for a constant evaporation flux condition as the numerical results in figure 3.21, because $\bar{u}_r(r,\theta)$ was bounded in (3.6) under this condition.

3.2.3 Offset of Marangoni-Induced Stagnation Points

The phenomenon that the surface flow is in the opposite direction to Marangoni stress does not only happen where capillary flow velocity diverges (between capillary-induced stagnation points and contact lines), but also where Marangoni stress is small (close to ex-

tremum points). It is demonstrated by the offset of the line of Marangoni-induced stagnation points from the line of extremum points. In figure 3.24, between the two lines are the conditions when $d\sigma/ds > 0$ yet surface flow is outward ($\mathbf{t} \cdot \mathbf{v} > 0$). For example, when the contact angle of the octane drop was 7° , the locations of the Marangoni-induced stagnation point and the corresponding extremum point were away by more than $0.1R$. Between the two points were where τ_{Ma} and the surface flow were in opposite directions (figure 3.25).

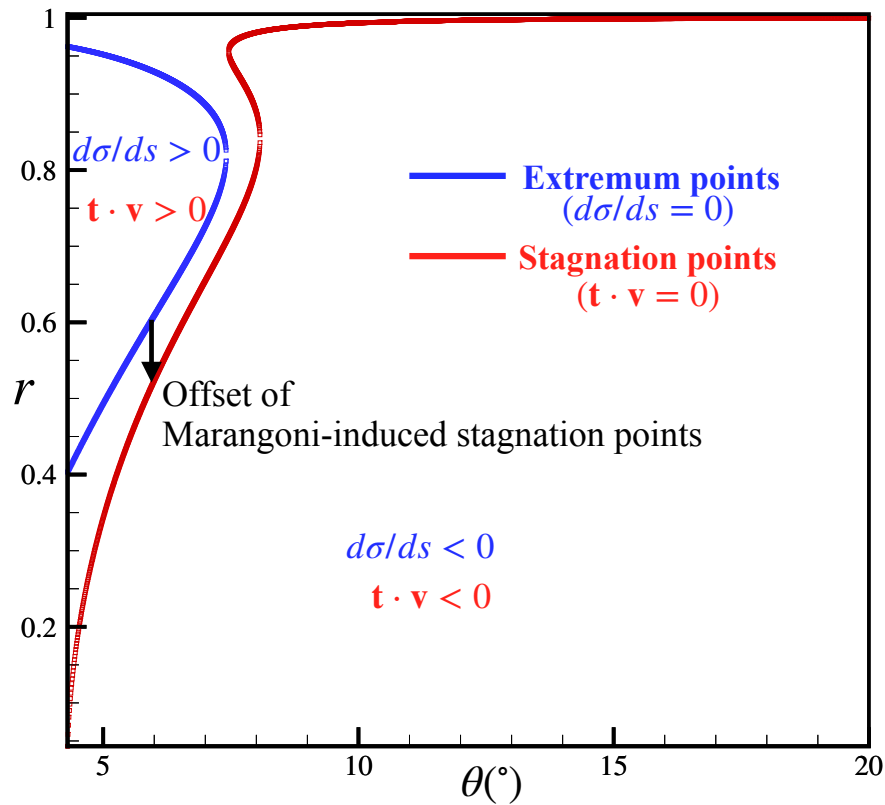


Figure 3.24. The parameters of liquid were changed to those of octane. The comparison between locations of stagnation points and extremum points showed an offset even at small r , which did not happen when the parameters were for water.

This offset can also be explained by the lubrication theory. According to (3.6), v_s is positive when $\tau_{Ma} > -\frac{8}{3} \frac{\bar{u}_r(r,\theta)}{h(r,t)}$. In other words, for a negative τ_{Ma} , when

$$|\tau_{Ma}| < \frac{8}{3} \frac{\bar{u}_r(r,\theta)}{h(r,t)} \equiv \tau_{offset}, \quad (3.7)$$

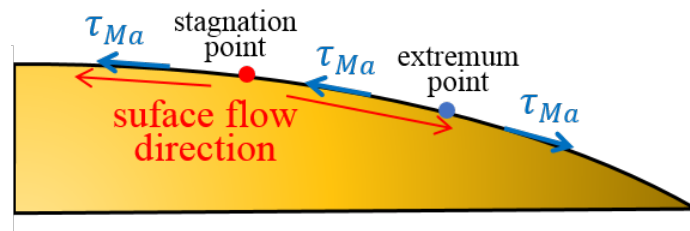


Figure 3.25. Offset of the Marangoni-induced stagnation point from the extremum point: τ_{Ma} and surface flow in opposite directions between the two points. A Marangoni-induced stagnation point located at where $\tau_{Ma} = -\tau_{offset}$, away from the extremum point where $\tau_{Ma} = 0$.

v_s is positive. (Outside capillary-induced stagnation points, this condition is accomplished by the divergence of \bar{u}_r .) Because the Marangoni-induced stagnation points are not in the vicinity of the contact line, \bar{u}_r and $h(r,t)$ are both bounded ($\bar{u}_r \sim v_c$, $h(r,t) \sim H$), thus τ_{offset} is bounded and (3.7) can be reached. Therefore, as shown in figure 3.26, a Marangoni-induced stagnation point located at where $\tau_{Ma} = -\tau_{offset}$, away from the extremum point where $\tau_{Ma} = 0$.

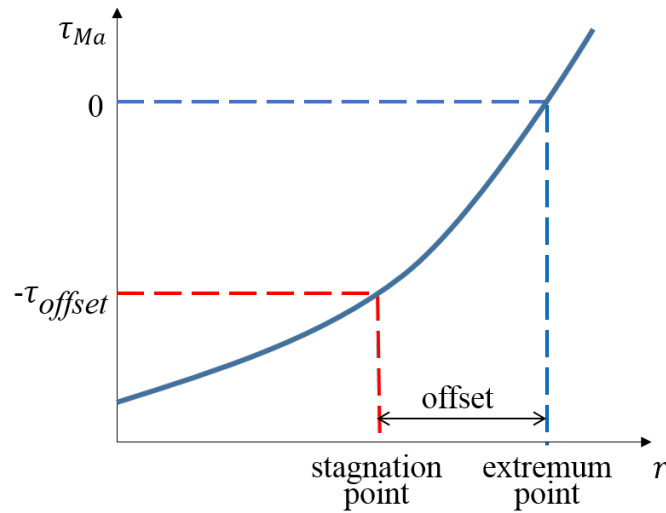


Figure 3.26. A diagram of offset of a Marangoni-induced stagnation point. The Marangoni-induced stagnation point is located at where $\tau_{Ma} = -\tau_{offset}$, away from the extremum point where $\tau_{Ma} = 0$

The offset is obvious in octane drops (figure 3.24), with similar but smaller effects in water drops (figure 3.19). The reason is the different magnitude of τ_{offset} in (3.7). It was larger for the octane drop than the water drop. From figure 3.26, larger τ_{offset} induced farther offset. By definition, the value of τ_{offset} depends on both $v_c(\sim \bar{u}_r)$ and $H(\sim h(r,t))$. On the one hand, $v_c = \frac{Dc_c}{\rho l_c}$ is larger for octane drops than water drops. On the other hand, the Marangoni-stagnation points emerged at a much lower contact angle for octane drops than water drops. So H is smaller for octane drops.

3.2.4 The Effect of Circulations on Particle Distribution

An inward flow from CL convects particles, thus reducing the CL accumulation and increasing the concentration of the location where the flow is toward. Figure 3.27 shows the particle concentrations at the drop surface with Marangoni flow or with pure capillary flow. When Marangoni flow was turned on, the concentrations for small r were larger than the case with Marangoni flow off, meaning more particles kept suspended away from CL. Marangoni flow made the concentrations at CL smaller, implying the suppression of CL accumulation. The local maxima of the concentration were at the location of stagnation points. Detailed discussion on particle suspension due to Marangoni circulation will be in the next section.

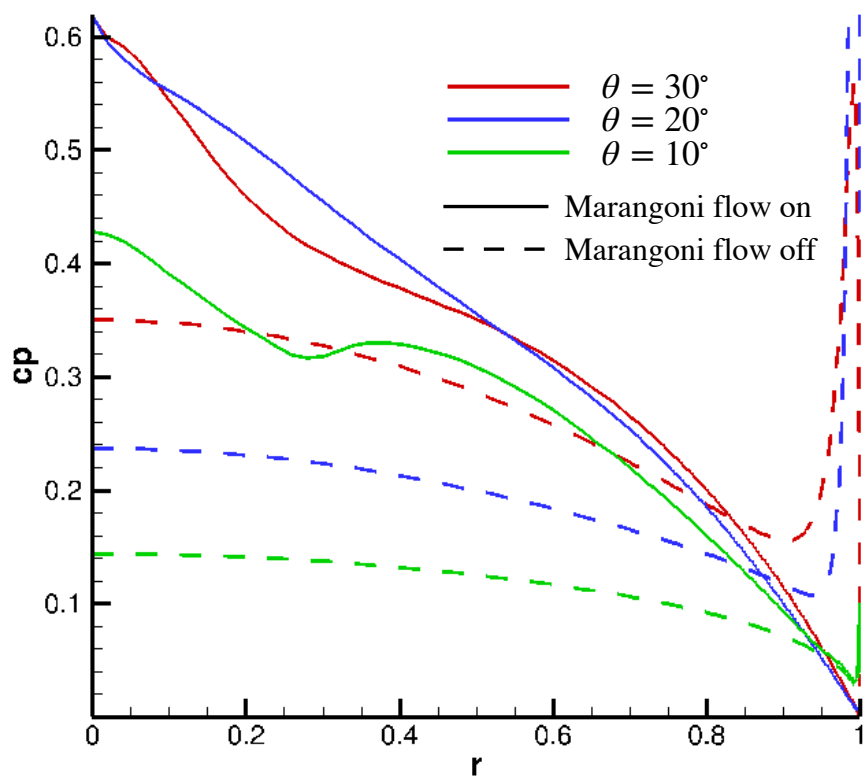


Figure 3.27. The particle concentrations c_p at the drop surface with Marangoni flow or with pure capillary flow.

3.3 Particle Distribution Affected by Marangoni Flows

We start by observing the case with no Marangoni flow and only capillary flow. There were mainly two regions where the particle concentration was higher than other regions, indicating the accumulation of particles (Figure 3.28). First, the accumulation near the contact line (CL) is the coffee-ring effect [1]. Second, the accumulation at the drop surface was due to the downward movement of the drop surface [88].

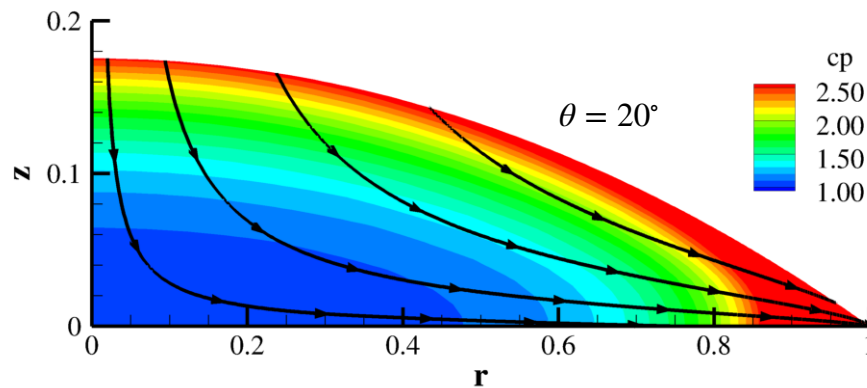


Figure 3.28. Particle concentration when $\theta = 20^\circ$ with only the capillary flow. There were mainly two regions where the particle concentration was higher than other regions: near the contact line (CL) and at the drop surface.

3.3.1 The Influence of Marangoni Flows with a Negative Ma

A negative Ma means the Marangoni stress is in the opposite direction of \mathbf{t} . A counterclockwise flow profile induced by a negative Ma caused the particles to circulate without substantial particle accumulation at the CL. A comparison of particle distribution during drop evaporation between the case with counterclockwise Marangoni flow and the case with no Marangoni flow is shown in Figure 3.29. A Marangoni number of $Ma = 10^5$ was used for the case with Marangoni flow. When CA decreased to 20° , capillary flow had transported most particles near the CL, while Marangoni circulation kept more particles suspended in the drop. The concentration at $(r = 0, z = 0)$ with Marangoni flow was more

than three times as large as the concentration with no Marangoni flow. In another word, a circulation caused by the Marangoni flow tends to make particle distribution more uniform across the drop.

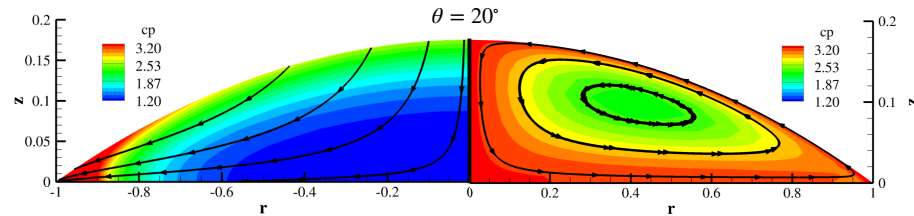


Figure 3.29. A comparison of particle distribution at $\theta = 20^\circ$ between the case with clockwise Marangoni flow and the case with no Marangoni flow. The left is the case with no Marangoni flow. A Marangoni number of $Ma = 10^5$ was used for the case with Marangoni flow. Capillary flow transported most particles near the CL, while Marangoni circulation kept particles suspended in the drop with a higher concentration.

More particles are kept in the middle of the drop with a more intense Marangoni effect. The intensity of the Marangoni effect can be represented by the magnitude of the Marangoni number Ma , since a larger Ma means larger Marangoni stresses. Figure 3.30 includes the results of multiple simulations where various values of Ma are applied in these simulations from the beginning of the evaporation till a contact angle of 20° . The mass fractions of particles that were left within $r = 0.8$ were compared, and the fraction is named x_{inner} because $r < 0.8$ was considered as the inner region of a drop. The particles are recognized to be close to CL if they were at radial locations larger than 0.8. If no Marangoni flow exists, viz. $Ma = 0 \sim 10^0$, more than a half of the total particles has reached close to CL when $\theta = 20^\circ$, according to the first point form the left in Figure 3.30. As Ma increases, more particles are kept in the inner region. For the case of $Ma = 10^5$ in Figure 3.29, more than 85% of the particles were still suspended within $r = 0.8$.

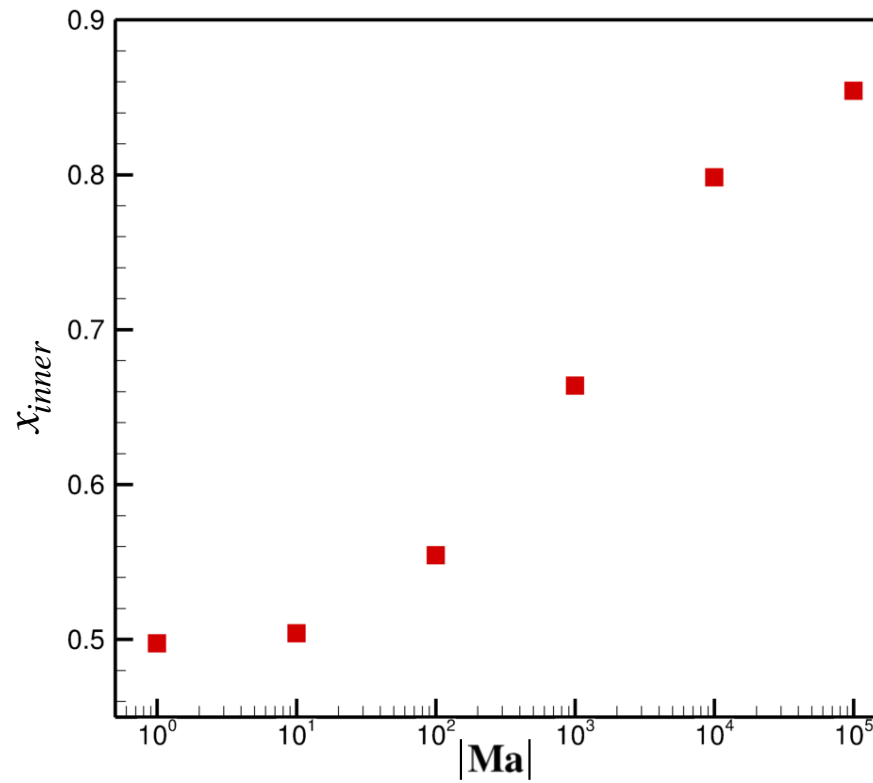


Figure 3.30. The mass fractions of particles left in the middle of the drop depend on the strength of Marangoni stresses. x_{inner} is the mass fraction of particles that located at a radial position less than 0.8 ($r < 0.8$) when CA decreased to $\theta = 20^\circ$. It is larger for larger Marangoni stresses, viz. larger Marangoni number Ma .

3.3.2 The Results with a Positive Ma

A positive Ma indicates the direction of the Marangoni stress to be the same as the direction of \mathbf{t} . A special profile with regional segregation is demonstrated by Figure 3.31. The Marangoni number used was $Ma = 10^3$. The flow profile divided the drop into two regions. One region has a clockwise circulation, and the other region presents the edge-ward flow near the CL. The edgeward flow transported the accumulated particles at the drop surface to CL, while the circulation made the particle concentration within the circulation region uniform. Therefore, compared to the capillary flow case, the drop surface had lower particle concentrations, and the high concentration only showed near CL within the edgeward-flow region. This flow profiles resulted in a smaller particle concentration gradient in the axial direction. The concentration change was mainly in the radial direction, while the change for a capillary flow case was both in the radial direction and the axial direction.

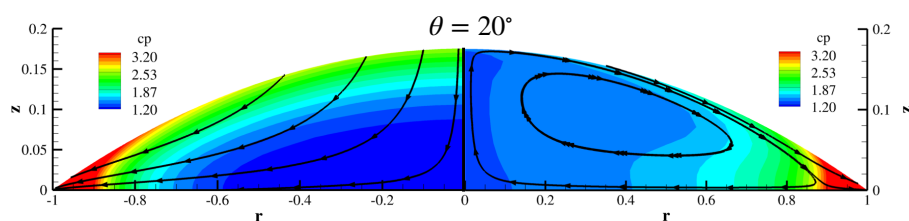


Figure 3.31. The profile on the right is with a reverse Marangoni stress of $Ma = 10^3$. The flow profile divided the drop into two regions. One is the clockwise circulation, and the other is the edgeward flow near the CL. The edgeward flow transported the accumulated particles at the drop surface to CL, while the circulation made the particle concentration within the circulation region uniform. Therefore, compared to the capillary flow case on the left, the drop surface presented lower concentration, and the high concentration only showed near CL.

The two-region flow profile is featured with a transition point at the bottom of the drop as is shown in Figure 3.32. The transition point in Figure 3.31 is between $r = 0.85$ and $r = 0.9$. On the left of the transition point, the flow is toward the center of the drop along

the bottom; and on the right, the flow is toward CL. The mathematical expression of the left side is $\partial u/\partial z < 0$ and vice versa, since the application of no-slip BC gives $u = 0$ at $z = 0$. The transition point has a radial location r_T where $\partial u/\partial z = 0$. The radial location of the transition point r_T moves during evaporation as the CA, θ , decreases. With $Ma = 10^3$, the trend is shown with the red dots in Figure 3.33. At the early stage of evaporation when θ was 40° , the point at the very right indicates $r_T > 0.9$. The location kept near $r = 0.9$ between 20° and 40° , however, moved inward rapidly as *theta* decreases below 20° .

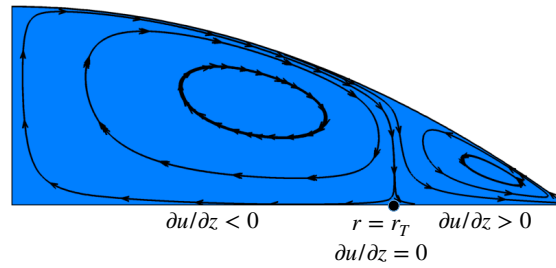


Figure 3.32. On the left of the transition point, the flow is toward the center of the drop along the bottom; on the right, the flow is toward CL. The mathematical expression of the left side is $\partial u/\partial z < 0$ and vice versa, since the application of no-slip BC gives $u = 0$ at $z = 0$. The transition point has a radial location r_T where $\partial u/\partial z = 0$.

The location of the transition point can be predicted by an application of the lubrication theory on the drop, which was used in previous research [46,62,78]. The symbol of $\partial u/\partial z$ is to be investigated with the following equation:

$$\frac{\partial u}{\partial z}\Big|_r = 3\frac{\bar{u}(r_T, \theta)}{h(r_T, \theta)} - \frac{1}{2}Ma, \quad (3.8)$$

where Ma is the Marangoni stress in \mathbf{t} direction. The equation was derived as the following paragraph from the results of the radial velocities based on the lubrication theory.

The lubrication theory is valid for a drop with a CA as high as 40° according to Hu and Larson [46]. The height-averaged radial velocity for capillary flow was derived from mass balance as equation 3.9, where $A(\theta)$ is a coefficient that changes as the drop evaporates.

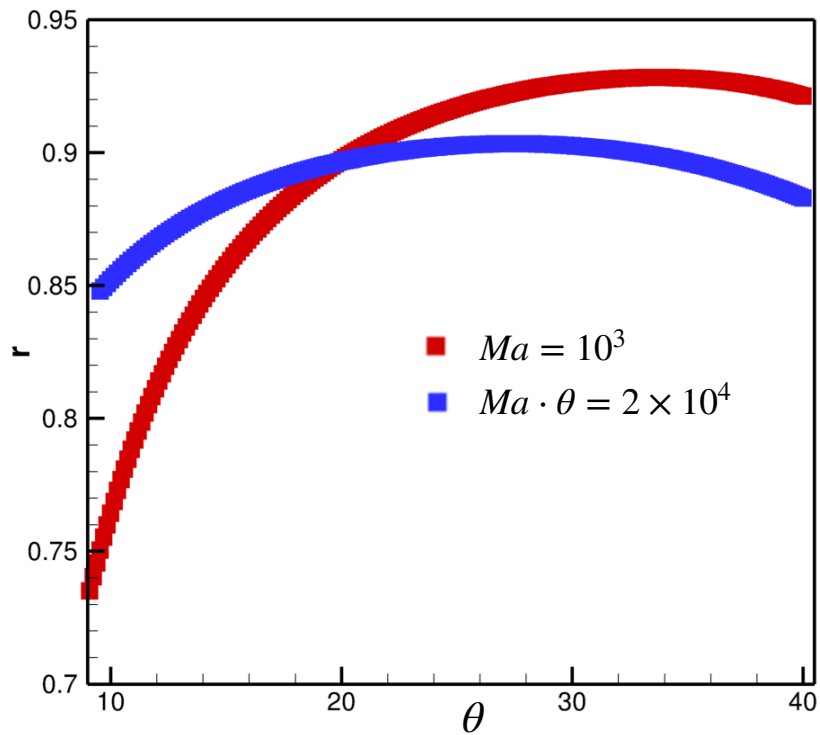


Figure 3.33. The radial location r of the transition point changes as the CA, θ , decreased during drop evaporation (θ value changes from the right to the left of the abscissa). A fixed $Ma = 10^3$ led to a distinct movement of the transition point (r_T changed by 0.2). Setting $\theta \cdot Ma = 2 \times 10^4$ restricted r_T between $r = 0.85$ and $r = 0.9$. The moving distance of the transition point was much smaller than the case with a constant Ma .

The mass balance keeps the same with or without Marangoni stress; therefore, the height-averaged radial velocity $\bar{u}_{r(r,\theta)}$ is essentially the same as 3.9 when Marangoni flow exists.

$$\frac{1}{h} \int_0^h u dz = \bar{u}_{(r,\theta)} = A_{(\theta)} \frac{1}{r} \left[(1-r^2)^{-\lambda(\theta)} - (1-r^2) \right] \quad (3.9)$$

Besides, the following boundary conditions were applied:

$$u|_{z=0} = 0, \quad (3.10)$$

and

$$\left. \frac{\partial u}{\partial z} \right|_{z=h(r,t)} = Ma, \quad (3.11)$$

where Ma is the Marangoni stress in \mathbf{t} direction. The radial velocities for a certain r are parabolic in z as $u_{(r,\theta)} = Az^2 + Bz + C$ from lubrication theory. Substituting Equation 3.9, 3.10 and 3.11, the velocity has a form of

$$u_{(r,z,\theta)} = \left(\frac{3Ma}{4h} - \frac{3\bar{u}}{2h^2} \right) z^2 + \left(3\frac{\bar{u}}{h} - \frac{1}{2}Ma \right) z. \quad (3.12)$$

Then at $(r, z = 0)$,

$$\left. \frac{\partial u}{\partial z} \right|_r = 3 \frac{\bar{u}_{(r_T,\theta)}}{h_{(r_T,\theta)}} - \frac{1}{2}Ma. \quad (3.13)$$

Equation 3.8 can be used to explain the inward movement of the transition point shown by the red dots in Figure 3.33. At the transition point, $\partial u / \partial z = 0$. A certain location $r = r_0$ was investigated as follows. If $\partial u / \partial z < 0$ at r_0 , the transition point is on the right of r_0 , viz. $r_T > r_0$, and vice versa (refer to Figure 3.32). As θ decreases during evaporation, $h_{(r_0,\theta)}$ decreases and $u_{(r_0,\theta)}$ increases, leading to an increase of $\partial u / \partial z$ according to Equation 3.8. The increase of $\partial u / \partial z$ from negative to positive means the movement of the transition point from $r_T > r_0$ to $r_T < r_0$. As a result, the transition point moves farther from CL as evaporation proceeds.

It is possible to restrict r_T within a certain range during evaporation by changing Ma to make $(h_{(r_T)} \cdot Ma)$ constant, according to Equation 3.8. If $h_{(r_T)}$ is approximated by $\theta(1 - r_T)$, then $(\theta \cdot Ma)$ should be constant. We tested by setting $\theta \cdot Ma = 2 \times 10^4$, and got the location of the transition point as the blue dots in Figure 3.33. The location r_T was restricted

between $r = 0.85$ and $r = 0.9$. The moving range of the transition point was much smaller than the case with a constant Ma (the red dots in Figure 3.33).

The reason why r_T was restricted in a range instead of at a fixed value was the errors from the two assumptions. The assumptions when restricting r_T with ($h_{(r_T)} \cdot Ma = \text{constant}$) were: 1) the change of $\bar{u}_{(r,\theta)}$ with θ is negligible, which fails when θ becomes small; 2) $h_{(r_T)} = \theta(1 - r_T)$, which fails when θ is large. These two assumptions brought the deviations of the value of r_T .

The range of r_T can be adjusted by the value of $(\theta \cdot Ma)$. In figure 3.34, the transition point stayed at different ranges of radial positions when $\theta \cdot Ma$ was 2×10^4 , 1×10^4 and 5×10^3 respectively. The larger $\theta \cdot Ma$ is, the closer to CL the transition point stays. The reason is the same as the explanation of the change of r_T with Ma .

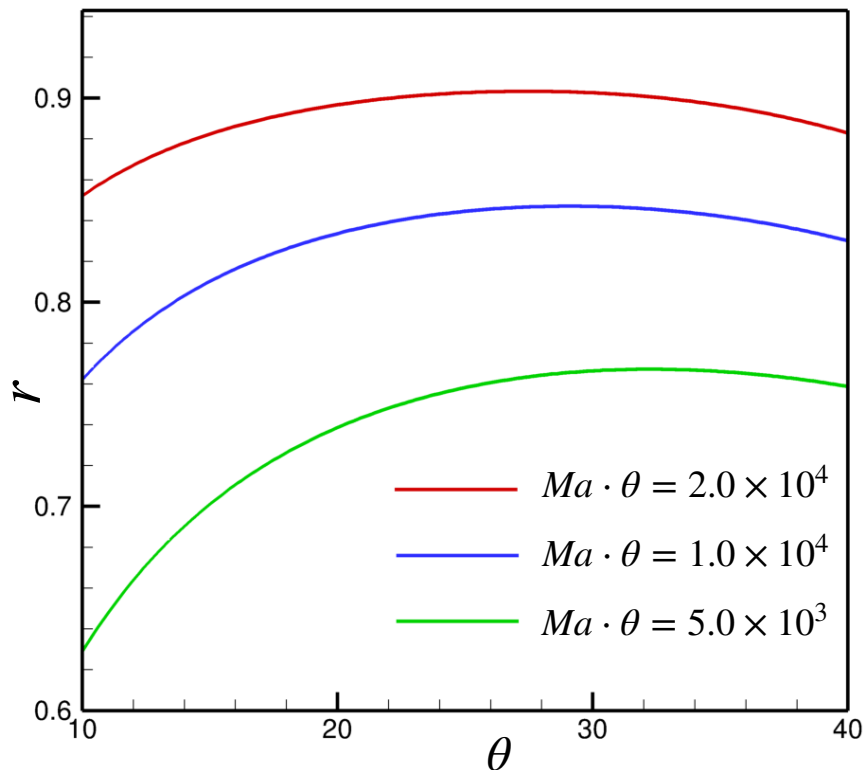


Figure 3.34. The transition point stayed at different ranges of radial positions r when $\theta \cdot Ma$ has different values.

A larger Marangoni stress, viz. a larger Ma , brings the transition point closer to CL. Figure 3.35 shows the locations of transition points r_T under various Ma at a contact angle of 20° . According to the result of the lubrication theory (Equation 3.8), for a certain θ , when Ma is larger, the first term needs to be larger to give $\partial u/\partial z = 0$. This requires a larger r_T so that $\bar{u}_{(r_T, \theta)}$ is larger and $h_{(r_T, \theta)}$ is smaller.

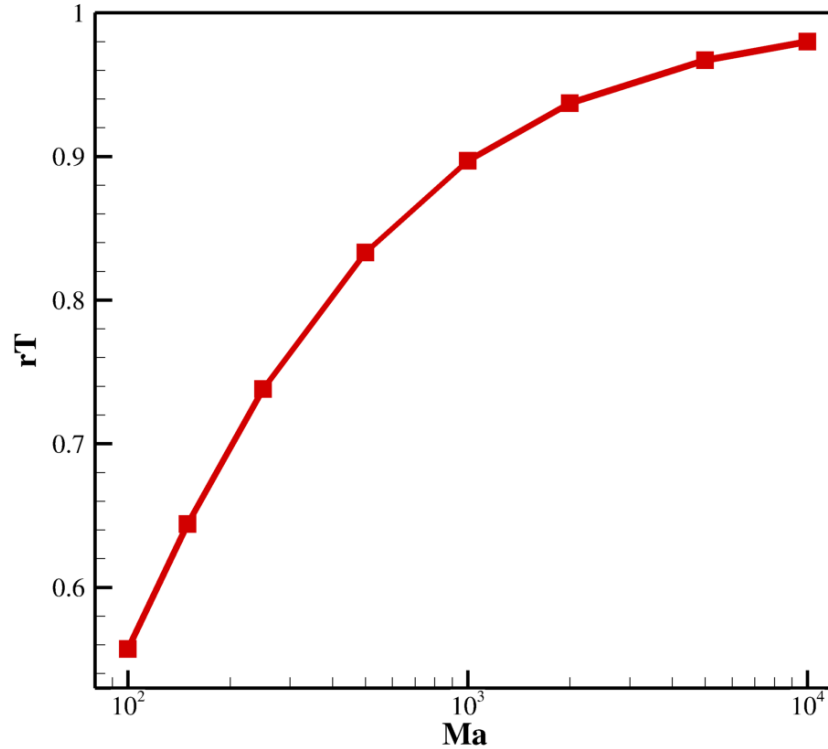


Figure 3.35. The locations of the transition point r_T under various Ma at a contact angle of 20° .

The change of r_T with CA is plotted in Figure 3.36, which shows both facts that a transition point locates closer to CL with a larger Ma and that a transition point moves inward as evaporation proceeds for the case of a fixed Ma .

The Ma value has to be within a certain range to result in a transition point, or in other words, to lead to the edgeward flow region beside the clockwise circulation. As Ma increases, the transition point gets closer to CL, and at last reaches CL and disappears. For

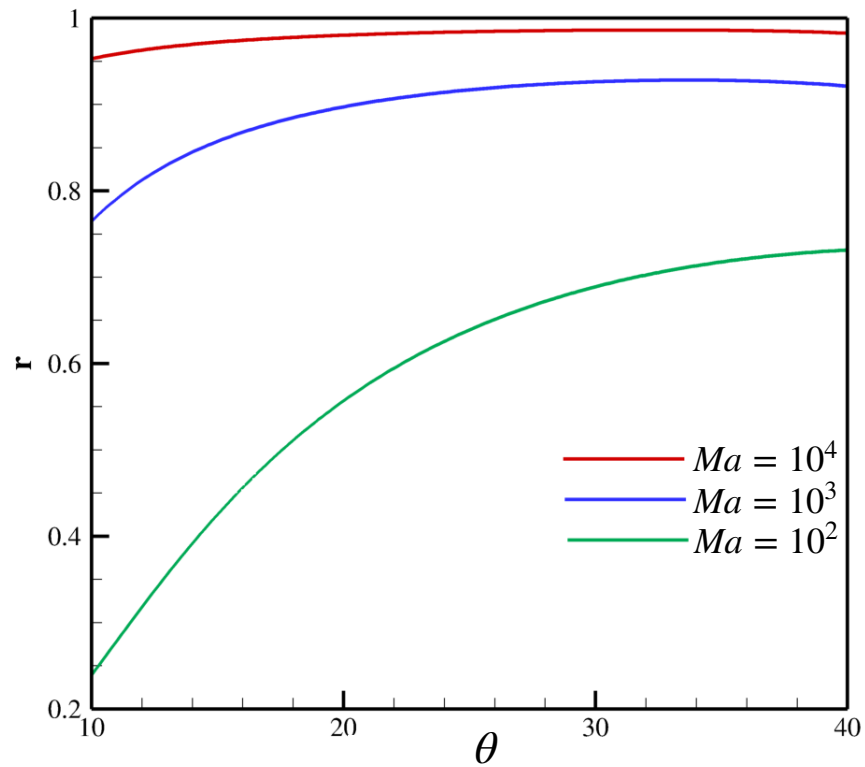


Figure 3.36. The change of r_T with CA θ when different Ma was imposed. The transition point moved inward as evaporation proceeds for the case of a fixed Ma .

example, if $Ma = 10^5$, the flow profile is circulation with no edgeward flow or transition points as is shown in Figure 3.37(a).

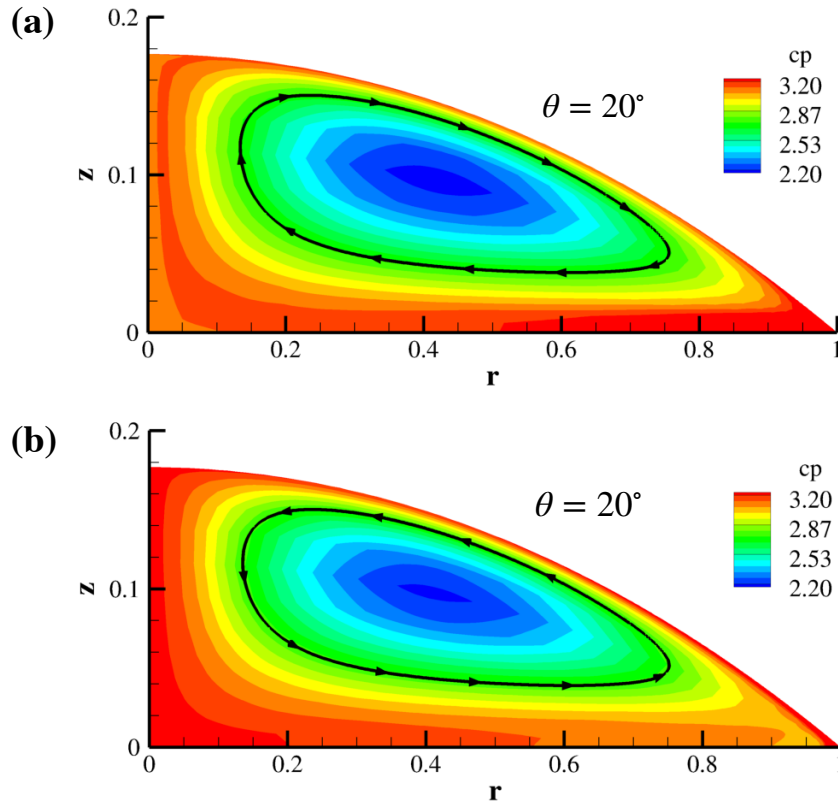


Figure 3.37. Profiles at $\theta = 20^\circ$ with $Ma = 10^5$ (Figure (a)), where clockwise circulation was formed, and $Ma = -10^5$ (Figure (b)), where counterclockwise circulation was formed. The scale bars for c_p are the same. The clockwise circulation and counterclockwise circulation lead to similar particle distribution.

The effects of the change of Ma on particle distribution can be shown by Figure 3.38, which presents the mass fraction of particles kept within $r = 0.8$. Distinct from the results of counter-clockwise circulations in Figure 3.30, the mass fraction first decreased as Ma increased, and then rapidly increased. For a low Ma of the clockwise circulation, the flow profiles had an edgeward flow region. In this region, the edgeward Marangoni flow strengthened the transport of particles toward the CL, leading to less particles at the inner

region. When Ma was high enough, the edgeward flow region disappeared, and the circulation tended to even the distribution of particles across the whole drop, keeping particles suspended at the inner region.

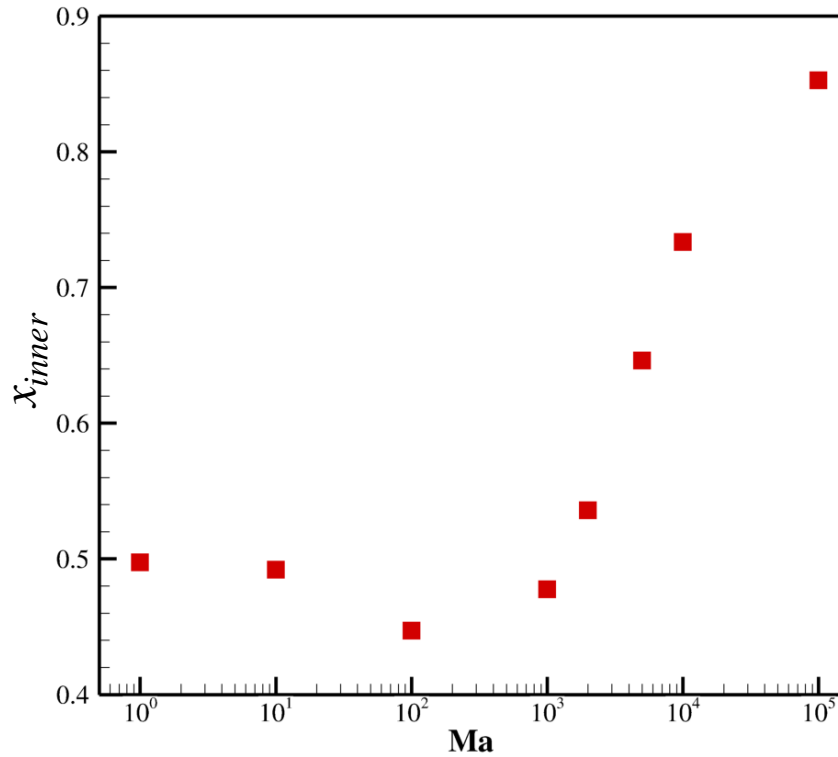


Figure 3.38. The mass fractions of particles left in the middle of the drop versus Ma when Marangoni stresses are in the direction from the top to CL. x_{inner} is the mass fraction of particles that located at a radial position less than 0.8 ($r < 0.8$) when CA decreased to $\theta = 20^\circ$.

The amount of particles at the inner region was similar for a clockwise Marangoni flow and for a counter-clockwise Marangoni flow when $Ma = 10^5$, which is indicated by the last point in Figure 3.30 and Figure 3.38. Actually, even the particle distribution was similar as Figure 3.37, which used the same scale bar for c_p and presents the similar concentration profiles with low concentrations in the middle of the domain.

3.3.3 Results of Thermal Marangoni Flows

The flow and concentration profiles are more complex when there is thermal Marangoni circulations. Depending on the time of the evaporation and the location of the surface, there could be an increase or a decrease of the temperature in the \mathbf{t} direction, which was shown by the left side of Figure 3.39, 3.40 and 3.41. At first, a counter clockwise circulation was caused by the Marangoni flow toward the top of the drop (Figure 3.39). The Marangoni flow results from the decrease of temperature from CL to the top of the drop. Later, the change of the temperature on the surface became non-monotonous, leading to Marangoni flows in different directions. The change of Marangoni flow directions resulted in a flow profile of two circulations (Figure 3.40). The circulation close to CL was counterclockwise, and the other was clockwise. Between the two circulations at the drop surface, a Marangoni-induced stagnation point existed at the minimum of temperature [78]. As the contact angle (CA) decreased, the temperature minimum located closer to CL. As a result, the counterclockwise circulation was smaller and shrank to the corner near CL (Figure 3.41).

Distribution of particles changed greatly with the flow profile change. The bulk particle concentrations, c_p , right below the drop-air interface are also plotted separately for a more obvious presentation as Figure 3.42. The surface concentration of the particles is affected by the surface flow directions, and the stagnation point results in further accumulation beyond the surface accumulation.

When the surface flow was toward the top throughout the whole drop, the accumulated particles at the surface further accumulated near the top, as in Figure 3.39 and the blue line in Figure 3.42. The circulation caused by the surface flow played the same role as the circulations from fixed Ma as Figure 3.37, which is to keep particles suspended in the drop rather than deposited at the CL. The early suspension makes it possible for later control of deposition locations.

Later when there was a stagnation point at the surface between the two circulations, particles gathered around the stagnation point (Figure 3.40 and the pink line in Figure

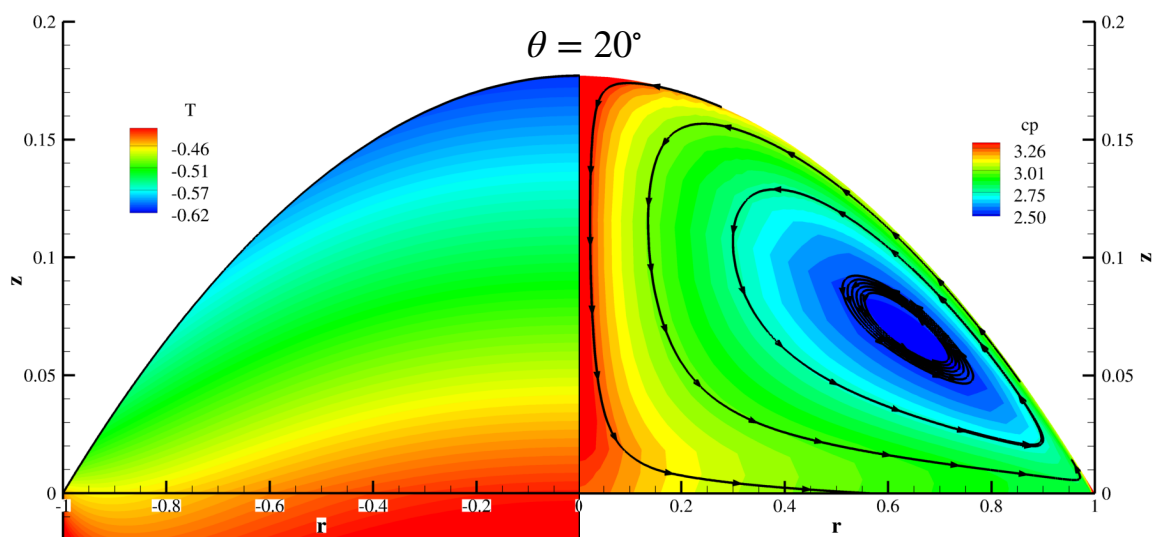


Figure 3.39. Temperature, flow and concentration profiles at the CA of $\theta = 20^\circ$. The temperature profile is the left side and shows both the drop domain and the substrate domain. A counter clockwise circulation was caused by Marangoni flow toward the top of the drop. The Marangoni flow results from the decrease of temperature from CL to the top of the drop.

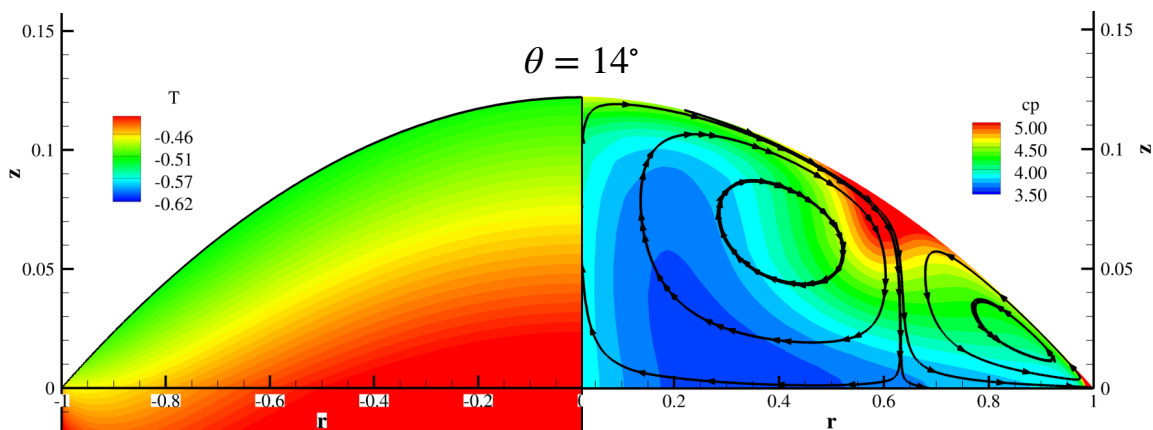


Figure 3.40. The temperature T change on the surface of the drop became non-monotonous. A flow profile of two circulations presented at $\theta = 14^\circ$. The circulation close to CL was counterclockwise, and the other was clockwise. Between the two circulations at the drop surface, a Marangoni-induced stagnation point existed at the minimum of temperature. The particle concentrations c_p near the stagnation point were large.

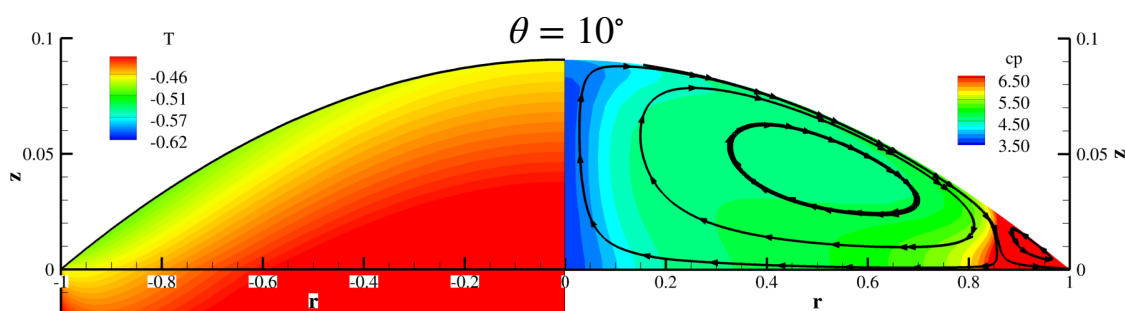


Figure 3.41. At $\theta = 10^\circ$, the temperature minimum located close to CL. There were still two circulations. The counterclockwise circulation near CL took up a small corner of the drop. The particle concentrations c_p inside the CL circulation were the largest.

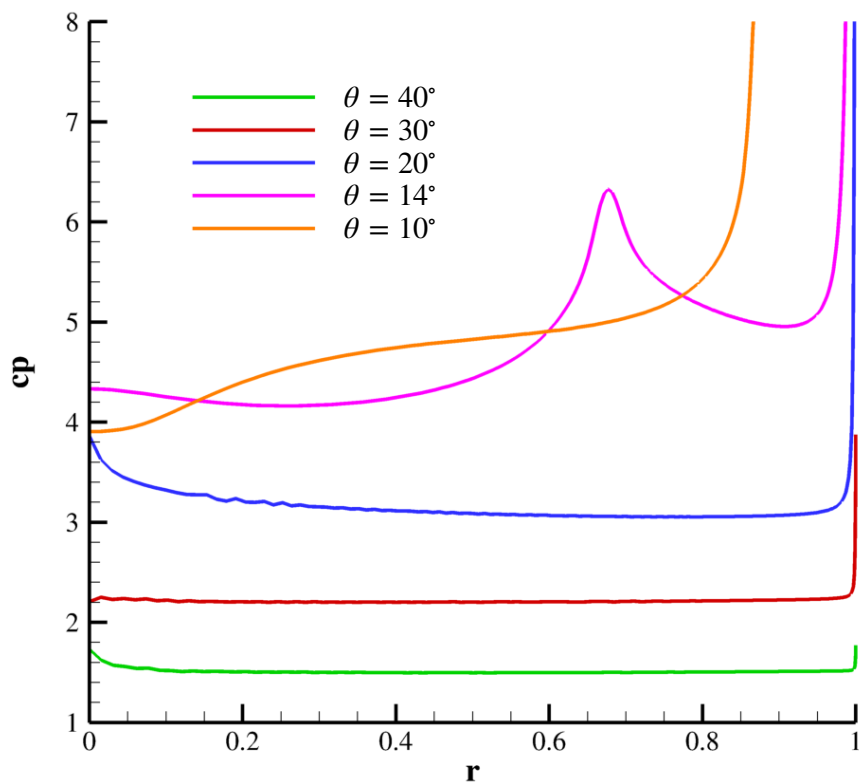


Figure 3.42. The values of the concentrations c_p at different radial locations r of the drop surface at various CAs θ .

3.42). At the late stage, when the stagnation point was close to CL, the effects of the stagnation point accumulation and the CL accumulation combined together, causing a high concentration at the corner (profile 3.41 and the yellow line in Figure 3.42).

The distribution of particles was also influenced by the vertical flow: a flow from the surface to the bottom of the drop convects particles downward. Due to particle accumulation near the surface, the downward convection increases the local concentration beneath the surface. Coincidentally, the surface accumulation around the stagnation points and the downward convection happened around the same radial position, leading to an even more obvious increase of concentrations at that radial position. This increase was illustrated by the higher concentration at the center of the drop in Figure 3.39, at a radial position around $r = 0.6$ in Figure 3.40 and near CL in Figure 3.41. Similarly, an upward flow decreases the particle concentration, which was manifested by the center of Figure 3.40 and 3.41.

3.3.4 Regional Segregation in Thermal Marangoni Circulations

The regional segregation with the natural thermal Marangoni flow is shown in Figure 3.41 where the drop was divided into two regions by the two circulations. Compared to the regional segregation with a fixed Ma , there is a counter-clockwise circulation close to CL.

The Marangoni stress in the CL region is in the opposite direction to the Marangoni stress in the clockwise circulation region, which is indicated by opposite signs of Ma calculated from thermal Marangoni stresses. The Marangoni number for the thermal Marangoni stress is expressed as $Ma = \frac{\beta T_c}{\mu_0 \nu c l_c} \nabla_s T$, which changes with both the time of evaporation and the location of the drop. The surface temperature and the corresponding Ma were plotted in Figure 3.43. There is a temperature minimum, where Ma changes from negative to positive. The temperature minimum is the surface tension maximum, which pulled the liquid on the surface and led to the two circulations. If a surface tension maximum is caused by other factors, such as surfactants, the regional segregation will also happen.

The regional segregation of flows resulted in a particle concentration plateau. The circulations make particle distribution uniform in each region. Because of the segregation, the concentration across the region boundary changed greatly, which is shown by the con-

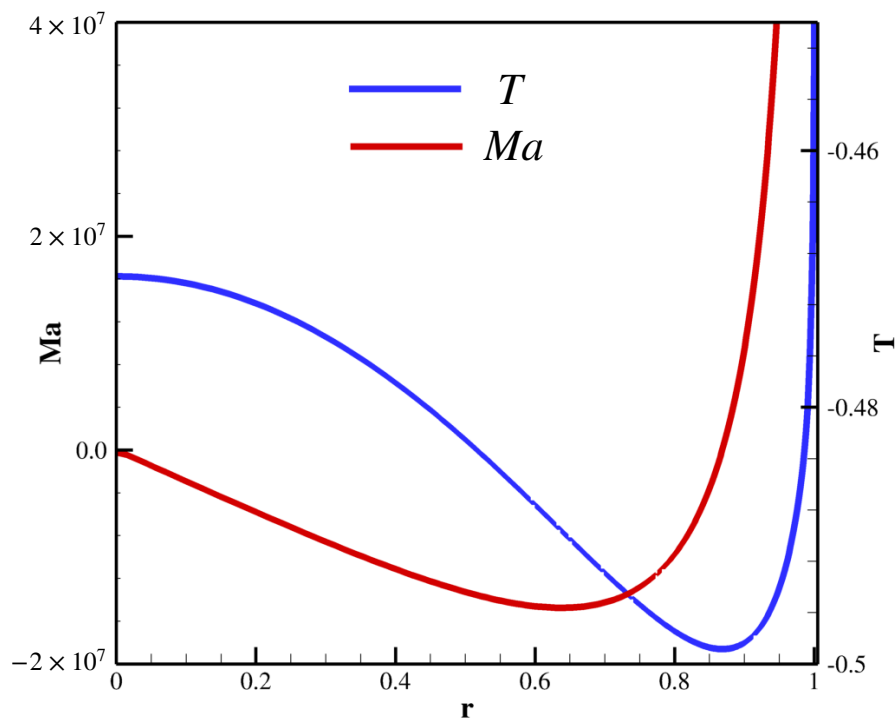


Figure 3.43. The surface temperature T and correspondent Marangoni number Ma changing with radial positions r . The Marangoni stress (Ma) magnitude was determined by the temperature gradient on the surface. Ma in the CL region is quite large due to the sharp temperature change. The results are at $\theta = 10^\circ$ with a condition of $d = 0.5$.

centration contours in Figure 3.41. The plot of the concentration at the surface at different radial locations, shown by the red line in Figure 3.44, also manifests the concentration difference due to the regional segregation. The plateau at $r > 0.8$ indicates the trap of a large portion of particles in the CL circulation region. The CL circulation and the high-particle-concentration region near the CL were also observed in the experiments by Parsa et al. [77] (Figure 4 in their paper). We were not able to compare with their work to get an agreement because the substrate thickness was not given in their paper. However, a qualitative agreement on the radial width of the CL region was reached. Our simulation gives the width of around 0.2, and their experiments showed a dimensionless width of $\frac{300\mu m}{1mm} = 0.3$. Future experiments can be done to validate this comparison.

Although the particle concentration plateau indicates a CL accumulation, it is distinct from the “coffee ring effect” which is caused by purely edgeward capillary flows. The CL accumulation brought by the capillary flow is indicated by the green line in Figure 3.44, and is featured with a smooth increase of the concentration approaching the CL. Compared to this accumulation, the segregated CL circulation produced a width of particle accumulation region, implying the spreading of the CL accumulation and a wider “coffee ring”. The spreading may be the reason why the profiles of particle deposition in experiments were lower and wider than the numerical results of Bhardwaj et al. [75] (Figure 13 of the paper).

Based on the above results of thermal Marangoni flow, an understanding to the Marangoni effect was provided at different stages of evaporation. The early effect keeps particles from accumulating at the CL. The later effect leads to regional segregation that affects the width of particle accumulation. The understanding provides potential methods to control the width of the “coffee ring” deposition.

Since the transition point is the boundary of the CL circulation, the ring width is determined by the transition point location. As a result, the width can be manipulated by designing the transition point location.

A more feasible way to design the location of transition points, compared to exerting corresponding Ma in Section 3.3.2, is to change the thickness of the substrate. The blue line in Figure 3.44 is the results for a substrate with a thickness of $d = 1.5$. The plateau

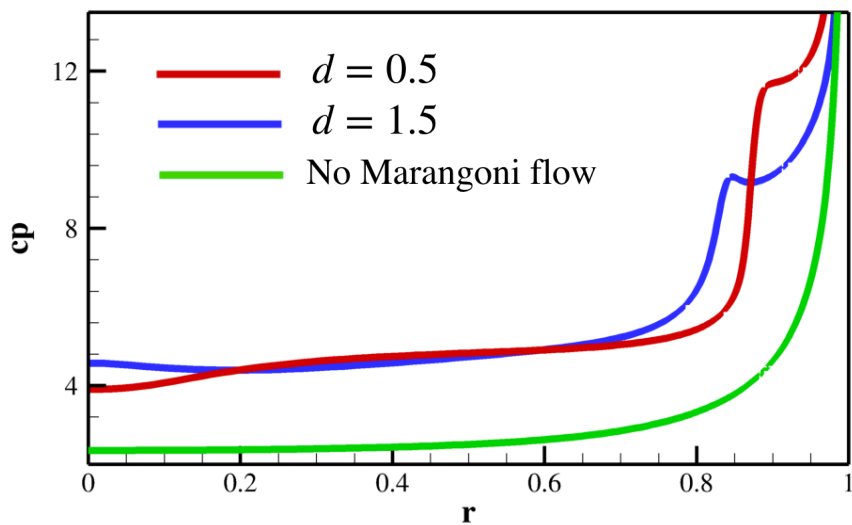


Figure 3.44. The concentration at the surface at different radial locations at $\theta = 10^\circ$. The green line shows the CL accumulation brought by the capillary flow, featured with a smooth increase of the concentration approaching CL. The red and the blue lines are results with thermal Marangoni flow. They manifest the concentration difference due to the regional segregation. The larger substrate thickness d led to a wider CL concentration plateau.

is wider than that of a substrate with $d = 0.5$, meaning the particle accumulation zone is wider due to farther distance of the transition point from CL.

The locations of transition points changing with the contact angle during evaporation are shown in Figure 3.45. Various thickness of the substrate was used. The thicker the substrate was, the later (at a smaller contact angle) a turning point emerges. If a certain contact angle is to be investigated, the turning point locates farther from CL for the thicker substrate case. When the thickness reached a certain value, increasing the thickness does not change r_T any more, which is indicated by the overlap of the results for $d = 1.5$ and $d = 2.0$.

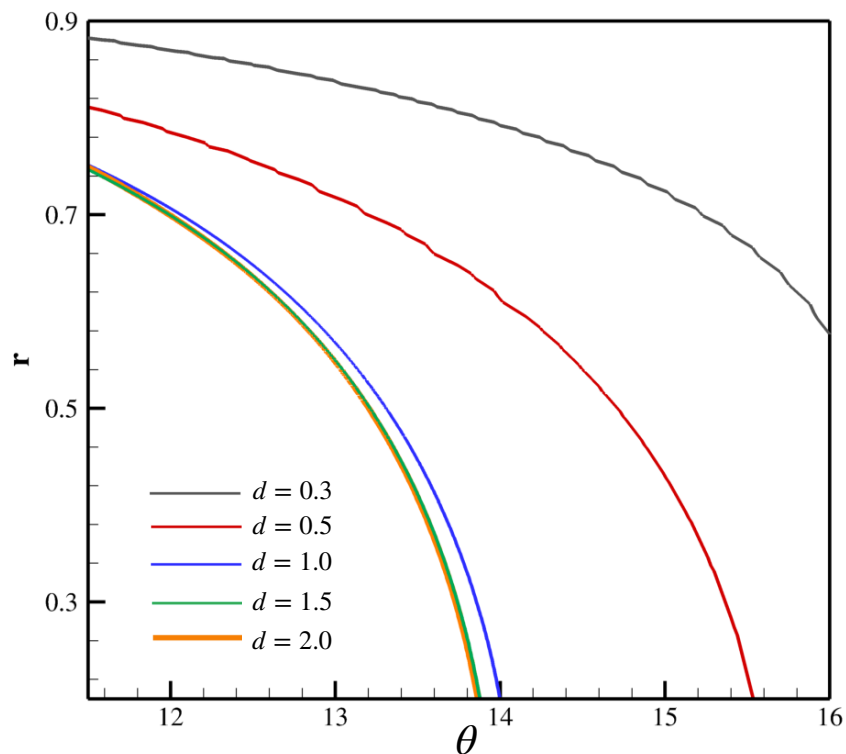


Figure 3.45. The locations r of transition points changing with the contact angle θ during evaporation. The thickness of the substrate d determined how early a transition point emerged and how far the transition point was away from CL. If d is larger than 1.5, increasing the thickness does not make a difference anymore.

It is noticeable that a transition point first emerged at the center of the drop, $r_T = 0$, and then moved outward toward CL. During the movement, there was first local accumulation around $r = r_T$ at the surface, which is shown in Figure 3.40. Then when the transition point approached CL, the accumulation gathered in the CL circulation region.

What is more importantly, the CL accumulation region was restricted by the CL circulation and shrank with the transition point movement. In Figure 3.46, the high concentration region was restricted between the transition point and the CL. The radial width of the region decreased due to the movement of the transition point. The contours used in Figure 3.46 are for the normalized particle concentration $c_{pN} = c_p/c_{pA}$, where c_{pA} is the averaged concentration for the current CA, and was calculated by $c_{pA} = c_{p0} \times V_0/V$, where c_{p0} and V_0 are the initial concentration and volume respectively, and V is the current volume. The normalized concentration c_{pN} was used to facilitate the comparison between drops of different CAs, which stand for different stages of evaporation. Otherwise, the average concentration increases as CA lowers, and the distribution cannot be clearly shown by c_p .

Another factor affecting the transition point location is the heat conductivity ratio of the drop and the substrate k_R . It is easier to change to substrate material, so k_R can be changed by adjusting k_S , the substrate heat conductivity. As Figure 3.47, the smaller k_S value was, the earlier a transition point emerged and the closer the transition point pushed the CL accumulation region to CL.

The temperature profiles for different k_S values are shown by Figure 3.48 and 3.49 with representative values for k_S as 0.6 and 1.2. At the early stage of evaporation, the temperature at the top of the drop was the lowest. This state lasted longer when k_S was larger. When $\theta = 14^\circ$, the lowest temperature was still at the top for $k_S = 1.2$ (Figure 3.49), while it was around $r = 0.8$ for $k_S = 0.6$ (Figure 3.48). Only when the lowest temperature is not at the top does a transition point starts to emerge. This is the reason for later emergence of a transition point with a larger k_S .

Similarly, the temperature profiles for various substrate thickness are shown by Figure 3.50 and 3.51.

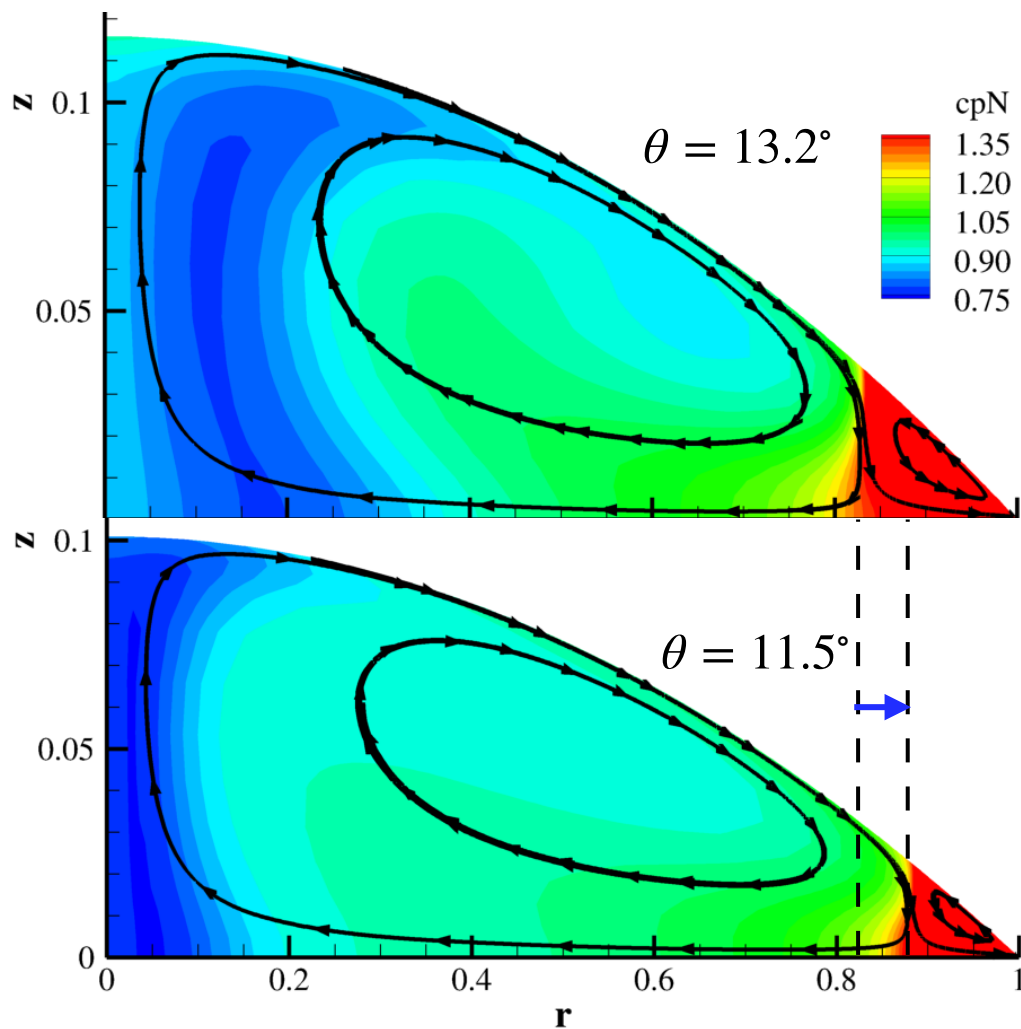


Figure 3.46. The high concentration region was restricted between the turning point and CL, and was pushed shrinking by the transition point. The contours are for the normalized particle concentration $c_{pN} = c_p/c_{pA}$, where c_{pA} is the averaged concentration for the current CA.

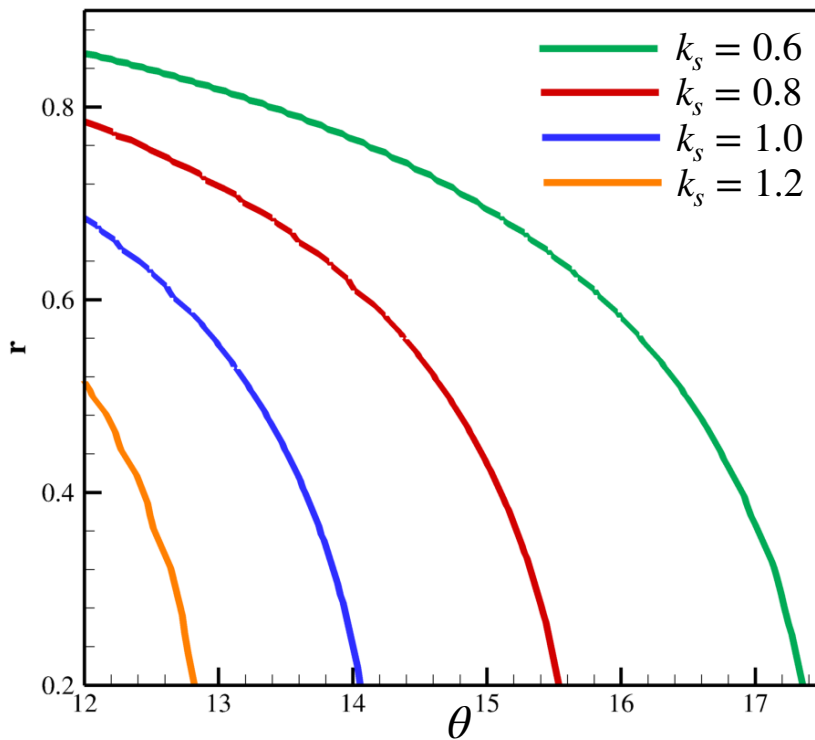


Figure 3.47. The locations r of transition points changing with the contact angle θ during evaporation. The thermal conductivity of the substrate k_s determined how early a transition point emerged and how far the transition point was away from CL.

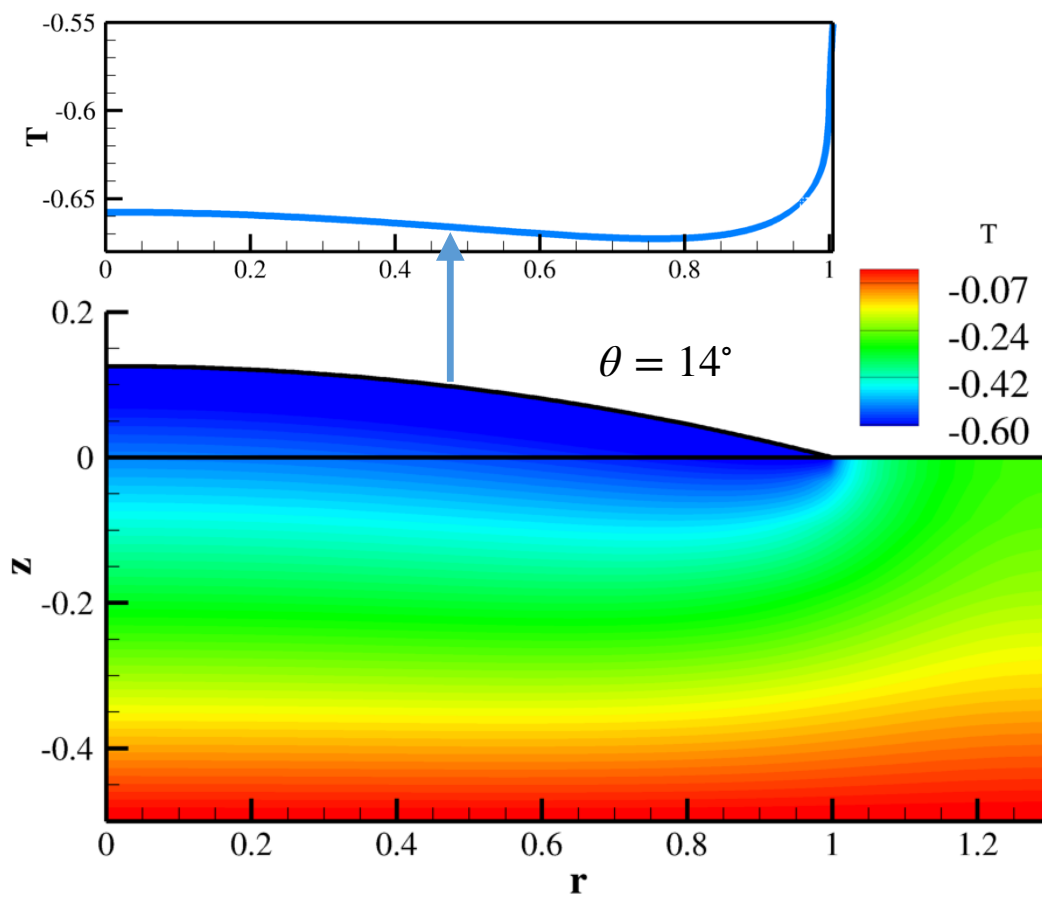


Figure 3.48. The temperature profiles for $k_s = 0.6$. The surface temperature was plotted separately. The results are with $d = 0.5$.

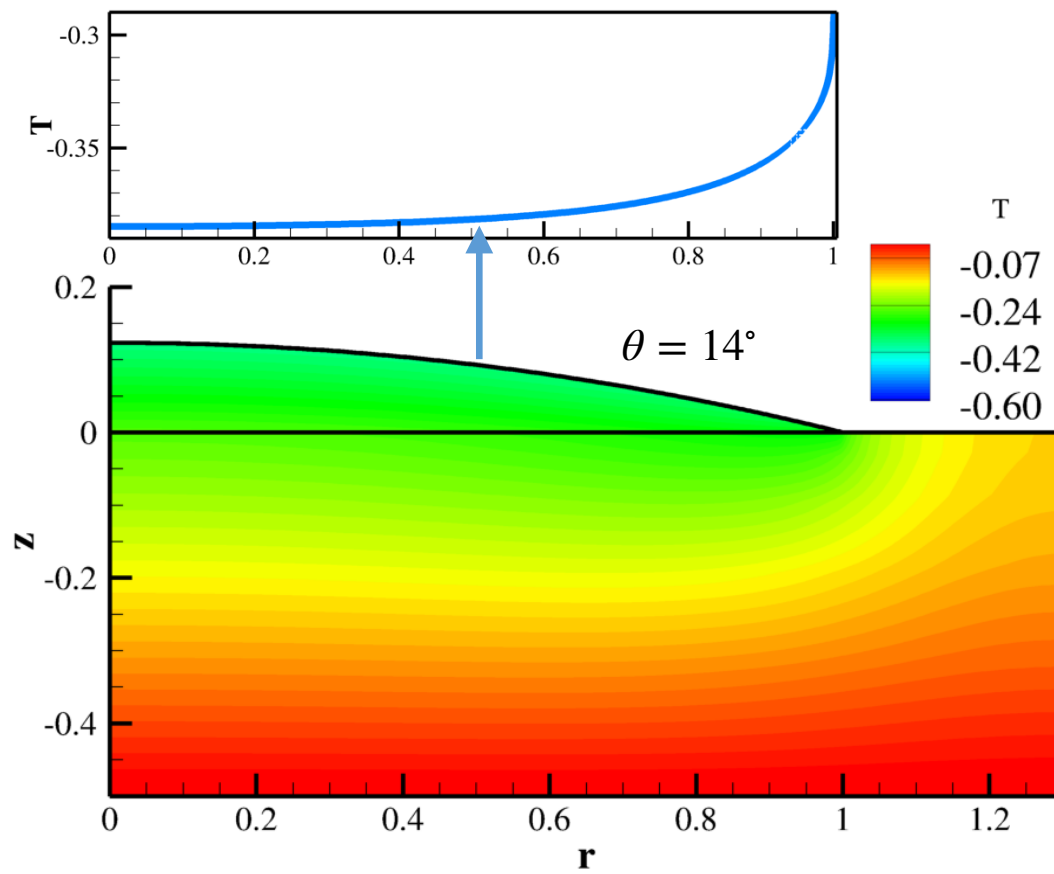


Figure 3.49. The temperature profiles for $k_s = 1.2$. The surface temperature was plotted separately. The results are with $d = 0.5$.

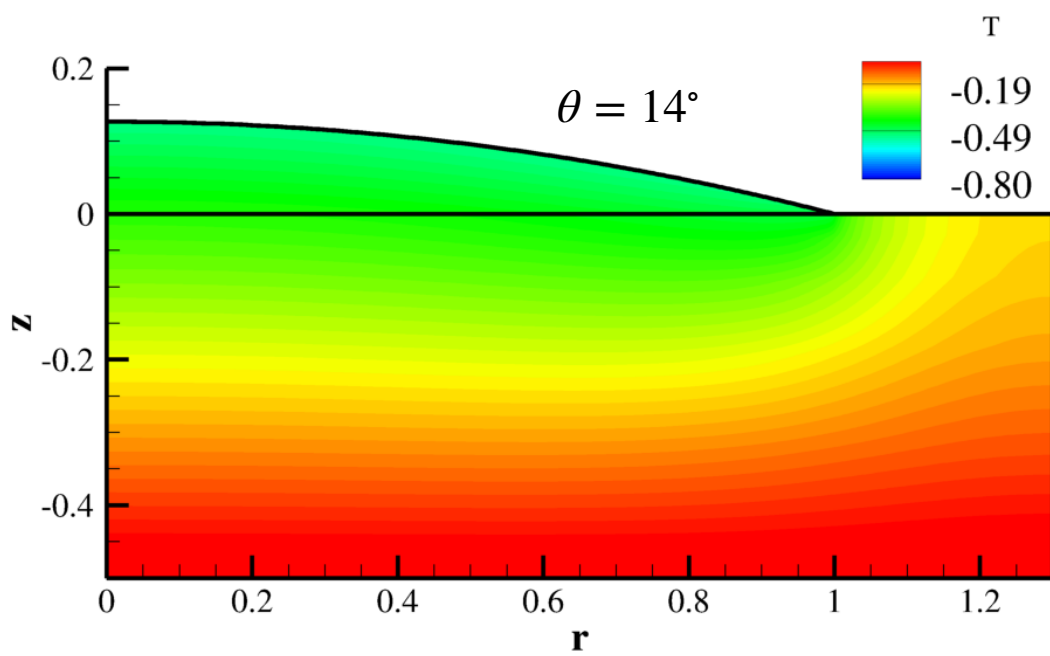


Figure 3.50. The temperature profiles for $d = 0.5$, $k_s = 0.8$.

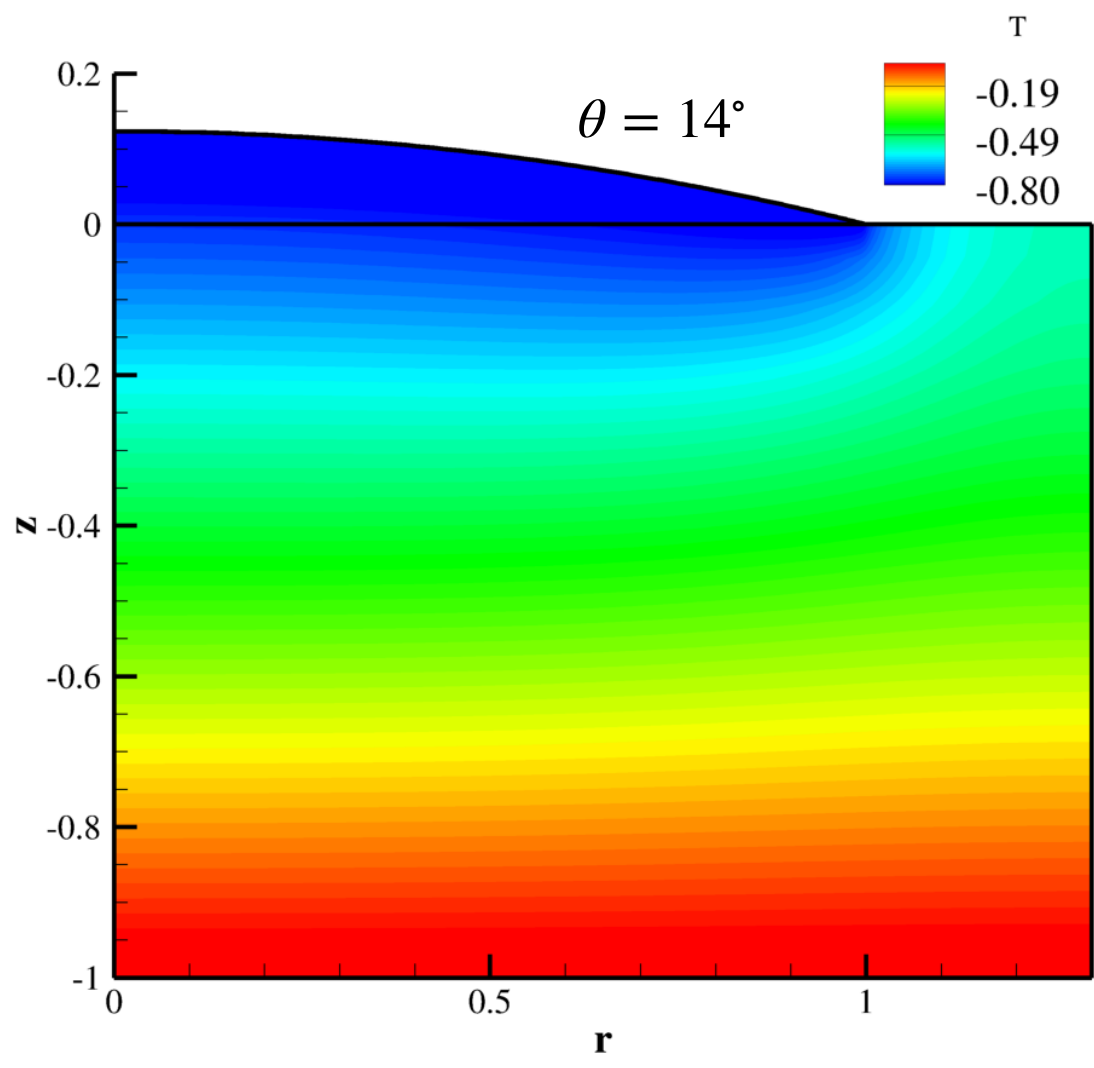


Figure 3.51. The temperature profiles for $d = 1.0, k_s = 0.8$.

3.4 Particle Adsorption

3.4.1 The Influence of Viscosity Change Due to Particle Concentration Increase

When the particles at the CL reaches maximum packing, the simulation has to be stopped. When the simulations stopped, the bulk concentrations were still far from achieving high concentrations. The locations of stagnation points and the transition points are compared with simulations incorporating the influence of viscosity change and simulations without viscosity change. Figure 3.52 and 3.53 show that the locations are almost the same. So the only effect of the application of Krieger-Dougherty relationship was to terminate the simulation when maximum packing was reached.

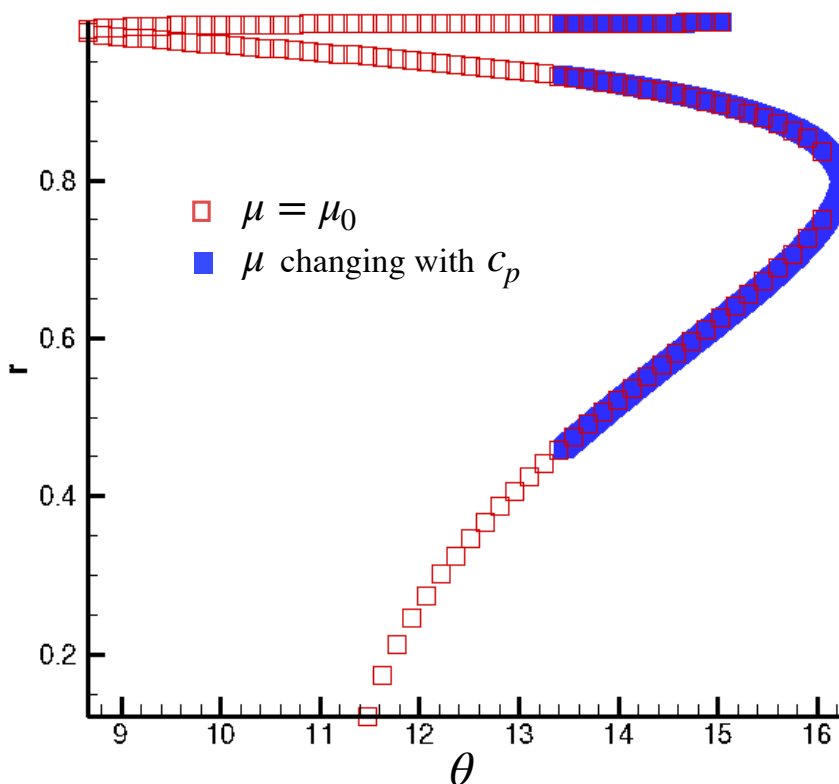


Figure 3.52. The locations of stagnation points are compared with simulations incorporating the influence of viscosity change and simulations without viscosity change. The results are with $d = 0.15$.

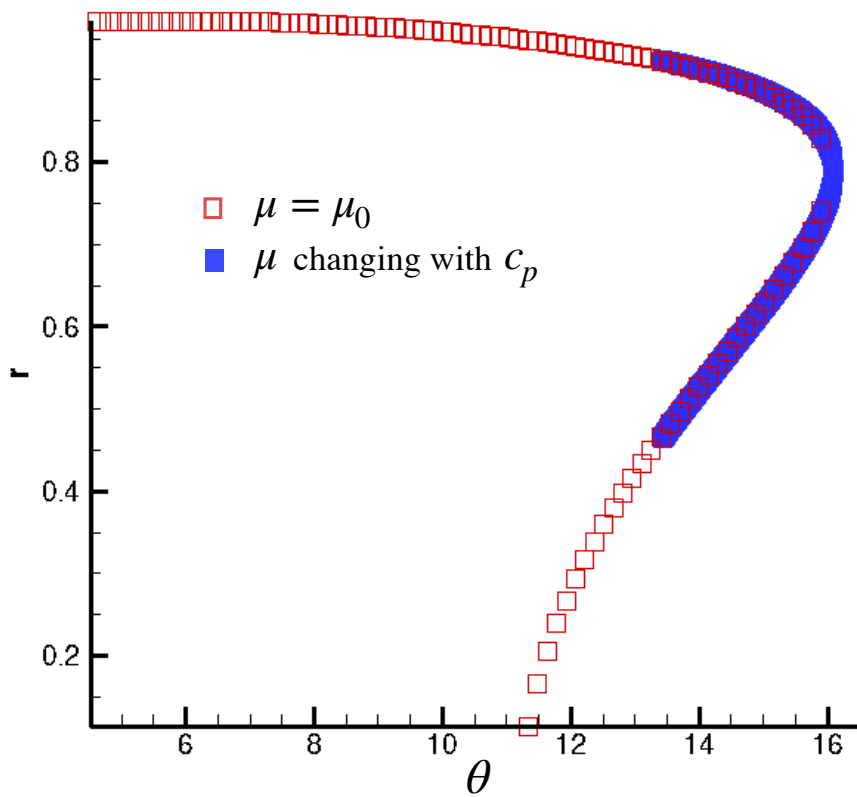


Figure 3.53. The locations of transition points are compared with simulations incorporating the influence of viscosity change and simulations without viscosity change. The results are with $d = 0.15$.

3.4.2 Substrate Adsorption

Since the adsorption to the substrate contributes to the deposition on the substrate, we will also call the process of adsorption to the substrate the deposition process.

3.4.2.1 Marangoni Flow Due to Temperature Change

A value of $Da = 100$ was used to investigate the influence of the particle adsorption to the substrate. Figure 3.54, on the one hand, indicates the mass conservation of particles by adding mass in the drop and the mass on the substrate, and on the other hand shows the amount of particles remaining in the bulk phase. When θ decreased to less than 10° , almost all particles adsorbed to the substrate, or in another word, deposited on the substrate. Compared to the mass change of a drop with no Marangoni flow (Figure 3.55), the Marangoni flow fostered the adsorption rate.

The adsorption location is shown by Figure 3.56. The surface concentration of the particles on the substrate Γ_{sub} increased as θ decreased. The concentration increased faster at $r = 0$ and CL.

The deposition at $r = 0$ was due to the downward flow of the Marangoni circulation. The concentration increase at $r = 0$ was much slower when Marangoni stress was not included in the simulation, as Figure 3.59. Because of the first-order adsorption rate, a higher local concentration leads to faster deposition. The downward flow, as in Figure 3.57, brought the particles accumulated at the surface near the substrate and facilitated the adsorption. In contrast, the high concentration region stayed at the drop surface with no Marangoni flow (Figure 3.58), leading to slow adsorption at the substrate. Although there was also downward flow in Figure 3.58, the velocity was much smaller as what has been discussed in the first section.

The CL deposition was suppressed by the circulation, if Figure 3.56 is compared with Figure 3.59, which is the surface concentration increase with no Marangoni flow. The adsorption with Marangoni flow was relatively uniform compared to the capillary case.

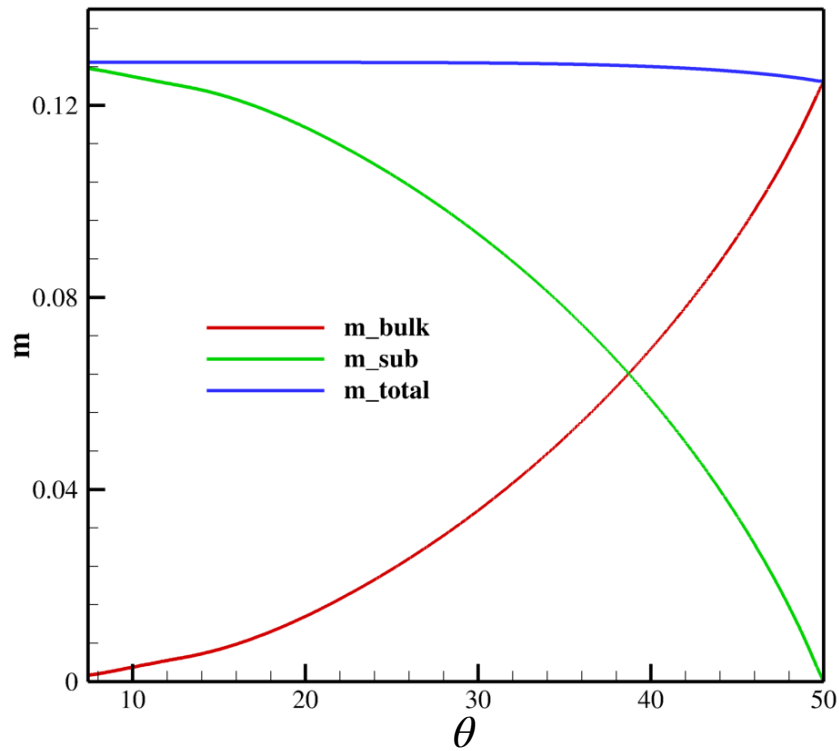


Figure 3.54. As a drop evaporates, the CA decreases from the right to the left on the abscissa. The red line shows the amount of particles in the bulk of the drop phase. The green line shows the amount of particles deposited on the substrate due to the adsorption. The blue line is the summation of the particle amount in the bulk phase and on the substrate. The results are for $Da = 100$. The Marangoni flow was caused by temperature change. The substrate thickness was $d = 0.5$.

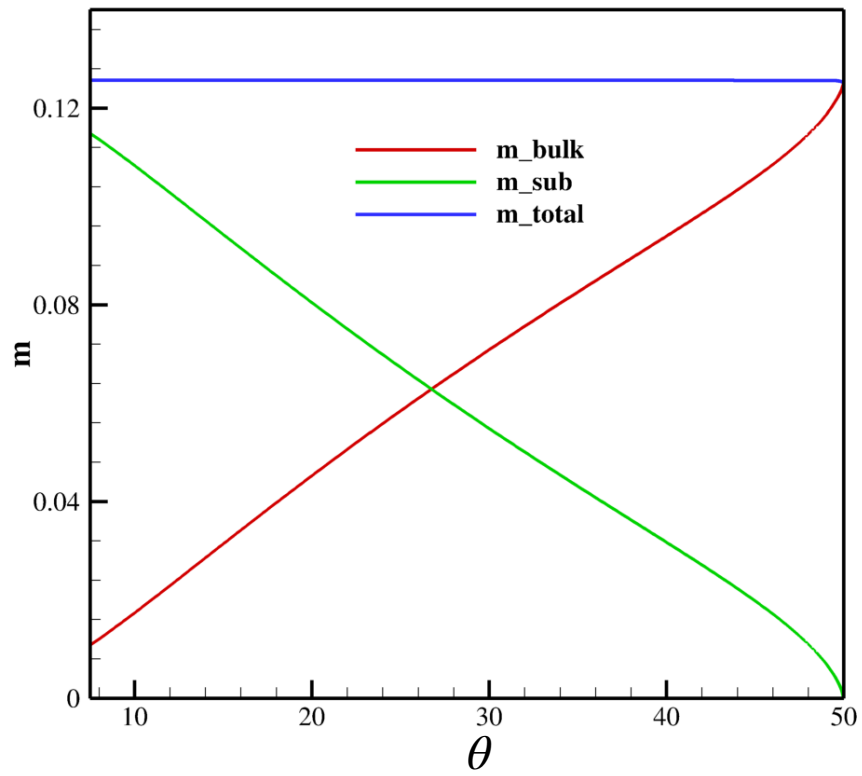


Figure 3.55. The meaning of the lines are the same as Figure 3.54. The results are for $Da = 100$ and pure capillary flows.

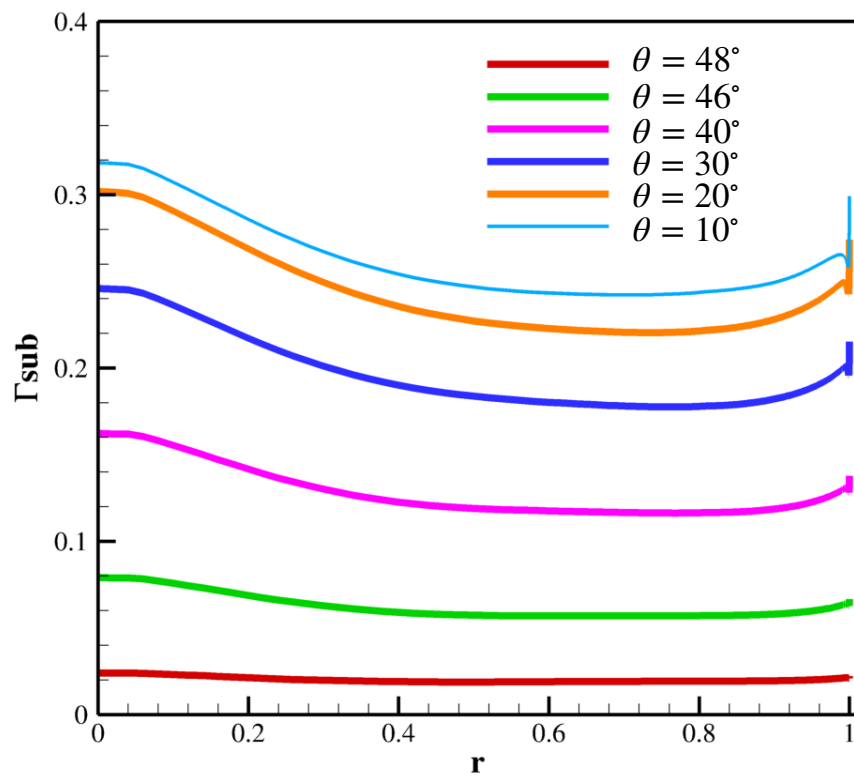


Figure 3.56. The surface concentration of the particles deposited on the substrate Γ_{sub} versus θ as CA decreased. The results are for $Da = 100$. The Marangoni flow was caused by temperature change. The substrate thickness was $d = 0.5$.

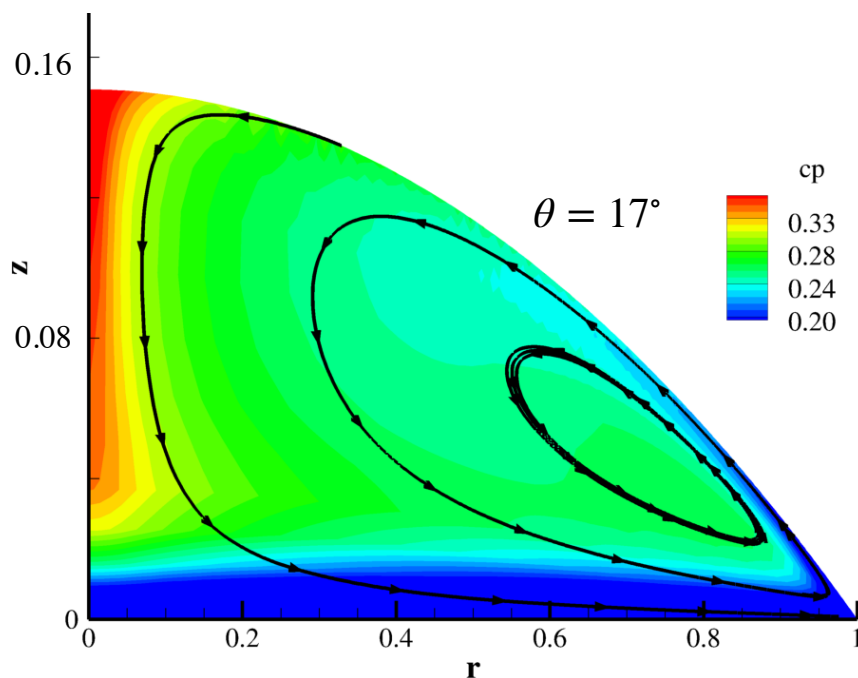


Figure 3.57. The flow and concentration profile at $\theta = 17^\circ$ with $Da = 100$. The Marangoni flow was induced by temperature change with $d = 0.5$.

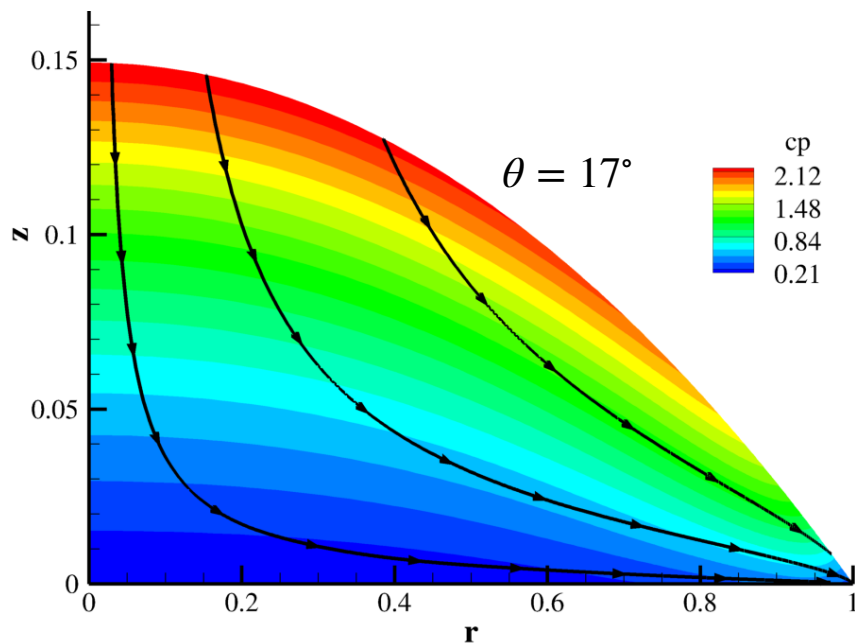


Figure 3.58. The flow and concentration profile at $\theta = 17^\circ$ with $Da = 100$. The flow was pure capillary flow with no Marangoni stress effect.

For example, Γ_{sub} was around 0.2 for any r when $\theta = 30^\circ$ in Figure 3.56, while was less than 0.1 at $r = 0$ and around 0.3 at CL in Figure 3.59.

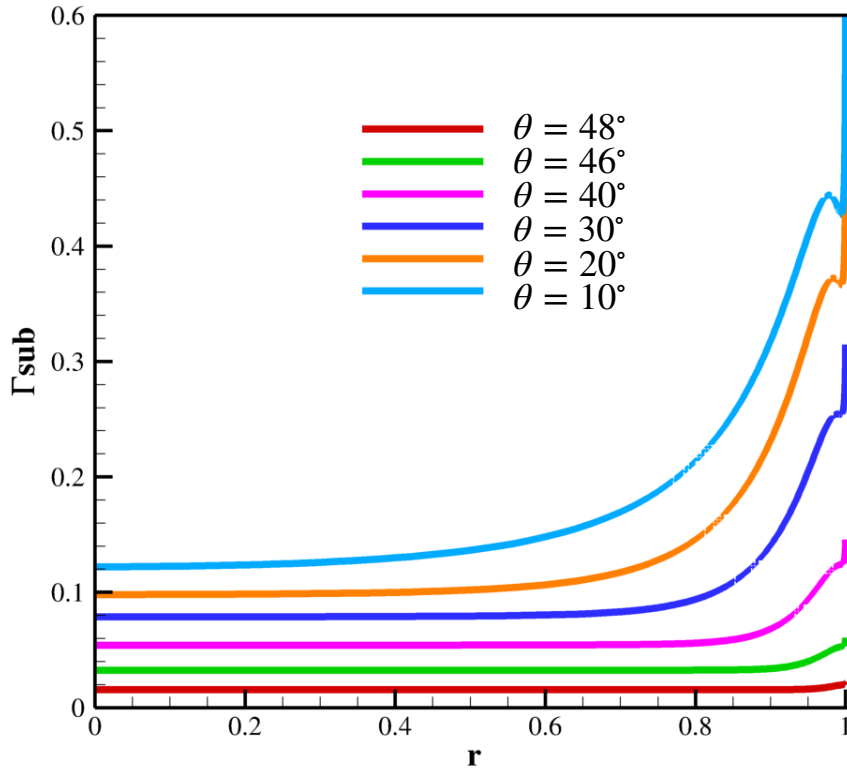


Figure 3.59. The surface concentration of the particles deposited on the substrate Γ_{sub} versus θ as CA decreased. The results are for $Da = 100$. No Marangoni flow was incorporated.

3.4.2.2 Application of a Fixed Marangoni Stress

To further compare the influence of the magnitude and the direction of Marangoni stresses on the adsorption rate, fixed Marangoni stresses were imposed on the drop surface. The moment when 80% of the total particles were deposited on the substrate was revealed by the contact angle $\theta_{0.8}$ of that moment. The larger $\theta_{0.8}$ is, the earlier most particles deposit on the substrate, indicating a faster deposition rate. According to Figure 3.60, a Marangoni stress in the direction from the top to CL facilitates the deposition and the deposition rate increases with the increase of Ma . However, the influence of a Marangoni

stress in the opposite direction depends on the magnitude of Ma . When $|Ma|$ was smaller than 10^3 , the deposition was compromised.

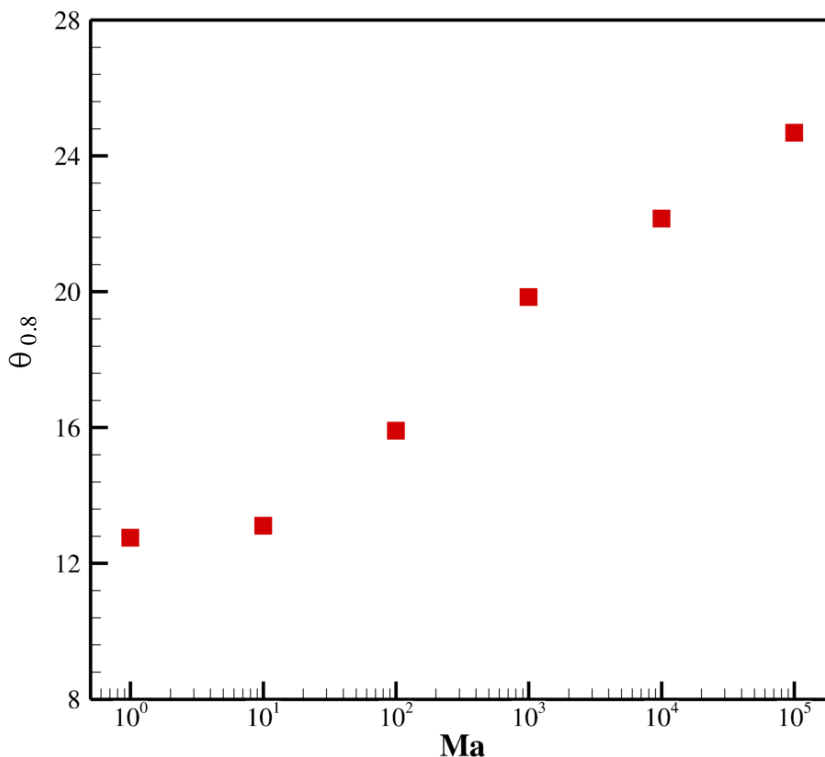


Figure 3.60. $\theta_{0.8}$ is the CA at the moment when 80% of the total particles were deposited on the substrate. The larger $\theta_{0.8}$ is, the earlier most particles deposit on the substrate, indicating the faster a deposition rate. The value of $\theta_{0.8}$ changed with Ma . The Marangoni stress is in the same direction as the tangential unit vector.

The specific deposition positions were given by Figure 3.62 under various Ma values. The results were plotted when CA was 12° . The green lines are the surface concentration of deposited particles. The blue lines are the concentration of suspended particles still in the bulk phase. The surface concentration of the suspended particles was derived by assuming that all particles fall at the same radial location on the substrate. The red lines are the summation of the deposited particle and the suspended particles.

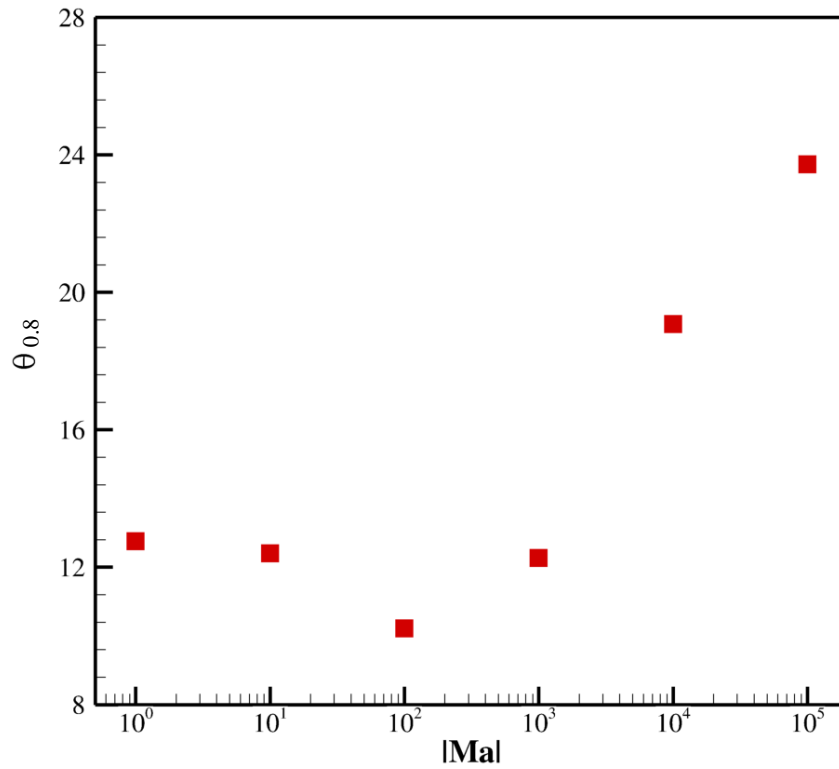


Figure 3.61. The same plot as Figure 3.60 but the direction of Marangoni stress, which was in the opposite direction as the tangential unit vector leading to counterclockwise circulation. Ma was negative, but the absolute value was used in the plot.

For a positive Ma , meaning the Marangoni stress from the top to CL, small Ma promoted deposition at the CL while large Ma promoted deposition in the drop middle. For a negative Ma , a larger $|Ma|$ resulted in the less deposition at the CL. The slow deposition rate for a small $|Ma|$ in Figure 3.61 was because of the reduced particle deposition at the CL. When $|Ma|$ was large, the deposition at the middle of the drop ($r = 0$) was significantly promoted, therefore contributing to the total deposition rate.

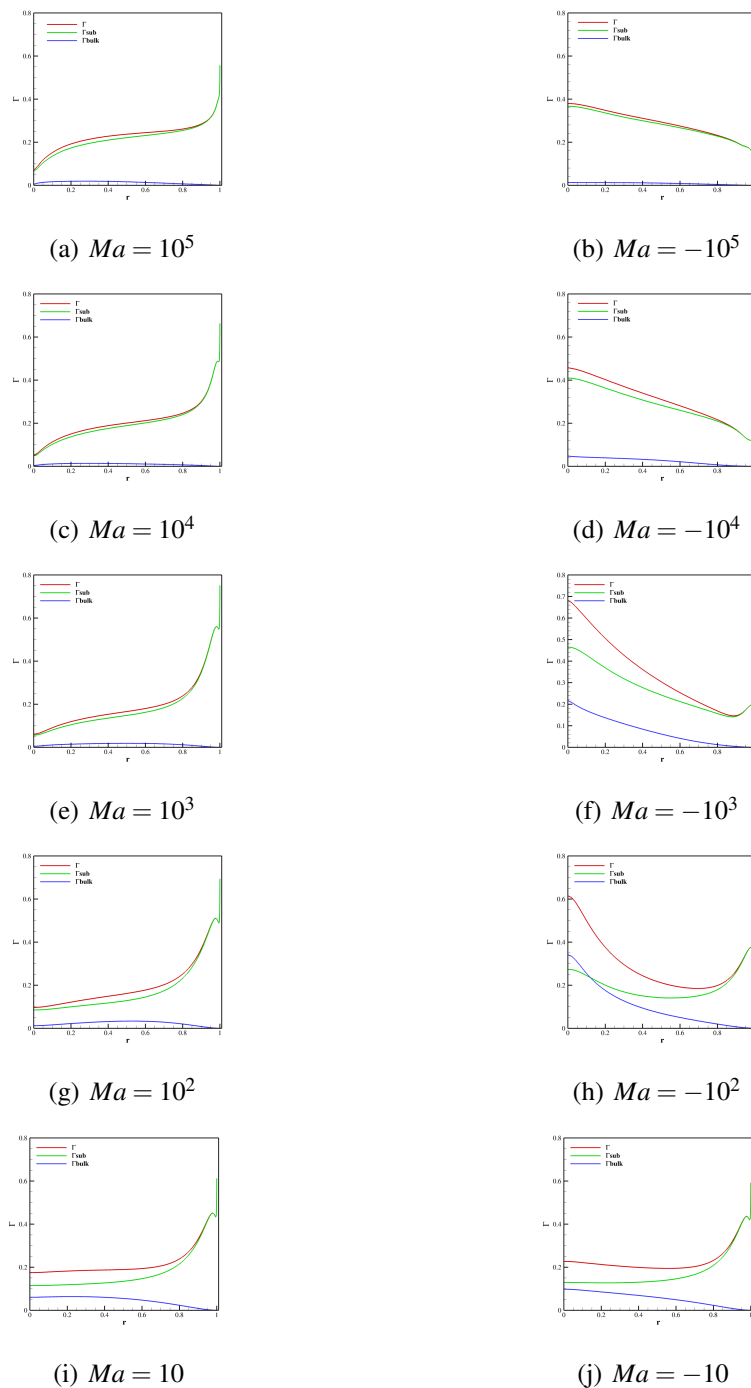


Figure 3.62. Three types of surface concentration Γ (blue for suspended particles, green for deposited particles and red for total particles) versus the radial locations r at $\theta = 12^\circ$. $Da = 100$. The plots are for different values of Ma imposed: the negative ones mean the Marangoni stress is in the opposite direction from the tangential unit vector \mathbf{t} .

4. SUMMARY AND FUTURE WORK

4.1 Summary

We numerically solved the coupled particle concentration, thermal and velocity fields in an evaporating drop. The effects of Marangoni flows on temperature, flow patterns, particle transport and deposition were especially investigated.

In terms of the thermal fields, we defined a Marangoni Peclet number Pe_{Ma} , which is proportional to the characteristic Marangoni velocity, as a criterion when neglect of heat convection is reasonable. This criterion was proved by the numerical results of the temperature distribution. In terms of the flow fields, we investigated the flows, especially the surface flow directions, not only at the initial evaporation stage, but also when the contact angle decreases below 15° . The flow changed from one-circulation to multi-circulation during drop evaporation.

At the late stage of evaporation, stagnation points emerge on the drop surface, which were divided into Marangoni-induced points and capillary-induced points. The locations of stagnation points may provide a better understanding of the temperature-induced Marangoni flow of drying drops. An explanation for the experimentally observed stagnation point near the contact line was given. This point is a capillary-induced stagnation point caused by the divergent capillary flow, according to both the numerical results and the lubrication theory validation. The explanation shows that the surface flow direction is not solely determined by Marangoni stress, especially near the contact line. The existence of this stagnation point potentially affects the evaporative deposition patterns and self-assembly of materials. So understanding the reasoning behind it may be useful to predict and control more precisely the deposition behavior of colloids during drop evaporation.

Although Marangoni circulation flows changed from a counterclockwise direction to a clockwise direction at a low CA, the CL region remained circulating in the counterclock-

wise direction, forming a segregated region from the other part of the drop. The segregated region was featured with a high particle concentration, meaning the trap of particles. However, compared to the coffee-ring accumulation resulting from mere capillary flow, the concentration in the segregated CL circulation was more uniform. These results implied the possibility to design the width of the coffee ring shape by adjusting the radial length of the CL circulation region.

The radial length of the CL circulation region was characterized by the radial location of a transition point, where $du/dz = 0$. The location changed with the thickness and the thermal conductivity of the substrate. The thicker the substrate was or the smaller the thermal conductivity was, the closer the transition point was away from CL, implying a narrower coffee ring shape would form.

The magnitude of the Marangoni effect can be indicated by the Marangoni number $Ma = \frac{\Delta\sigma}{\mu_0 v_c}$. By applying various fixed Ma on the surface, the flow profiles and the particle distribution greatly changed. On the whole, the larger Ma was, the more particles were kept in the middle of the drop instead of accumulating at CL. However, the Marangoni flow facilitated the CL accumulation if when the Marangoni stress was in the direction from the top to CL and $Ma < 10^3$.

When there was adsorption of particles to the substrate, Marangoni flows facilitated the deposition rate because they transported the particles from the drop surface, where particles accumulated due to base fluid evaporation, to the substrate region. A counterclockwise Marangoni circulation also changed the CL deposition profile to a more uniform profile by bringing down the particle at the surface to the center region of the substrate (where $r = 0$).

4.2 Future Studies

For future studies, I recommend the following projects on both simulations and experiments.

For simulations, first, drop evaporation with a heating substrate can be investigated. The heat exchange between the air and the drop is not negligible anymore because of the large temperature difference.

Second, a packing condition can be added to continue the simulation. My simulations were stopped once the maximum packing was reached at the CL. This stoppage could happen fairly early in the drop evaporation process. Thus, the maximum packing density regions need to be defined while the computations in the other regions of the droplet are allowed to continue. To use a packing condition, the fluid equations at the packing region need to transform to porous media flow like Darcy's law, and the shape of the surface near the CL is fixed by the packed particles instead of being subject to the traction boundary condition at the packing region.

Last, the adsorption of particles to the free surface cannot be simulated in this work because the accumulation of the particles at stagnation points led to too large a divergence of the concentration, which was not favorable in the FEM method. Multiscale simulations techniques will need to be employed to further elucidate this problem.

Besides, experiments can be done to validate simulations. Although our simulation results agree with some previous experimental results [65, 68], there are other experiments implying multi-circulations [77] that can be described more specifically (i.e. the thickness of the substrate) and compared with our simulations quantitatively. The agreement between experiments and simulations will also be more convincing if it is reached for cases with heated substrates.

REFERENCES

- [1] Robert D. Deegan, Olgica Bakajin, Todd F. Dupont, Greg Huber, Sidney R. Nagel, and Thomas A. Witten. Capillary flow as the cause of ring stains from dried liquid drops. *Nature*, 389(6653):827–829, 1997.
- [2] D.J. Norris, E.G. Arlinghaus, L. Meng, R. Heiny, and L.E. Scriven. Opaline photonic crystals: How does self-assembly work. *Advanced Materials*, 16(16):1393–1399, 2004.
- [3] Junhu Zhang, Zhiqiang Sun, and Bai Yang. Self-assembly of photonic crystals from polymer colloids. *Current Opinion in Colloid and Interface Science*, 14(2):103 – 114, 2009.
- [4] Sun Choi, Stefano Stassi, Albert P. Pisano, and Tarek I. Zohdi. Coffee-ring effect-based three dimensional patterning of micro/nanoparticle assembly with a single droplet. *Langmuir*, 26(14):11690–11698, 2010. PMID: 20527912.
- [5] Haoyan Zhao, Zhao Wang, Guifang Dong, and Lian Duan. Fabrication of highly oriented large-scale TIPS pentacene crystals and transistors by the Marangoni effect-controlled growth method. *Physical Chemistry Chemical Physics*, 17(9):6274–6279, 2015.
- [6] Joshua R. Trantum, David W. Wright, and Frederick R. Haselton. Biomarker-mediated disruption of coffee-ring formation as a low resource diagnostic indicator. *Langmuir*, 28(4):2187–2193, 2012. PMID: 22148855.
- [7] Stéphanie Devineau, Manos Anyfantakis, Laurent Marichal, Laurent Kiger, Mathieu Morel, Sergii Rudiuk, and Damien Baigl. Protein adsorption and reorganization on nanoparticles probed by the coffee-ring effect: Application to single point mutation detection. *Journal of the American Chemical Society*, 138(36):11623–11632, 2016. PMID: 27562632.
- [8] Yuanhang Li, Zichen Zhao, Miu Ling Lam, Wei Liu, Pak Piu Yeung, Ching-Chang Chieng, and Ting-Hsuan Chen. Hybridization-induced suppression of coffee ring effect for nucleic acid detection. *Sensors and Actuators B: Chemical*, 206:56 – 64, 2015.
- [9] Lei Li, Hua Hu, and Ronald G. Larson. Dna molecular configurations in flows near adsorbing and nonadsorbing surfaces. *Rheologica Acta*, 44(1):38–46, Dec 2004.
- [10] T Heim, S Preuss, B Gerstmayer, A Bosio, and R Blossey. Deposition from a drop: morphologies of unspecifically bound dna. *Journal of Physics: Condensed Matter*, 17(9):S703, 2005.

- [11] Tak Sing Wong, Ting Hsuan Chen, Xiaoying Shen, and Chih Ming Ho. Nanochromatography driven by the coffee ring effect. *Analytical Chemistry*, 83(6):1871–1873, 2011.
- [12] Jung-Yeul Jung, Young Won Kim, and Jung Yul Yoo. Behavior of particles in an evaporating didisperse colloid droplet on a hydrophilic surface. *Analytical Chemistry*, 81(19):8256–8259, 2009. PMID: 19737006.
- [13] Benjamin Michen, Christoph Geers, Dimitri Vanhecke, Carola Endes, Barbara Rothen-Rutishauser, Sandor Balog, and Alke Petri-Fink. Avoiding drying-artifacts in transmission electron microscopy: Characterizing the size and colloidal state of nanoparticles. *Scientific Reports*, 5:9793, may 2015.
- [14] Vadim Bromberg, Siyuan Ma, and Timothy J. Singler. High-resolution inkjet printing of electrically conducting lines of silver nanoparticles by edge-enhanced twin-line deposition. *Applied Physics Letters*, 102(21):214101, 2013.
- [15] Van Duong Ta, Andrew Dunn, Thomas J. Wasley, Ji Li, Robert W. Kay, Jonathan Stringer, Patrick J. Smith, Emre Esenturk, Colm Connaughton, and Jonathan D. Shephard. Laser textured superhydrophobic surfaces and their applications for homogeneous spot deposition. *Applied Surface Science*, 365:153 – 159, 2016.
- [16] Tim Still, Peter J. Yunker, and Arjun G. Yodh. Surfactant-induced Marangoni eddies alter the coffee-rings of evaporating colloidal drops. *Langmuir*, 28(11):4984–4988, 2012.
- [17] Alexander W. Wray, Demetrios T. Papageorgiou, Richard V. Craster, Khellil Sefiane, and Omar K. Matar. Electrostatic suppression of the “coffee stain effect”. *Langmuir*, 30(20):5849–5858, 2014. PMID: 24819778.
- [18] Leslie Y. Yeo and James R. Friend. Surface acoustic wave microfluidics. *Annual Review of Fluid Mechanics*, 46(1):379–406, 2014.
- [19] Nicole Raley Devlin, Katherine Loehr, and Michael T. Harris. The Importance of Gravity in Droplet Evaporation: A Comparison of Pendant and Sessile Drop Evaporation with Particles. *American Institute of Chemical C Engineers AICHE J*, 62(PART 1):947–955, 2016.
- [20] R. G. Picknett and R. Bexon. The evaporation of sessile or pendant drops in still air. *Journal of Colloid And Interface Science*, 61(2):336–350, 1977.
- [21] Xin Yang, Christopher Y. Li, and Ying Sun. From multi-ring to spider web and radial spoke: Competition between the receding contact line and particle deposition in a drying colloidal drop. *Soft Matter*, 10(25):4458–4463, 2014.
- [22] C. Bourgès-Monnier and M. E.R. Shanahan. Influence of Evaporation on Contact Angle. *Langmuir*, 11(7):2820–2829, 1995.
- [23] Tuan A H Nguyen and Anh V. Nguyen. Increased evaporation kinetics of sessile droplets by using nanoparticles. *Langmuir*, 28(49):16725–16728, 2012.
- [24] Byung Mook Weon and Jung Ho Je. Self-pinning by colloids confined at a contact line. *Physical Review Letters*, 110(2):1–5, 2013.

- [25] Lichao Gao and Thomas J. McCarthy. Contact angle hysteresis explained. *Langmuir*, 22(14):6234–6237, 2006. PMID: 16800680.
- [26] H. B. Eral, D. J. C. M. 't Mannetje, and J. M. Oh. Contact angle hysteresis: a review of fundamentals and applications. *Colloid and Polymer Science*, 291(2):247–260, Feb 2013.
- [27] James Clerk Maxwell. *Collected scientific papers*. CUP, 1890.
- [28] Harry W. Morse. On evaporation from the surface of a solid sphere. *Proceedings of the American Academy of Arts and Sciences*, 45(14):363–367, 1910.
- [29] Irving Langmuir. The evaporation of small spheres. *Physical Review*, 12(5):368–370, 1918.
- [30] K. S. Birdi, D. T. Vu, and A. Winter. A study of the evaporation rates of small water drops placed on a solid surface. *The Journal of Physical Chemistry*, 93(9):3702–3703, 1988.
- [31] K.S. Birdi and D.T. Vu. Wettability and the evaporation rates of fluids from solid surfaces. *Journal of Adhesion Science and Technology*, 7(6):485–493, 1993.
- [32] Ronald J. Sicker, David F. Chao, Peter C. Wayner, Thao T.T. Nguyen, Jiaheng Yu, and Joel L. Plawsky. Spontaneously oscillating menisci: Maximizing evaporative heat transfer by inducing condensation. *International Journal of Thermal Sciences*, 128(February):137–148, 2018.
- [33] M. N. Popescu, G. Oshanin, S. Dietrich, and A. M. Cazabat. Precursor films in wetting phenomena. *Journal of Physics Condensed Matter*, 24(24):1–51, 2012.
- [34] Siswo Sumardiono and Johann Fischer. Molecular simulations of droplet evaporation processes: Adiabatic pressure jump evaporation. *International Journal of Heat and Mass Transfer*, 49(5-6):1148–1161, 2006.
- [35] A. J. Petsi and V. N. Burganos. Stokes flow inside an evaporating liquid line for any contact angle. *Physical Review E - Statistical, Nonlinear, and Soft Matter Physics*, 78(3):1–9, 2008.
- [36] S. S. Sazhin, I. N. Shishkova, A. P. Kryukov, V. Yu Levashov, and M. R. Heikal. Evaporation of droplets into a background gas: Kinetic modelling. *International Journal of Heat and Mass Transfer*, 50(13-14):2675–2691, 2007.
- [37] Zhenchen Zheng, Leping Zhou, Xiaoze Du, and Yongping Yang. Numerical investigation on conjugate heat transfer of evaporating thin film in a sessile droplet. *International Journal of Heat and Mass Transfer*, 101:10–19, 2016.
- [38] Alejandro M. Briones, Jamie S. Ervin, Shawn A. Putnam, Larry W. Byrd, and Lois Gschwender. Micrometer-sized water droplet impingement dynamics and evaporation on a flat dry surface, 2010.
- [39] Truong Pham and Satish Kumar. Drying of Droplets of Colloidal Suspensions on Rough Substrates. *Langmuir*, 33(38):10061–10076, 2017.
- [40] H. B. Ma, P. Cheng, B. Borgmeyer, and Y. X. Wang. Fluid flow and heat transfer in the evaporating thin film region. *Microfluidics and Nanofluidics*, 4(3):237–243, 2008.

- [41] S. Semenov, V. M. Starov, M. G. Velarde, and R. G. Rubio. Droplets evaporation: Problems and solutions. *European Physical Journal: Special Topics*, 197(1):265–278, 2011.
- [42] Robert D. Deegan, Olgica Bakajin, Todd F. Dupont, Greg Huber, Sidney R. Nagel, and Thomas A. Witten. Contact line deposits in an evaporating drop. *Physical Review E - Statistical Physics, Plasmas, Fluids, and Related Interdisciplinary Topics*, 62(1 B):756–765, 2000.
- [43] Hua Hu and Ronald G. Larson. Evaporation of a sessile droplet on a substrate. *Journal of Physical Chemistry B*, 106(6):1334–1344, 2002.
- [44] L. Yu Barash. Marangoni convection in an evaporating droplet: Analytical and numerical descriptions. *International Journal of Heat and Mass Transfer*, 102:445–454, 2016.
- [45] Xuefeng Xu, Jianbin Luo, and Dan Guo. Radial-velocity profile along the surface of evaporating liquid droplets. *Soft Matter*, 8(21):5797–5803, 2012.
- [46] Hua Hu and Ronald G. Larson. Analysis of the effects of marangoni stresses on the microflow in an evaporating sessile droplet. *Langmuir*, 21(9):3972–3980, 2005.
- [47] C. Nadir Kaplan, Ning Wu, Shreyas Mandre, Joanna Aizenberg, and L. Mahadevan. Dynamics of evaporative colloidal patterning. *Physics of Fluids*, 27(9), 2015.
- [48] Francois Boulogne, Francois Ingremeau, and Howard A. Stone. Coffee-stain growth dynamics on dry and wet surfaces. *Journal of Physics Condensed Matter*, 29(7), 2017.
- [49] Guillaume Berteloot, Anna Hoang, Adrian Daerr, H. Pirouz Kavehpour, Francois Lequeux, and Laurent Limat. Evaporation of a sessile droplet: Inside the coffee stain. *Journal of Colloid and Interface Science*, 370(1):155–161, 2012.
- [50] Jungho Park and Jooho Moon. Control of colloidal particle deposit patterns within picoliter droplets ejected by ink-jet printing. *Langmuir*, 22(8):3506–3513, 2006.
- [51] Michel Versluis, Xuehua Zhang, Detlef Lohse, Pengyu Lv, Christian Diddens, Huan-shu Tan, and J. G. M. Kuerten. Evaporating pure, binary and ternary droplets: thermal effects and axial symmetry breaking. *Journal of Fluid Mechanics*, 823:470–497, 2017.
- [52] Stefan Karpitschka, Ferenc Liebig, and Hans Riegler. Marangoni Contraction of Evaporating Sessile Droplets of Binary Mixtures. *Langmuir*, 33(19):4682–4687, 2017.
- [53] Tim Still, Peter J. Yunker, and Arjun G. Yodh. Surfactant-induced Marangoni eddies alter the coffee-rings of evaporating colloidal drops. *Langmuir*, 28(11):4984–4988, 2012.
- [54] Haihu Liu, Yan Ba, Lei Wu, Zhen Li, Guang Xi, and Yonghao Zhang. A hybrid lattice Boltzmann and finite difference method for droplet dynamics with insoluble surfactants. *Journal of Fluid Mechanics*, 837:381–412, 2018.
- [55] Nicole Raley Devlin, Katherine Loehr, and Michael T. Harris. The separation of two different sized particles in an evaporating droplet. *AIChE Journal*, 61(10):3547–3556, 2015.

- [56] George Karapetsas, Kirti Chandra Sahu, and Omar K. Matar. Evaporation of Sessile Droplets Laden with Particles and Insoluble Surfactants. *Langmuir*, 32(27):6871–6881, 2016.
- [57] Hyungsoo Kim, François Boulogne, Eujin Um, Ian Jacobi, Ernie Button, and Howard A. Stone. Controlled Uniform Coating from the Interplay of Marangoni Flows and Surface-Adsorbed Macromolecules. *Physical Review Letters*, 116(12):1–5, 2016.
- [58] J. R. A. Pearson. On convection cells induced by surface tension. *Journal of Fluid Mechanics*, 4(5):489–500, 1958.
- [59] Fabien Girard, Mickaël Antoni, Sylvain Faure, and Annie Steinchen. Evaporation and Marangoni driven convection in small heated water droplets. *Langmuir*, 22(26):11085–11091, 2006.
- [60] Chafea Bouchenna, Mebrouk Ait Saada, Salah Chikh, and Lounès Tadrist. Generalized formulation for evaporation rate and flow pattern prediction inside an evaporating pinned sessile drop. *International Journal of Heat and Mass Transfer*, 109:482–500, 2017.
- [61] L. E. SCRIVEN and C. V. STERNLING. The Marangoni Effects. *Nature*, 187(4733):186–188, 1960.
- [62] Hua Hu and Ronald G. Larson. Analysis of the microfluid flow in an evaporating sessile droplet. *Langmuir*, 21(9):3963–3971, 2005.
- [63] R Savino, D Paterna, and N Favalaro. Buoyancy and Marangoni Effects in an Evaporating Drop. *Journal of Thermophysics and Heat Transfer*, 16(4):562–574, oct 2002.
- [64] Hua Hu and Ronald G Larson. Marangoni Effect Reverses Coffee-Ring Depositions. *The Journal of Physical Chemistry B*, 110:7090–7094, 2006.
- [65] Xuefeng Xu and Jianbin Luo. Marangoni flow in an evaporating water droplet. *Applied Physics Letters*, 91(12):2005–2008, 2007.
- [66] Joshua R. Trantum, Zachary E. Eagleton, Chetan A. Patil, Jason M. Tucker-Schwartz, Mark L. Baglia, Melissa C. Skala, and Frederick R. Haselton. Cross-sectional tracking of particle motion in evaporating drops: Flow fields and interfacial accumulation. *Langmuir*, 29(21):6221–6231, 2013.
- [67] Alvaro Marin, Robert Liepelt, Massimiliano Rossi, and Christian J. Kahler. Surfactant-driven flow transitions in evaporating droplets. *Soft Matter*, 12:1593–1600, 2016.
- [68] Yanshen Li, Cunjing Lv, Zhaohan Li, David Quéré, and Quanshui Zheng. From coffee rings to coffee eyes. *Soft Matter*, 11(23):4669–4673, 2015.
- [69] Maryam Parsa, Souad Harmand, Khellil Sefiane, Maxence Bigerelle, and Raphaël Deltombe. Effect of substrate temperature on pattern formation of nanoparticles from volatile drops. *Langmuir*, 31(11):3354–3367, 2015. PMID: 25742508.
- [70] F. Girard, M. Antoni, and K. Sefiane. On the effect of Marangoni flow on evaporation rates of heated water drops. *Langmuir*, 24(17):9207–9210, 2008.

- [71] W. D. Ristenpart, P. G. Kim, C. Domingues, J. Wan, and H. A. Stone. Influence of substrate conductivity on circulation reversal in evaporating drops. *Physical Review Letters*, 99(23):1–4, 2007.
- [72] Efeng Xu, Jianbin Luo, and Dan Guo. Criterion for reversal of thermal marangoni flow in drying drops. *Langmuir*, 26(3):1918–1922, 2010.
- [73] L. Yu Barash. Dependence of fluid flows in an evaporating sessile droplet on the characteristics of the substrate. *International Journal of Heat and Mass Transfer*, 84:419–426, 2015.
- [74] L. Yu Barash. Marangoni convection in an evaporating droplet: Analytical and numerical descriptions. *International Journal of Heat and Mass Transfer*, 102:445–454, 2016.
- [75] Rajneesh Bhardwaj, Xiaohua Fang, and Daniel Attinger. Pattern formation during the evaporation of a colloidal nanoliter drop: A numerical and experimental study. *New Journal of Physics*, 11, 2009.
- [76] Nagesh D. Patil, Prathamesh G. Bange, Rajneesh Bhardwaj, and Atul Sharma. Effects of Substrate Heating and Wettability on Evaporation Dynamics and Deposition Patterns for a Sessile Water Droplet Containing Colloidal Particles. *Langmuir*, 32(45):11958–11972, 2016.
- [77] Maryam Parsa, Souad Harmand, Khellil Sefiane, Maxence Bigerelle, and Raphaël Deltombe. Effect of substrate temperature on pattern formation of nanoparticles from volatile drops, 2015.
- [78] Lihui Wang and Michael T. Harris. Stagnation Point of Surface Flow during Drop Evaporation. *Langmuir*, 34(20):5918–5925, 2018.
- [79] Kai Zhang, Liran Ma, Xuefeng Xu, Jianbin Luo, and Dan Guo. Temperature distribution along the surface of evaporating droplets. *Physical Review E - Statistical, Nonlinear, and Soft Matter Physics*, 89(3):1–7, 2014.
- [80] Yanshen Li, Cunjing Lv, Zhaohan Li, David Quéré, and Quanshui Zheng. From coffee rings to coffee eyes. *Soft Matter*, 11(23):4669–4673, 2015.
- [81] Qingfeng Yan, Li Gao, Vyom Sharma, Yet Ming Chiang, and C. C. Wong. Particle and substrate charge effects on colloidal self-assembly in a sessile drop. *Langmuir*, 24(20):11518–11522, 2008.
- [82] Venkateshwar Rao Dugyala and Madivala G. Basavaraj. Control over coffee-ring formation in evaporating liquid drops containing ellipsoids, 2014.
- [83] Lloyd A. Spielman and S. K. Friedlander. Role of the electrical double layer in particle deposition by convective diffusion. *Journal of Colloid And Interface Science*, 46(1):22–31, 1974.
- [84] Ervina Widjaja and Michael T. Harris. Particle Deposition Study During Sessile Drop Evaporation. *AIChE Journal*, 54(9):2250–2260, 2008.
- [85] Anna Zigelman and Ofer Manor. The deposition of colloidal particles from a sessile drop of a volatile suspension subject to particle adsorption and coagulation. *Journal of Colloid and Interface Science*, 509:195–208, 2018.

- [86] Parul Katiyar and Jayant K. Singh. Evaporation induced self-assembly of different shapes and sizes of nanoparticles: A molecular dynamics study. *Journal of Chemical Physics*, 150(4):1–10, 2019.
- [87] Suresh Narayanan, Jin Wang, and Xiao-Min Lin. Dynamical Self-Assembly of Nanocrystal Superlattices during Colloidal Droplet Evaporation by in situ Small Angle X-Ray Scattering. *Physical Review Letters*, 93(13):1–4, 2004.
- [88] Terry P. Bigioni, Xiao Min Lin, Toan T. Nguyen, Eric I. Corwin, Thomas A. Witten, and Heinrich M. Jaeger. Kinetically driven self assembly of highly ordered nanoparticle monolayers. *Nature Materials*, 5(4):265–270, 2006.
- [89] Yanan Li, Qiang Yang, Mingzhu Li, and Yanlin Song. Rate-dependent interface capture beyond the coffee-ring effect. *Scientific Reports*, 6(March):1–8, 2016.
- [90] Peter J. Yunker, Tim Still, Matthew A. Lohr, and A. G. Yodh. Suppression of the coffee-ring effect by shape-dependent capillary interactions. *Nature*, 476(7360):308–311, 2011.
- [91] Karam Nashwan Al-Milaji and Hong Zhao. Probing the Colloidal Particle Dynamics in Drying Sessile Droplets, 2019.
- [92] Manos Anyfantakis, Zheng Geng, Mathieu Morel, Sergii Rudiuk, and Damien Baigl. Modulation of the coffee-ring effect in particle/surfactant mixtures: The importance of particle-interface interactions, 2015.
- [93] Saeed Jafari Kang, Vahid Vandadi, James D. Felske, and Hassan Masoud. Alternative mechanism for coffee-ring deposition based on active role of free surface, 2016.
- [94] Mingfei Zhao and Xin Yong. Nanoparticle motion on the surface of drying droplets. *Physical Review Fluids*, 3(3), 2018.
- [95] Kara L. Maki and Satish Kumar. Fast evaporation of spreading droplets of colloidal suspensions. *Langmuir*, 27(18):11347–11363, 2011.
- [96] Irvin M. Krieger and Thomas J. Dougherty. A Mechanism for Non-Newtonian Flow in Suspensions of Rigid Spheres. *Transactions of the Society of Rheology*, 3(1):137–152, 1959.
- [97] Nicole Raley Devlin. The separation of two different sized particles via droplet evaporation, 2015.
- [98] P. Hood. Frontal solution program for unsymmetric matrices. *International Journal for Numerical Methods in Engineering*, 10(2):379–399, 1976.
- [99] Christopher R Anthony. Dynamics of retracting films and filaments near singularities, 2017.
- [100] K.N. Christodoulou and L.E. Scriven. Discretization of free surface flows and other moving boundary problems. *Journal of Computational Physics*, 99(1):39 – 55, 1992.
- [101] Alfonso Arturo Castrejón-Pita, Osman A. Basaran, José Rafael Castrejón-Pita, Sumeet Suresh Thete, John Hinch, John R. Lister, Ian M. Hutchings, and Krishnaraj Sambath. Plethora of transitions during breakup of liquid filaments. *Proceedings of the National Academy of Sciences*, 112(15):4582–4587, 2015.

- [102] Sumeet Suresh Thete, Christopher Anthony, Pankaj Doshi, Michael T. Harris, and Osman A. Basaran. Self-similarity and scaling transitions during rupture of thin free films of Newtonian fluids. *Physics of Fluids*, 28(9):0–18, 2016.
- [103] Pritish M. Kamat, Brayden W. Wagoner, Sumeet S. Thete, and Osman A. Basaran. Role of Marangoni stress during breakup of surfactant-covered liquid threads: Reduced rates of thinning and microthread cascades. *Physical Review Fluids*, 3(4), 2018.
- [104] Ervina Widjaja and Michael T. Harris. Numerical study of vapor phase-diffusion driven sessile drop evaporation. *Computers and Chemical Engineering*, 32(10):2169–2178, 2008.

A. CONTACT ANGLE CHANGE

Many papers or thesis describe the process of drop evaporation with evaporation time. Yet, we used the CA as the indication for a more intuitive understanding of the stage of the evaporation. To facilitate the comparison with other work, a plot of the CA, θ , with the dimensionless time t is given as Figure A.1. Since the drop remains a spherical-cap shape and the evaporation speed is determined solely by vapor diffusion, the relationship between θ and t is always the same for all of the simulations in this dissertation.

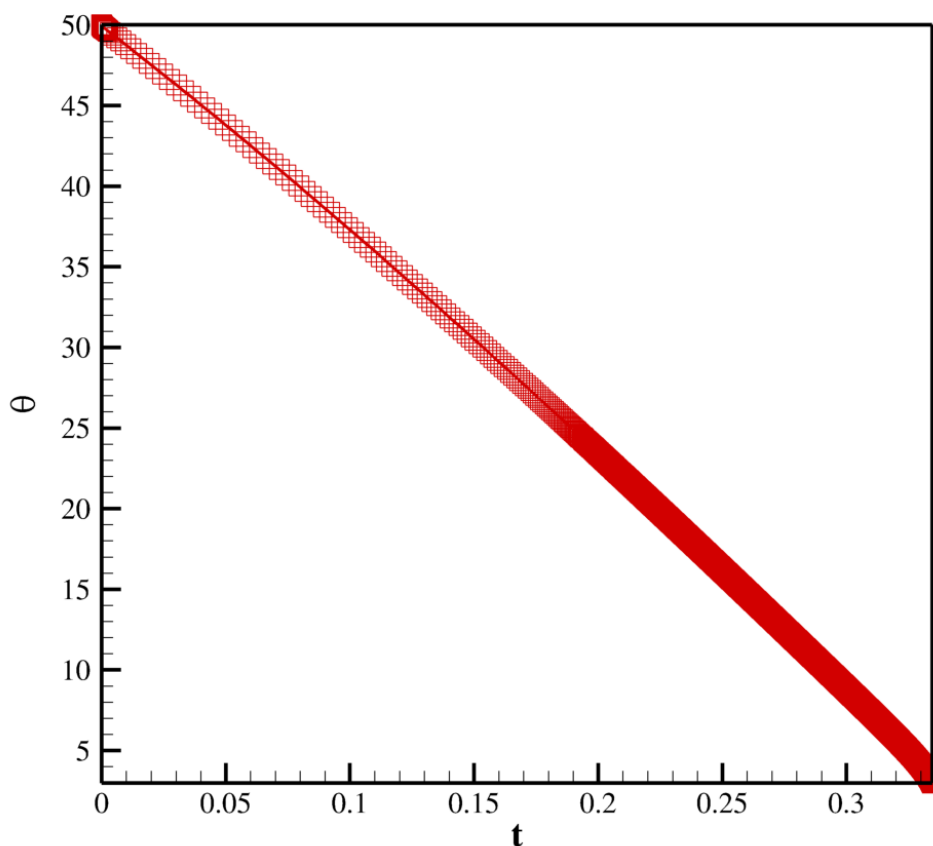


Figure A.1. The CA, θ , changing with the dimensionless time t . The characteristic time is 1.5×10^3 s.

B. NON-DIMENSIONALIZATION OF GOVERNING EQUATIONS AND BCS

B.1 Governing Equations

The Cauchy momentum equation:

$$\frac{\partial \tilde{\mathbf{v}}}{\partial \tilde{t}} + \tilde{\mathbf{v}} \cdot \tilde{\nabla} \tilde{\mathbf{v}} = \frac{1}{\rho} \tilde{\nabla} \cdot \tilde{\mathbf{T}} \quad (\text{B.1})$$

$$\frac{v_c}{t_c} \frac{\partial \mathbf{v}}{\partial t} + \frac{v_c^2}{l_c} \mathbf{v} \cdot \nabla \mathbf{v} = \frac{\tau_c}{\rho l_c} \nabla \cdot \mathbf{T} \quad (\text{B.2})$$

$$Re = \frac{\rho v_c^2}{\tau_c} = \frac{\rho v_c l_c}{\mu_0}, \quad t_c = \frac{l_c}{v_c} \quad (\text{B.3})$$

$$Re \cdot \left(\frac{\partial \mathbf{v}}{\partial t} + \mathbf{v} \cdot \nabla \mathbf{v} \right) = \nabla \cdot \mathbf{T} \quad (\text{B.4})$$

$$\tilde{\mathbf{T}} = \tilde{p} \mathbf{I} + \tilde{\mu} \left[\tilde{\nabla} \tilde{\mathbf{v}} + (\tilde{\nabla} \tilde{\mathbf{v}})^T \right] \quad (\text{B.5})$$

$$\tau_c \mathbf{T} = -p_c \rho \mathbf{I} + \frac{\mu_0 v_c}{l_c} \mu \left[\nabla \mathbf{v} + (\nabla \mathbf{v})^T \right] \quad (\text{B.6})$$

$$Ca = \frac{\tau_c}{p_c}, \quad \tau_c = \frac{\mu_0 v_c}{l_c} \quad (\text{B.7})$$

$$\mathbf{T} = -\frac{1}{Ca} p \mathbf{I} + \mu \left[\nabla \mathbf{v} + (\nabla \mathbf{v})^T \right] \quad (\text{B.8})$$

The Krieger-Dougherty relationship:

$$\tilde{\mu} = \mu_0 \left(1 - \frac{\tilde{c}_P}{\tilde{c}_{pm}} \right)^{-2} \quad (\text{B.9})$$

$$\mu_c \mu = \mu_0 \left(1 - \frac{c_{pc} \cdot c_P}{c_{pc} \cdot c_{pm}} \right)^{-2}, \quad \mu_c = \mu_0 \quad (\text{B.10})$$

$$\mu = \left(1 - \frac{c_P}{c_{pm}} \right)^{-2} \quad (\text{B.11})$$

The heat convection-diffusion equation:

$$\frac{\partial \tilde{T}}{\partial \tilde{t}} + \tilde{\mathbf{v}} \cdot \tilde{\nabla} \tilde{T} = \alpha \tilde{\nabla}^2 \tilde{T} \quad (\text{B.12})$$

$$\frac{T_c}{t_c} \frac{\partial T}{\partial t} + \frac{v_c T_c}{l_c} \mathbf{v} \cdot \nabla T = \frac{\alpha T_c}{l_c^2} \nabla^2 T \quad (\text{B.13})$$

$$Pe = \frac{v_c l_c}{\alpha} \quad (\text{B.14})$$

$$Pe \left(\frac{\partial T}{\partial t} + \mathbf{v} \cdot \nabla T \right) = \nabla^2 T \quad (\text{B.15})$$

The convection-diffusion equation for the particle concentration:

$$\frac{\partial \tilde{c}_p}{\partial \tilde{t}} + \tilde{\mathbf{v}} \cdot \tilde{\nabla} \tilde{c}_p = D_p \tilde{\nabla}^2 \tilde{c}_p \quad (\text{B.16})$$

$$\frac{c_{pc}}{t_c} \frac{\partial c_p}{\partial t} + \frac{v_c c_{pc}}{l_c} \mathbf{v} \cdot \nabla c_p = \frac{D_p c_{pc}}{l_c^2} \nabla^2 c_p \quad (\text{B.17})$$

$$Pe_p = \frac{v_c l_c}{D_p} \quad (\text{B.18})$$

$$Pe_p \left(\frac{\partial c_p}{\partial t} + \mathbf{v} \cdot \nabla c_p \right) = \nabla^2 c_p \quad (\text{B.19})$$

Heat conduction in the substrate:

$$\frac{\partial \tilde{T}_s}{\partial \tilde{t}} = \alpha_s \tilde{\nabla}^2 \tilde{T}_s \quad (\text{B.20})$$

$$\frac{T_c}{t_c} \frac{\partial T_s}{\partial t} = \alpha_s \frac{T_c}{l_c^2} \nabla^2 T_s \quad (\text{B.21})$$

$$\frac{\partial T_s}{\partial t} = F_0 \nabla^2 T_s \quad (\text{B.22})$$

B.2 Boundary Conditions

The kinetic boundary condition on the free surface:

$$\rho \mathbf{n} \cdot (\tilde{\mathbf{v}} - \tilde{\mathbf{v}}_s) = \tilde{J} = -\mathbf{n} \cdot D \tilde{\nabla} \tilde{c} \quad (\text{B.23})$$

$$\rho v_c \mathbf{n} \cdot (\mathbf{v} - \mathbf{v}_s) = \frac{D c_c}{l_c} J = -\frac{D c_c}{l_c} \mathbf{n} \cdot D \nabla c \quad (\text{B.24})$$

$$v_c = \frac{D c_c}{\rho l_c} \quad (\text{B.25})$$

$$\mathbf{n} \cdot (\mathbf{v} - \mathbf{v}_s) = J \quad (\text{B.26})$$

The stress balance on the free surface:

$$\mathbf{n} \cdot \tilde{\mathbf{T}} = -2\tilde{\mathcal{H}}\tilde{\boldsymbol{\sigma}}\mathbf{n} + \tilde{\nabla}_s\tilde{\boldsymbol{\sigma}} \quad (\text{B.27})$$

$$\boldsymbol{\tau}_c\mathbf{n} \cdot \mathbf{T} = -2\frac{\sigma_c}{l_c}\mathcal{H}\boldsymbol{\sigma}\mathbf{n} + \frac{\sigma_c}{l_c}\nabla_s\boldsymbol{\sigma} = -2p_c\mathcal{H}\boldsymbol{\sigma}\mathbf{n} + p_c\nabla_s\boldsymbol{\sigma} \quad (\text{B.28})$$

$$Ca = \frac{\tau_c}{p_c} = \frac{\tau_c}{\sigma_c/l_c} \quad (\text{B.29})$$

$$Can \cdot \mathbf{T} = -2\mathcal{H}\boldsymbol{\sigma}\mathbf{n} + \nabla_s\boldsymbol{\sigma} \quad (\text{B.30})$$

For thermal Marangoni stress,

$$\tilde{\nabla}_s\tilde{\boldsymbol{\sigma}} = \beta\tilde{\nabla}_s\tilde{T} \quad (\text{B.31})$$

$$\mathbf{n} \cdot \tilde{\mathbf{T}} = -2\tilde{\mathcal{H}}\tilde{\boldsymbol{\sigma}}\mathbf{n} + \beta\tilde{\nabla}_s\tilde{T} \quad (\text{B.32})$$

$$\boldsymbol{\tau}_c\mathbf{n} \cdot \mathbf{T} = -2\frac{\sigma_c}{l_c}\mathcal{H}\boldsymbol{\sigma}\mathbf{n} + \beta\frac{T_c}{\sigma_c}\frac{\sigma_c}{l_c}\nabla_s T = -2p_c\mathcal{H}\boldsymbol{\sigma}\mathbf{n} + \left(\beta\frac{T_c}{\sigma_c}\right)p_c\nabla_s T \quad (\text{B.33})$$

$$Can \cdot \mathbf{T} = -2\mathcal{H}\boldsymbol{\sigma}\mathbf{n} + \left(\beta\frac{T_c}{\sigma_c}\right)\nabla_s T \quad (\text{B.34})$$

For a fixed Marangoni stress,

$$\tilde{\nabla}_s\tilde{\boldsymbol{\sigma}} = \tilde{\boldsymbol{\tau}}_{Ma}\mathbf{t} \quad (\text{B.35})$$

$$\mathbf{n} \cdot \tilde{\mathbf{T}} = -2\tilde{\mathcal{H}}\tilde{\boldsymbol{\sigma}}\mathbf{n} + \tilde{\boldsymbol{\tau}}_{Ma}\mathbf{t} \quad (\text{B.36})$$

$$\tau_{Ma} = Ma = \frac{\tilde{\boldsymbol{\tau}}_{Ma}}{\tau_c} \quad (\text{B.37})$$

$$\boldsymbol{\tau}_c\mathbf{n} \cdot \mathbf{T} = -2p_c\mathcal{H}\boldsymbol{\sigma}\mathbf{n} + \tau_c\tau_{Ma}\mathbf{t} \quad (\text{B.38})$$

$$Ca = \tau_c/p_c \quad (\text{B.39})$$

$$Can \cdot \mathbf{T} = -2\mathcal{H}\boldsymbol{\sigma}\mathbf{n} + Ca\tau_{Ma}\mathbf{t} = -2\mathcal{H}\boldsymbol{\sigma}\mathbf{n} + Ca \cdot Ma\mathbf{t} \quad (\text{B.40})$$

The energy balance at the free surface:

$$H_v\tilde{J} = -k_l\mathbf{n} \cdot \tilde{\nabla}\tilde{T} \quad (\text{B.41})$$

$$H_v\frac{Dc_c}{l_c}J = -k_l\frac{T_c}{l_c}\mathbf{n} \cdot \nabla T \quad (\text{B.42})$$

$$REH = \frac{H_vDc_c}{k_lT_c} \quad (\text{B.43})$$

$$REH \cdot J = -\mathbf{n} \cdot \nabla T \quad (\text{B.44})$$

The particle mass balance at the free surface:

$$\tilde{c}_p \cdot \frac{\tilde{\mathbf{J}}}{\rho} + D_p \mathbf{n} \cdot \tilde{\nabla} \tilde{c}_p = 0 \quad (\text{B.45})$$

$$\frac{c_{pc} D c_c}{\rho l_c} c_p \cdot \mathbf{J} + \frac{D_p c_{pc}}{l_c} \mathbf{n} \cdot \nabla c_p = c_{pc} v_c \cdot c_p \cdot \mathbf{J} + \frac{D_p c_{pc}}{l_c} \mathbf{n} \cdot \nabla c_p = 0 \quad (\text{B.46})$$

$$Pe_p c_p \cdot \mathbf{J} + \mathbf{n} \cdot \nabla c_p = 0 \quad (\text{B.47})$$

The heat flux balance at the drop-substrate interface:

$$\mathbf{n} \cdot (k_s \tilde{\nabla} \tilde{T}_s - k_l \tilde{\nabla} \tilde{T}) = 0 \quad (\text{B.48})$$

$$\mathbf{n} \cdot \left(\nabla T_s - \frac{1}{k_R} \nabla T \right) = 0 \quad (\text{B.49})$$

Particle mass balance at the drop-substrate interface:

$$D_p \mathbf{n} \cdot \tilde{\nabla} \tilde{c}_p + k \tilde{c}_p = 0 \quad (\text{B.50})$$

$$D_p \frac{c_{pc}}{l_c} \mathbf{n} \cdot \nabla c_p + k c_{pc} c_p = 0 \quad (\text{B.51})$$

$$Da = \frac{k l_c}{D_p} \quad (\text{B.52})$$

$$\mathbf{n} \cdot \nabla c_p + Da c_p = 0 \quad (\text{B.53})$$

Surface concentration of particles on the substrate:

$$\frac{\partial \tilde{\Gamma}}{\partial \tilde{t}} = k \cdot \tilde{c}_p \quad (\text{B.54})$$

$$\frac{c_{pc} l_c}{t_c} \frac{\partial \Gamma}{\partial t} = k c_{pc} c_p \quad (\text{B.55})$$

$$\frac{\partial \Gamma}{\partial t} = \frac{Da}{Pe_p} c_p \quad (\text{B.56})$$

$$\Gamma = \frac{Da}{Pe_p} \int_0^t c_p dt' \quad (\text{B.57})$$